Domain wall motion

in an ultracold ^{87}Rb gas

by

Mehdi Pourzand

B.Eng., Monash University Malaysia, 2016

Thesis Submitted in Partial Fulfillment of the

Requirements for the Degree of

Master of Science

in the

Department of Physics

Faculty of Science

Declaration of Committee

Name:	**Mehdi Pourzand**
Degree:	**Master of Science (Physics)**
Title:	**Domain wall motion in an ultracold ^{87}Rb gas**
Committee:	**Chair:** Karen Kavanagh
	Professor, Physics

Jeffrey McGuirk
Supervisor
Associate Professor, Physics

Paul Haljan
Committee Member
Associate Professor, Physics

Malcolm Kennett
Examiner
Associate Professor, Physics

Abstract

Spin diffusion in an ultracold nondegenerate bosonic gas is significantly affected by quantum collisions. In binary collisions of noncondensed indistinguishable particles, exchange symmetry can lead to a rotation of spins of the colliding particles. These spin-rotating collisions change dynamical properties of a multi-domain spin structure. Our magnetically-trapped two-level system is a quasi-one-dimensional pseudo-spin-$\frac{1}{2}$ gas of ^{87}Rb atoms.

This thesis work studies motion of domain walls as spin diffusion takes place in a spin-independent potential. To investigate domain wall motion, we devised a solution to optimally initialize the domains. We also developed an algorithm to analyze the experimental data to extract domain wall information.

The experimental results in this work suggest that the main prerequisite for the domain walls to move is asymmetry in the transverse spin distribution with respect to the wall center. The data shows that transverse spin distribution and total population ratio of the two states determine the type of motion a domain wall exhibits, and the path that it takes as the system evolves. Domain walls in the three-domain systems studied in this work exhibit a linear or oscillatory motion. To further understand domain wall motion, we also explored domain wall dynamics in two-domain systems. The results of this work are a first step in understanding why a domain wall moves, and how its trajectory can be controlled.

Keywords: Ultracold atoms; Spin diffusion; Domain wall motion; Nonequilibrium

Acknowledgements

Contents

List of Figures

Chapter 1

Introduction

Trapped ultracold atoms provide a powerful experimental platform to explore physics in the quantum regime. The strength of these systems arises from the high degree of control over the experimental parameters, enabling physicists to relatively easily manipulate a system of atoms.

Advancements in the field of ultracold atoms have been significant over the past decades. Today, the field covers a broad range of topics. Some examples are precision clocks [1], gravity sensors [2], and precision measurements in fundamental particle physics [3], just to name a few.

Even before atoms are cooled to degeneracy, quantum mechanical aspects of their behavior become unignorable at ultracold temperatures. As an atom is cooled, its associated thermal de Broglie wavelength that characterizes its spatial extent gets comparable to the interparticle interaction range. Particle indistinguishability and wavefunction symmetrization properties consequently lead to quantum effects [4].

In an ultracold nondegenerate Bose gas, spin dynamics is significantly affected by exchange interactions. In binary collisions of noncondensed indistinguishable particles, exchange symmetry can lead to a rotation of spins of the colliding particles [5]. This exchange interaction leads to a wide spectrum of interesting dynamics such as spin waves in trapped gases [6], localized collapse and revival of coherence [7], and spin self-rephasing and very long coherence times in a trapped atomic ensemble [8].

Improvements in measuring techniques of ultracold systems have enabled physicists to have greater experimental control. One of these advances has been the ability to have spatial resolution in measuring a system's dynamics [6], rather than just measuring the ensemble properties as a whole [9]. In addition to measuring techniques, initialization and control methods in ultracold atomic systems have been upgraded too. In the context of spin systems, these advancements enable us to initialize the system with more complicated spin profiles, and we have more control over the operating conditions as the dynamics evolves.

The McGuirk group has previously explored various topics involving spin diffusion in an ultracold nondegenerate trapped rubidium-87 (^{87}Rb) gas. Their previous work includes optical excitation of nonlinear spin waves [10], longitudinal spin diffusion of two pseudospin domains [11], and stability of two-domain spin structures and how it can be modified by an

effective magnetic field [12]. One of the topics that has not been explored is motion of a spin domain wall, which is investigated in this thesis.

The atomic system in this work is a bosonic cloud of ultracold trapped nondegenerate weakly-interacting ^{87}Rb atoms. The ensemble has a quasi-one-dimensional geometry with pseudo-spin-$\frac{1}{2}$ spin structure. This thesis explores displacement of spin domain walls as spin diffusion, affected by a spin rotation effect, takes place in spin-independent potential. The trajectory that a spin wall takes is a function of different initial parameters that determine how spin is distributed across the atom cloud in the beginning of the dynamics. The main focus of this thesis is on three-domain spin systems, but since the parameter space of these systems is quite large, only a small subset is covered. There are also a few examples of spin wall motion in two-domain clouds, illustrating the point that spin wall motion is a general phenomenon.

The structure of this thesis is as follows. Chapter 2 explains the experimental procedures in our apparatus, which involves the two techniques that we use to cool trapped atoms, and how imaging of the ensemble is performed. Chapter 3 presents the background theory of the system including how our pseudo-spin-$\frac{1}{2}$ atoms can be mapped onto the Bloch sphere. Chapter 3 also discusses a one-dimensional spin kinetic equation that, to a good degree, is the governing equation of our spin system. Chapter 4 then uses the discussions in Chapters 2 and 3 to explain how the desired spin domains are initialized and how the governing conditions of the dynamics are set. Chapter 5 covers the difficulties that were faced in spin domain preparation and details of the method we developed to solve the problem. Chapter 6 presents an algorithm that was developed to extract information about spin wall motion. Experimental data and the relevant discussions are given in Chapter 7. The last Chapter draws some general conclusions and suggests ideas for future work.

Chapter 2

Experimental procedures

This Chapter gives an overview of the apparatus with a description of the steps taken to conduct experiments and obtain data. Figure 2.1 shows an overview of one cycle of the experimental procedures involved in this thesis work. Initially atoms are loaded and laser cooled in a magneto-optical trap (MOT) as the first cooling stage. Once enough atoms are trapped and cooled in the MOT, we prepare the atoms for a mechanical transfer to a science cell where evaporative cooling further decreases the temperature of the magnetically trapped atoms. When the desired temperature is reached, the initial conditions of the experiment are set and the experiment starts under controlled operating conditions. After the experiment, the state of the atoms is changed using the adiabatic-rapid passage technique to prepare them for imaging. Finally, we image the atom cloud using an absorption imaging method. Parameter extraction and data analysis occur after the imaging. This Chapter explains the essential features of each of these steps before and after the experiment stage. For further details about these steps, see Ref. [13–16]. The experiment stage is discussed in detail in Chapter 4 after discussing the background theory in Chapter 3.
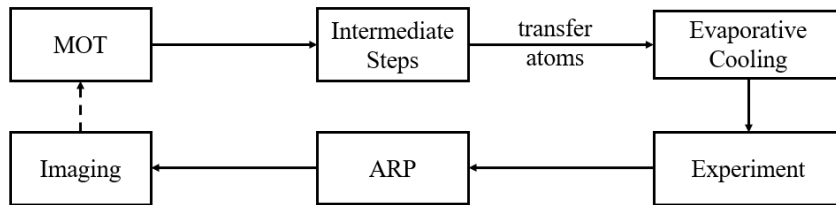
Figure 2.1: Overview of one experimental cycle. Initially, atoms are loaded and cooled in a magneto-optical trap (MOT). When the number of trapped atoms reaches a certain level, loading stops and three intermediate steps (i.e. compressed-MOT, optical pumping, and magnetic field increase) prepare the atoms to be mechanically transferred to a science cell, where evaporative cooling further decreases the temperature of the atoms. The experiment is then initialized and run. Finally, using the adiabatic-rapid passage (ARP) technique, the atoms are prepared to be imaged. The last step is imaging. The dashed line on the diagram means that at the end of every cycle, atoms in the science cell are dumped and new atoms are loaded in a new cycle. To obtain a full data set, what typically changes in the cycles is the evolution time at the experiment stage.

2.1 1$^{\text{st}}$ cooling step: laser cooling in a MOT

The key idea of the laser-cooling method is to slow neutral atoms by repeatedly targeting them with photons. In addition to cooling the atoms, a MOT simultaneously traps the atoms using an inhomogeneous magnetic field, which provides a position-dependent restoring force [17]. Figure 2.2 shows schematics of a MOT comprised of two coils and three pairs of counter-propagating laser beams. The coils are in an anti-Helmholtz configuration creating a spatially-varying quadrupolar magnetic field, with a zero point at the center. The three pairs of laser beams have opposite circular polarizations and intersect at the center of the trap.
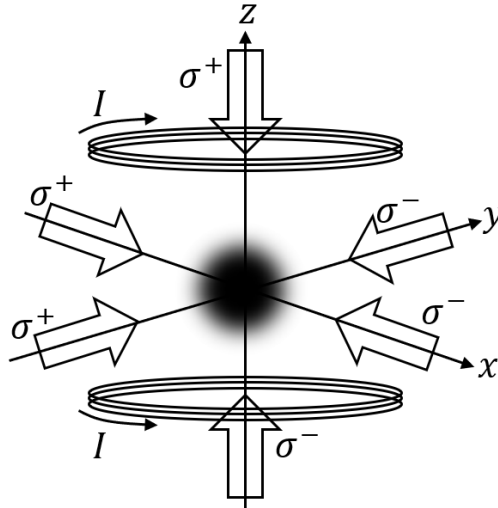
Figure 2.2: Schematic of a MOT setup. Two coils in anti-Helmholtz configuration create a quadrupolar magnetic field confining the atoms. Three pairs of laser beams with each pair of opposite circular polarization illuminate the atoms. The dark spot at the center represents trapped atoms.

To understand how a MOT works, it is easier to start with a one-dimensional MOT; a three-dimensional MOT is essentially an extension of that. To both cool and trap the atoms, photons should target those atoms that are moving away from the trap center. A moving atom in a spatially-varying magnetic field experiences both a Doppler shift of the laser frequency and a spatially-varying Zeeman shift of its magnetic sublevels m. Figure 2.3 shows how a one-dimensional MOT simultaneously exploits these two phenomena.

The two counter-propagating laser beams have opposite circular polarizations and are both red-detuned from the resonant frequency of stationary atoms. In this one-dimensional MOT, when an atom moves to the right, it will scatter more photons from the left-propagating beam because its polarization is set to be σ^-, which excites the atom to a state with $\Delta m = -1$. Photon absorption is polarization-dependent due to conservation of angular momentum. A similar process happens for an atom moving to the left and the right-propagating beam with σ^+ polarization, which excites the atom to a state with $\Delta m = +1$. To make a three-dimensional MOT, a similar structure is used in the other orthogonal axes. Although in Fig. 2.3 the ground state has $m = 0$, in the cooling process of ^{87}Rb in our system, the

4

ground state could occupy a non-zero Zeeman sublevel.
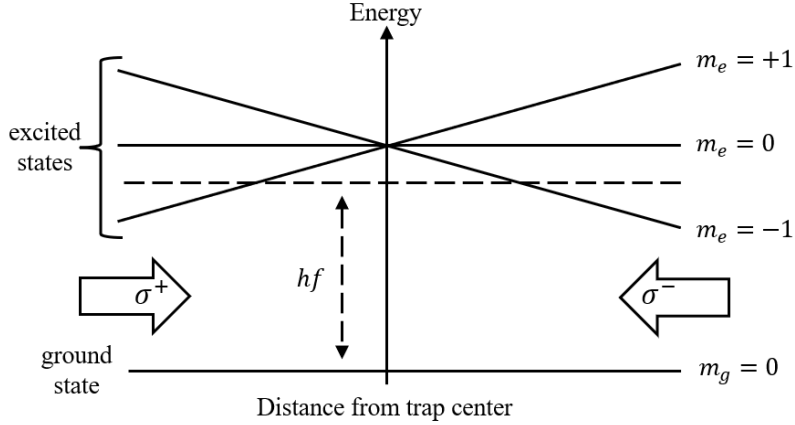
Figure 2.3: Trapping mechanism in a one-dimensional MOT. The trapping magnetic field Zeeman-shifts energy levels of the excited state. The horizontal dashed line indicates the energy of the incoming photons, which is red-detuned from the $m_e = 0$ state. Photons coming from the two directions have opposite circular polarizations. As an atom moves away from the trap center to the left, it will scatter more σ^+ photons because the transition $m_e - m_g = +1$ is resonant with these photons on the left of the trap center. Since the left-moving atom scatters more σ^+ than σ^- photons, it will be pushed back towards the center of the trap. Right-moving atoms experience a similar opposing force from σ^- photons in the transition $m_e - m_g = -1$.

The process that cools the atoms, i.e. slows them down, is as follows. After the atom is excited by absorbing a counter-propagating photon, it experiences a momentum kick opposite to its direction of motion. It then spontaneously emits a photon. This cycle repeats many times, and the atom slows. A key point here is that the spontaneous emission is isotropic; therefore, on average the momentum recoil the atom experiences by emitting photons is zero, whereas the momentum kicks it receives from laser photons are towards the center of the trap. Consequently, the velocity of the atoms in that direction decreases.

To cool atoms to lower temperatures, a cooling cycle is needed. This cycle is made of two energy levels. A red-detuned laser excites a moving atom to the higher level, exerting an opposing momentum kick, and then the atom isotropically emits a photon and de-excites. This process repeats many times, leading to a decrease in the ensemble temperature. In ^{87}Rb, the D_2 transition $\left(5^2S_{1/2} \rightarrow 5^2P_{3/2}\right)$ provides us with this cycle where a cooling laser of wavelength 780 nm is about 20 MHz (about 3 linewidths) red-detuned from the transition $F = 2 \rightarrow F' = 3$ (prime notation refers to the excited state). States with $F' = 3$ only decay to $F = 2$, but off-resonant excitation by the cooling laser transfers some atoms to $F' = 2$, which can decay to $F = 2$ or $F = 1$. If the atom goes to the state with $F = 1$, it gets out of the cooling cycle. To put it back into that cycle, a second laser, called the repump laser, is used. This laser is locked to the transition $F = 1 \rightarrow F' = 2$. Both the cooling and repump lasers are locked via the saturation absorption spectroscopy technique (see Ref. [14]). Transitions associated with the cooling and repump lasers are shown in Fig. 2.4.

The MOT duration is determined by comparing the voltage level of a photodiode that captures the photons emitted by the MOT atoms to a preset threshold voltage. The voltage

5
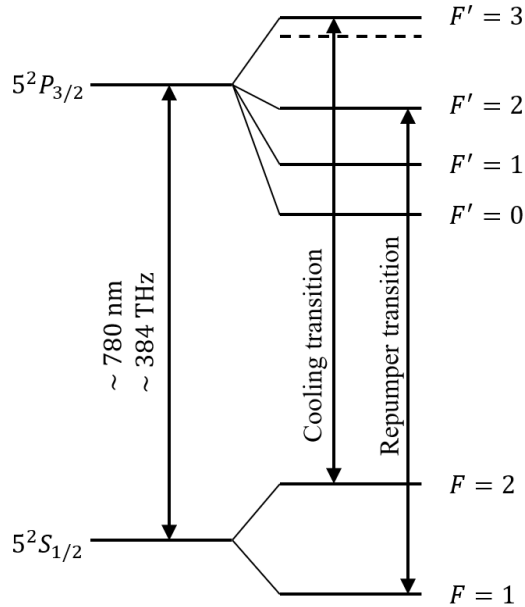
Figure 2.4: D$_2$ transition $\left(5^2\mathrm{S}_{1/2} \rightarrow 5^2\mathrm{P}_{3/2}\right)$ of ^{87}Rb in zero magnetic field. Cooling and repump transitions for laser cooling Rubidium atoms are shown. The wavelengths of both lasers are about 780 nm. The cooling laser is red-detuned (dashed line) and the repump laser is on resonance with the transitions shown on the diagram.

level has a monotonic relation with the cloud density at the end of the second cooling stage, and its value is chosen by the required operating density for the experiment. When the photodiode signal reaches the threshold voltage, loading of atoms into MOT stops and the apparatus prepares the trapped atoms to be transferred to the science cell where the second cooling step takes place. The next Section summarizes the intermediate steps needed before transferring the atoms.

2.2 Intermediate steps between the two cooling processes

To perform the second cooling stage, namely evaporative cooling, one requirement is to have a low collision rate with background atoms. However, this rate is high in the MOT cell; therefore, atoms are mechanically transferred to an ultra-high vacuum science cell, which is about half a meter away from the MOT cell. When the atoms are being moved to the science cell, they remain trapped in the magnetic field of the MOT coils which are mounted on a track.

Before the atoms are transported to the science cell, some intermediate steps are taken. There are two important results that are achieved by these steps. One is that atoms are transferred to one Zeeman sublevel. The other is that the cloud is compressed to a smaller size, which helps avoid heating.

At the end of the laser-cooling process, atoms are in a mixture of Zeeman sublevels. What we want is for the atoms to be in one internal state. Among the Zeeman sublevels

involved in the laser cooling, the state $|F = 1, m_F = -1\rangle$ is a magnetically trappable state, and at the end of the intermediate steps, atoms will be in this state with all the other states removed from the trap.

To transfer the atoms to the science cell, we first compress the cloud. This stage is referred to as a compressed MOT (CMOT). The reduction in cloud volume is needed because later we want to ramp up the magnetic field to keep the cloud trapped, and if the cloud size remains as large as it is at the end of MOT cooling, the increase in the magnetic field gradient will lead to heating the cloud. The CMOT is achieved by further red-detuning the cooling laser from the $F = 2 \rightarrow F' = 3$ transition and reducing the intensity of the repump laser. These modifications of the two lasers reduce the radiation pressure at the center of the cloud. Detuning the cooling laser reduces the photon scattering rate of the atoms in the $F = 2$ state and the reduction in repump intensity makes an atom spend less time in the $F = 2$ state.

We then optically pump the atoms to the $F = 1$ hyperfine ground state. The cooling laser does not address atoms that are in $F = 1$ (see Fig. 2.4); therefore, we can transfer the atoms to this state simply by turning off the repump laser. When the repump laser is off, the atoms that are excited to the $F' = 2$ state by the cooling laser will all eventually decay to the $F = 1$ state and stay there. The cooling laser is then turned off too. The ground-state atoms with $F = 1$ are in a mixture of Zeeman sublevels with $m_F = -1, 0, 1$. Of these sublevels, only $m_F = -1$ stays trapped; $m_F = 0$ is untrapped, and $m_F = 1$ is anti-trapped. Thus, the result of optical pumping is a cloud of atoms all in the state $|F = 1, m_F = -1\rangle$. Next, we ramp the magnetic field to tighten the trap, and the cloud is then moved to the science cell.

Figure 2.5 shows a summary of the intermediate steps between the two cooling processes. After the MOT atoms get to the science cell, they are released from the MOT magnetic field. The magnetic field of the science cell catches the atoms and evaporative cooling begins immediately. Details of this cooling step are discussed in the next Section.
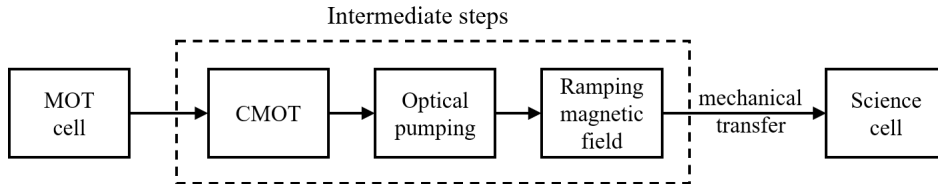
Figure 2.5: Diagram of the intermediate steps that are taken before the atoms are mechanically transferred from the MOT cell to the science cell. A compressed-MOT (CMOT) makes the atomic cloud smaller. Optical pumping takes the atoms to the state $|F = 1, m_F = -1\rangle$. Finally, the MOT magnetic field is ramped to tighten the trap. The cloud is then mechanically transferred to the science cell by moving the MOT coils, while it is being trapped in the magnetic field of these coils. When the coils reach the science cell, atoms are released from the MOT and caught by the magnetic field in the science cell.

2.3   2$^{\text{nd}}$ cooling step: evaporative cooling in a Ioffe-Pritchard trap

2.3.1   Magnetic trap in the science cell

The magnetic trap in the science cell is a hybrid Ioffe-Pritchard (HIP) trap. Instead of using a pair of coils like the Ioffe-Pritchard magnetic trap [18], a pair of permanent magnets are used for radially trapping the atoms by a quadrupole field in the radial direction. An advantage of permanent magnets is that unlike coils they do not need a power source to generate the magnetic field. Axial trapping of atoms is achieved by using two pairs of coils: pinch coils that produce axial field curvature, and bias coils, which produce a uniform magnetic field at the center of the cloud. Figure 2.6 schematically shows the structure of the HIP trap. Pinch coils are the outer coils and bias coils are the inner ones. In each pair of coils, the currents are in the same direction. The directions of the currents in the two pairs are opposite to each other. The orientation of the permanent magnets is shown in Fig. 2.7. They are oriented such that the resulting radial magnetic field from these magnets is in the same direction as that of the quadrupolar field in the MOT so that atoms can be smoothly transferred to the science cell.
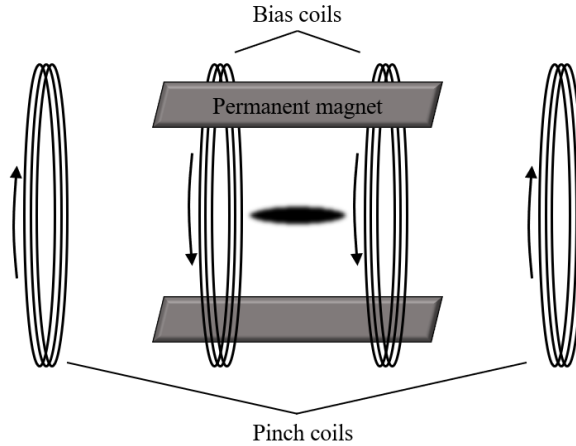
Figure 2.6: Structure of the hybrid Ioffe-Pritchard (HIP) trap in the science cell. The arrows next to the coils indicate direction of current, and the dark spot at the center represents trapped atoms. Radial confinement is done by a pair of permanent magnets. The pinch coils axially trap the atoms, and the bias coils control the bias field. The trapped ensemble is not drawn to scale.

The resulting trapping magnetic potential near the center of the trap is an anisotropic harmonic potential [18]

$$U = \frac{1}{2}m\left(\omega_\rho^2 \rho^2 + \omega_z^2 z^2\right),\tag{2.1}$$

where m is the ^{87}Rb mass and ρ (z) is the radial (axial) coordinate. The trap frequencies in the radial direction (ω_ρ) and axial direction (ω_z) are given by
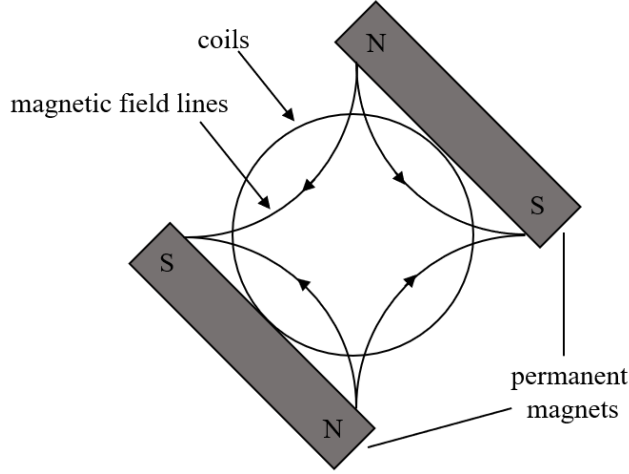
Figure 2.7: End-on view of the hybrid Ioffe-Pritchard trap showing permanent magnet orientation, which generate magnetic field in the radial direction only.

$$\omega_\rho = \sqrt{\frac{m_F g_F \mu_B}{m B_0}} \eta \,, \tag{2.2}$$

and

$$\omega_z = \sqrt{\frac{m_F g_F \mu_B \beta}{m}} \,, \tag{2.3}$$

where η is radial field gradient created by the permanent magnets, β is the axial field curvature created by the pinch coils, g_F is the Lande g-factor, μ_B is the Bohr magneton, B_0 is the bias magnetic field, and m_F is the magnetic sublevel. The 3D harmonic trapping potential causes the atom distribution at equilibrium to be Gaussian in both axial and radial directions. However, depending on the ratio of the two trap frequencies, the Gaussian widths in these two directions could be quite different.

To measure the radial and axial trap frequencies, a momentum kick is exerted on the cloud to set it into oscillation in the corresponding direction. This momentum kick is provided by a brief shift in the center of the magnetic trap, which is achieved by placing a small coil near the atoms. The orientation of the coil determines the direction of cloud oscillation, which in turn sets the direction of the trap center shift. The frequencies are extracted from sinusoidal fits. Figure 2.8 shows examples of measurements of radial and axial trap frequencies. The trap ratio is quite large: $\omega_\rho/\omega_z \simeq 37$. This ratio in magnetic confinement strength makes the cloud geometry highly elongated in the axial direction. The fast radial frequency rapidly averages any radial dynamics, which makes the cloud effectively a quasi-one-dimensional system.

2.3.2 Evaporative cooling

Evaporative cooling is the second cooling technique in our system. The key idea of this method is to remove atoms that have energies higher than the average energy of the cloud, while allowing the cloud to rethermalize through elastic collisions. Rethermalization of the

(a)

(b)
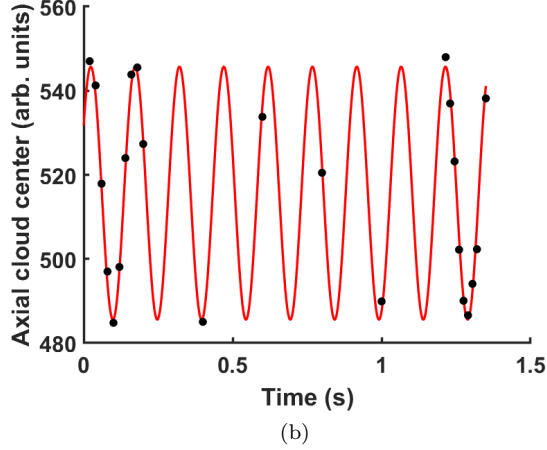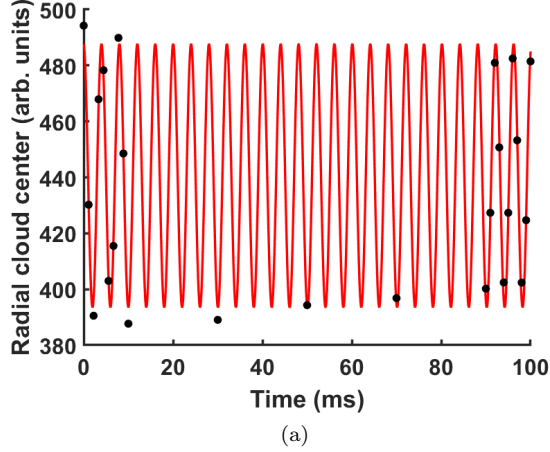
Figure 2.8: Measurement data of (a) radial (ω_ρ) and (b) axial (ω_z) trap frequencies. To induce oscillations in the radial or axial direction, a momentum kick is exerted on the atom cloud using an electromagnetic coil that is placed near the cloud. To extract the trap frequency in each direction, a sinusoid is fit to the position of the center of the cloud. In our system, $\omega_z = 2\pi \times 249.4 \pm 0.1\,\mathrm{Hz}$ and $\omega_\rho = 2\pi \times 6.72 \pm 0.01\,\mathrm{Hz}$, with the trap ratio $\omega_\rho/\omega_z \simeq 37$; therefore, the trapped ensemble is a highly elongated ellipsoid, making the cloud geometry quasi-one-dimensional.

ensemble and removal of these more energetic atoms leads to a drop in the temperature of the cloud [17].

Because the atoms are in a magnetic trap, they experience Zeeman shifts. The trapping potential is a harmonic potential; therefore, the Zeeman shift of an atom grows as the atom moves away from the trap center. In addition to this change in their Zeeman shift, atoms that have higher kinetic energy spend more time on average near the edges of the cloud. Using these two properties of atoms in the trap, we change the state of the more energetic atoms by adjusting the frequency (f) of an rf synthesizer such that the state of these atoms changes from the trapped state $|1, -1\rangle$ to the untrapped state $|1, 0\rangle$. By sweeping the rf frequency from high to low, the more energetic atoms get removed from the trap. To allow the ensemble to rethermalize, the rf frequency is therefore swept in a number of stages.

The evaporation process in our system uses nine stages. In each stage the rf frequency is decreased following the exponential form [13]

$$f(t) = (f_{\text{init}} - f_0) e^{-t/\tau} + f_0 \,, \tag{2.4}$$

where f_{init} and τ are the initial frequency and the time constant of the evaporation stage, respectively. f_0 is the trap bottom frequency below which the entire cloud is evaporated. In each evaporative cooling stage, half the energy of the cloud is removed. The functional form of decreasing the rf frequency in Eqn. 2.4 is chosen to be an exponential drop so that the cloud has time to rethermalize in each evaporation stage. Overall, in our experiment the rf frequency is decreased from 60 MHz to about 2 MHz. Furthermore, the thermalization rate is a function of collision rate, which varies as the density and temperature of the cloud change through the evaporation stages. To account for that, the time constant τ is modified accordingly in each exponential ramp.

The last evaporative cooling stage sets the temperature of the cloud. All the experimental data in this thesis are taken at temperature $T = 650$ nK, which for densities in this work (typically $2 \times 10^{13} \, \text{cm}^{-3}$) means the temperature is above the critical temperature for Bose-Einstein condensation. The experiment begins immediately after the last evaporation stage. Details of experiment initialization and control are discussed in Chapter 4. Once an experiment finishes, an adiabatic rapid passage step prepares the atoms to be imaged so that cloud parameters can be extracted. These steps are discussed in the following Sections of this Chapter.

2.4 Adiabatic rapid passage (ARP)

Information about the cloud properties at the end of an experiment is obtained by imaging the atoms. A key point in imaging atoms is to have a high signal-to-noise ratio (SNR). For this purpose, a cycling transition is needed. However, the state $|F = 1, m_F = -1\rangle$ does not have a corresponding excited state that forms a cycling transition. The state $|2, -2\rangle$ on the other hand makes a cycling transition with $|3, -3\rangle$. For this reason, before the imaging begins, we transfer the atoms from $|1, -1\rangle$ to $|2, -2\rangle$ via ARP. We use the ARP method because the resonance frequency varies across the cloud due to the harmonic trapping potential. To perform the ARP, the frequency of a microwave synthesizer is swept through resonance of all atoms in state $|1, -1\rangle$. The ARP process takes about 0.4 ms. It should be noted that the state $|2, -2\rangle$ is anti-trapped so the imaging should be done quickly after ARP.

2.5 Imaging

The imaging method that we use is absorption imaging, in which a resonant probe laser illuminates the atoms and a lens focuses their shadow as well as unabsorbed laser light onto a camera. To make the probe laser resonant with the entire cloud, the inhomogeneous magnetic field needs to become flat, which is achieved by increasing the strength of the bias

magnetic field. Another step that needs to be taken before turning on the probe laser is to allow the cloud to expand to avoid absorption saturation. The bias magnetic field is $\sim 3\,\mathrm{G}$ during the experiment, and imaging is done in $\sim 100\,\mathrm{G}$. Neither of these field values is suitable for the expansion. In a low field, the cloud quickly expands into the inhomogeneous regions of the trapping potential. In a high field, the cloud expands too slowly. We allow the cloud to expand in an intermediate field of $\sim 50\,\mathrm{G}$ for about $5\,\mathrm{ms}$. When the expansion step is finished, the bias field is ramped to $\sim 100\,\mathrm{G}$, and then the probe laser is turned on. In addition to flattening the magnetic potential, ramping the field up also increases energy separation of other sublevels from the probe transition frequency.

The probe laser is locked to the cycling transition $|F = 2, m_F = -2\rangle \leftrightarrow |F' = 3, m'_F = -3\rangle$ using the phase-locked loop (PLL) method (see Ref. [14] for further details). Figure 2.9 shows the transitions involved in ARP and imaging.
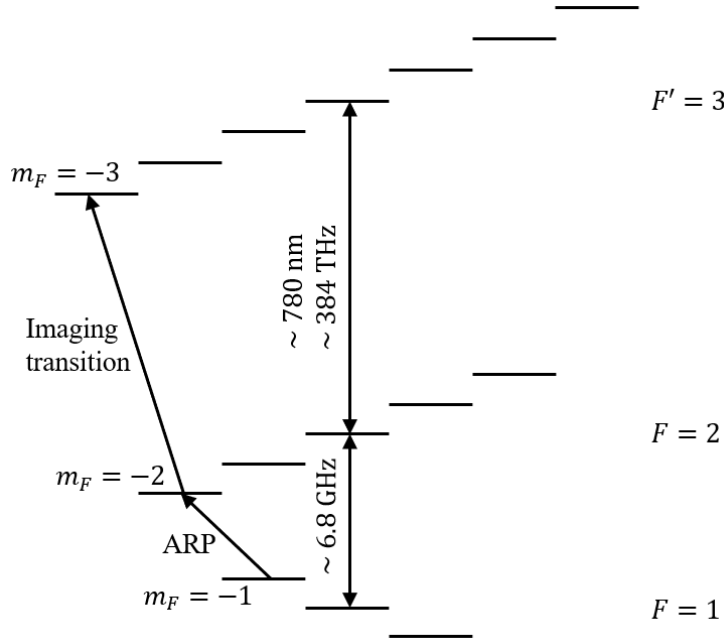
Figure 2.9: Schematics of ARP and imaging transitions for atoms initially in the state $5S_{1/2}\,|F = 1, m_F = -1\rangle$. After the atoms are transferred to the state $5S_{1/2}\,|F = 2, m_F = -2\rangle$ via ARP method, they are allowed to expand for about $5\,\mathrm{ms}$ to avoid absorption saturation. The cycling transition $5S_{1/2}\,|F = 2, m_F = -2\rangle \leftrightarrow 5P_{3/2}\,|F' = 3, m'_F = -3\rangle$ is used for absorption imaging. The energy separations are not drawn to scale.

Because the atoms in the state $|2, -2\rangle$ are not trapped, they fall due to gravity. To overcome this issue, a magnetic field from a shim coil is applied to counteract the downward force of gravity.

During imaging, photons from the probe laser and a small percentage of isotropically scattered photons from the atoms are captured by an electron-multiplying charge-coupled device (EMCCD) camera. This imaging method is destructive, i.e. at the end of imaging, atoms are lost from the trap and the experimental cycle must start over from the MOT stage. The images taken by the camera are read by a computer for analysis.

In each experimental cycle, there are three images that are required to account for systematics associated with the absorption imaging technique. In the first image ("atom image"), the probe laser is on and atoms are present. In the second image ("light image"), atoms are not present but the laser beam is still on. In the third image ("dark image"), there are no atoms and the laser beam is off.

Before cloud parameters such as temperature and number of atoms can be extracted from the images, we need to address systematics and resolve issues in optical density (OD). The beam of the probe laser has spatial intensity variations. These variations, along with peak intensity, are extracted from the light image. The dark image is also needed because there can always be some background light captured by the camera, in addition to the probe laser light and the scattered photons from the atoms. Additionally, the dark image provides a measure of the dark current and CCD biasing.

For each camera pixel, the measured optical density is given by Beer's law with the dark image intensity subtracted from the intensities of light and atom images:

$$OD_{\text{measured}} = \ln\left(\frac{I_{\text{light}} - I_{\text{dark}}}{I_{\text{atoms}} - I_{\text{dark}}}\right). \tag{2.5}$$

There is always a minimum detected intensity because the probe light is not entirely resonant with the cloud or can scatter from a path not passing through atoms. This minimum intensity corresponds to a saturation OD ($OD_{\text{saturation}}$) that is observed when all the resonant light is absorbed by the cloud. To measure $OD_{\text{saturation}}$, we image a very dense cloud such that the OD distribution saturates and obtains a flat top. The value of the flat part is $OD_{\text{saturation}}$, which is about 2.8 in our system. The modified optical density that accounts for saturation effects is

$$OD_{\text{modified}} = \ln\left(\frac{1 - e^{-OD_{\text{saturation}}}}{e^{-OD_{\text{measured}}} - e^{-OD_{\text{saturation}}}}\right). \tag{2.6}$$

The final correction is to account for saturation of the imaging transitions, which changes the scattering rate. This correction makes the final processed OD

$$OD_{\text{actual}} = OD_{\text{modified}} + \left(1 - e^{-OD_{\text{modified}}}\right)\frac{I_{\text{probe}}}{I_{\text{saturation}}} \tag{2.7}$$

We set the probe intensity I_{probe} to be $\sim 0.1\, I_{\text{saturation}}$ to minimize the saturation correction factor. Here, saturation intensity is $I_{\text{saturation}} = 1.67\,\text{mW/cm}^2$.

2.6 Extracting ensemble parameters

We find the cloud parameters following Ref. [13]. A nondegenerate cloud at equilibrium has a Gaussian density distribution in a harmonic trapping potential. The fitting function is a 2D Gaussian

$$f_{\text{Gaussian}} = OD_{\text{peak}}\, e^{-(z-z_c)^2/2(z_0')^2}\, e^{-(y-y_c)^2/2(y_0')^2}, \tag{2.8}$$

where $z\,(y)$ is the axial (radial) coordinate, z_c and y_c are coordinates of the center of the cloud, and $z_0'\,(y_0')$ is the axial (radial) width of the cloud after expansion. The parameters to be fit for each image are OD_{peak}, z_c, y_c, z_0' and y_0'. Because of the cloud expansion, z_0' is not

the actual axial Gaussian width. Denoting the trap frequency before and after expansion as ω_0 and ω respectively, the actual axial Gaussian width with expansion time t_{exp} is

$$z_0 = \frac{z_0'\omega}{\sqrt{\omega^2 + (\omega^2 + \omega_0^2)\sinh^2(\omega t_{\text{exp}})}}.$$ (2.9)

The trap frequency during the expansion does not change. Denoting the trap ratio by $\alpha = \omega_\rho/\omega_z$, the peak density is

$$n_0 = \frac{1}{(2\pi)^{3/2}} \frac{N\alpha^2}{z_0^3},$$ (2.10)

where N is the total number of atoms given by

$$N = 2\pi z_0 y_0 OD_{\text{peak}}/AC.$$ (2.11)

For the specific imaging states that we use for ^{87}Rb, the absorption cross-section (AC) is

$$AC = \frac{1}{2}\left(\frac{3\lambda^2}{2\pi}\right)\frac{1}{1 + 4\left(\frac{\Delta}{\Gamma}\right)^2},$$ (2.12)

where λ is the probe laser wavelength, and Γ is the natural linewidth. Δ is the detuning from resonance, but since the probe beam is on resonance, we have $\Delta = 0$. There is a factor of $1/2$ in front of Eqn. 2.12 because we drive a circular polarization transition with a linearly polarized light. Finally, the cloud temperature is

$$T = \frac{m\omega_z^2 z_0^2}{k_B}.$$ (2.13)

The next Chapter discusses the background theory of our experimental system.

Chapter 3

Background theory

This Chapter presents the relevant theoretical background for our system. Discussions are split into two Sections. The first Section discusses interaction of a two-level system with an oscillating electromagnetic field. It explains how we use Rabi π-pulses and $\frac{\pi}{2}$-pulses to manipulate the internal state of atoms in initializations and measurements. Next, the important concept of the Bloch sphere is presented. It is then shown how our two-level system is mapped onto the Bloch sphere. The second Section presents a 1D kinetic equation for spin dynamics. It discusses the identical spin rotation effect, which is a result of particle indistinguishability and wavefunction symmetrization in binary collisions. In our nondegenerate ultracold gases, this rotation effect is the dominant factor that modifies spin diffusion.

3.1 A two-level system in an oscillating electromagnetic field

3.1.1 Rabi flopping

The Hamiltonian of a two-level system coupled to an electromagnetic field is

$$H = \begin{bmatrix} -\hbar\omega_0/2 & \Omega_R e^{-i\omega t} \\ \Omega_R e^{i\omega t} & \hbar\omega_0/2 \end{bmatrix}, \tag{3.1}$$

where ω is the applied field frequency, ω_0 is the atomic resonance frequency between the two states, and t is the interaction duration. The strength of the coupling between the atom and the field is signified by the Rabi frequency, Ω_R. This Hamiltonian leads to what is called Rabi flopping in which an atom oscillates between the ground state $|1\rangle$ and the excited state $|2\rangle$ at frequency Ω_R while interacting with an oscillatory electromagnetic field. We can find the probability, $P_2(t)$, of finding an atom in the excited state by solving the time-dependent Schrodinger equation. For the initial conditions $P_1(t=0) = 1$ and $P_2(t=0) = 0$, $P_2(t)$ is

given by

$$P_2\left(t\right) = \left(\frac{\Omega_R}{\Omega'_R}\right)^2 \sin^2\left(\frac{\Omega'_R}{2}t\right), \tag{3.2}$$

where the effective Rabi frequency is

$$\Omega'_R = \sqrt{\Omega_R^2 + \delta^2}, \tag{3.3}$$

with $\delta \equiv \omega - \omega_0$ being the detuning of the field frequency from the transition frequency.

A π-pulse is defined as a pulse that is applied for a duration of t_π such that $\Omega'_R t_\pi = \pi$. This condition makes the sine-squared term in Eqn. 3.2 equal to 1. Similarly, a $\frac{\pi}{2}$-pulse is defined such that $\Omega'_R t_{\pi/2} = \pi/2$, making the sine-squared term equal to $1/2$. Figure 3.1 depicts Rabi flopping for the case where there is no detuning $\left(\Omega'_R = \Omega_R\right)$.

Rabi pulses can be used to modify the internal state of atoms. When the detuning is zero and the atom is in state $|1\rangle$, applying a π-pulse takes it to state $|2\rangle$, and a $\frac{\pi}{2}$-pulse changes the state of the atom from $|1\rangle$ to an equal superposition of the two states. The amplitude and frequency of $P_2\left(t\right)$ oscillations depend on the detuning. Maximum amplitude and minimum oscillation frequency occur when the pulse is on resonance. As the detuning increases, oscillations happen faster but amplitude decreases.
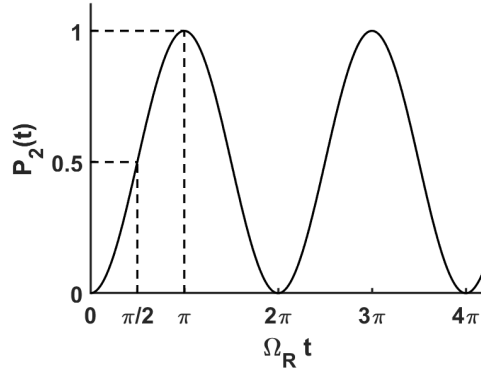
Figure 3.1: Probability of finding an atom in the excited state $|2\rangle$ when it is initially in the ground state $|1\rangle$ and the Rabi pulse is on resonance, i.e. $\Omega'_R = \Omega_R$. In this Rabi-flopping phenomenon, when $\Omega'_R t = \pi$, the pulse is called a π-pulse and when $\Omega'_R t = \pi/2$, it is called a $\frac{\pi}{2}$-pulse. A resonant π-pulse maximizes the probability of finding the atom in the excited state and a resonant $\frac{\pi}{2}$-pulse changes the state of an atom from the ground state to an equal superposition of the ground and excited states.

3.1.2 Bloch sphere representation of the spin state

The spin state $|S\rangle$ of a two-level spin system can be represented as a vector $\vec{S}$ on a so-called Bloch sphere, illustrated in Fig. 3.2. In this representation, the spin vector $\vec{S}$ is also referred to as the Bloch vector. The Bloch sphere exists in an abstract three-dimensional space with axes $u - v - w$. Evolution of the internal state of an atom can be visualized by the motion of $\vec{S}$ in this representation. In our system, the axes of the Bloch sphere do not coincide with the spatial coordinate axes because the states are not real spin-1/2 states. Our system is

referred to as a peudo-spin-1/2, and like any other two-level system, it is possible to map it onto the Bloch sphere.

The components of the spin vector along the axes of the Bloch sphere are

$$\vec{S} = S_u \hat{u} + S_v \hat{v} + S_w \hat{w}. \tag{3.4}$$

Here, S_w is referred to as the longitudinal spin component $(S_\parallel)$. (S_u, S_v) are the two components of the transverse spin $\left(\vec{S}_\perp\right)$, which lies in the horizontal plane (the $u-v$ plane) of the Bloch sphere. The azimuthal angle ϕ of $\vec{S}$ is the relative phase between the transverse spin components. The ground and excited states are the basis states where $|1\rangle$ points to the south pole of the Bloch sphere and $|2\rangle$ to the north pole. When the spin state is an equal superposition of the two basis states, we have

$$|S\rangle = \frac{1}{\sqrt{2}} \left(|1\rangle + e^{\mathrm{i}\phi} |2\rangle \right), \tag{3.5}$$

which lies in the equatorial plane of the Bloch sphere.
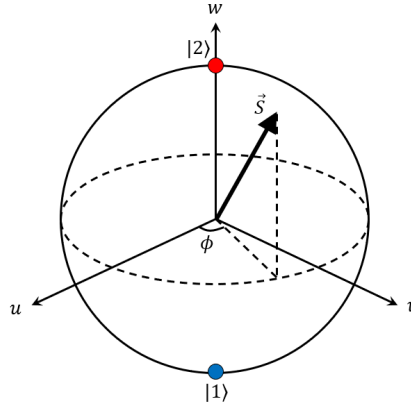
Figure 3.2: Bloch sphere representation of the spin state vector $\vec{S}$. In this visualization of our two-level system, the south pole is associated with the ground state $|1\rangle$ and the north pole with the excited state $|2\rangle$. A purely longitudinal spin state would lie on the w-axis and a purely transverse spin state would exist in the $u-v$ plane. The azimuthal angle (ϕ) is the relative phase between the two transverse components.

When the atom interacts with an oscillating field, the effective Rabi vector can be thought of as a torque vector, with components $\vec{\Omega}'_R = \Omega_R \hat{u} + \delta \hat{w}$, acting on the spin state vector according to

$$\frac{d\vec{S}}{dt} = \vec{\Omega}'_R \times \vec{S}. \tag{3.6}$$

Eqn. 3.6 describes a motion in which the Bloch vector $\vec{S}$ precesses around the torque vector $\vec{\Omega}'_R$. During this precession, the tip of the Bloch vector remains on the sphere, so the magnitude of $\vec{S}$ remains the same. In this picture, the transverse component of $\vec{S}$ is associated with internal coherence.

When the coupling field is resonant, $\vec{\Omega}'_R$ points along the u-axis, and the spin state

vector would precess around the u-axis of the Bloch sphere. A resonant π-pulse and $\frac{\pi}{2}$-pulse applied to a spin vector initially in the state $|1\rangle$ are schematically shown in Fig. 3.3. If the detuning is not zero ($\delta \neq 0$), $\vec{\Omega}'_R$ would point away from the u-axis. Depending on the sign of detuning, it could point up or down, and applying a Rabi pulse would make $\vec{S}$ rotate around $\vec{\Omega}'_R$ without fully going through state $|2\rangle$.

<center>(a) (b)</center>
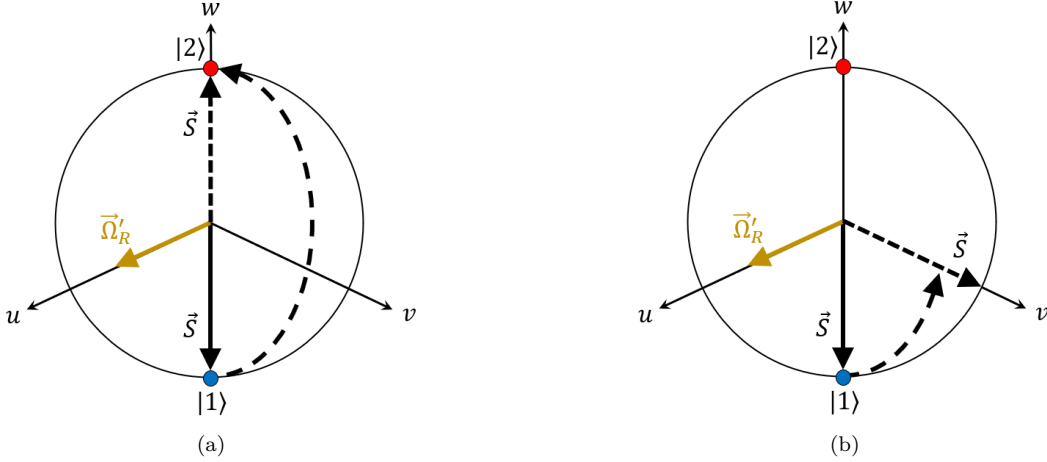
Figure 3.3: Depiction of resonant (a) π-pulse and (b) $\frac{\pi}{2}$-pulse when initially the atom is in the ground state $|S\rangle = |1\rangle$. When a Rabi pulse is applied, the spin state vector $\vec{S}$ precesses around the effective Rabi vector $\vec{\Omega}'_R$. If there is no detuning, $\vec{\Omega}'_R$ points along the u-axis, and Rabi pulses become resonant. Curved dashed lines indicate the trajectory of $\vec{S}$. Straight dashed lines show the final state of the state vector, which is (a) the excited state $|2\rangle$ for a π-pulse, and (b) a pure transverse state for a $\frac{\pi}{2}$-pulse.

3.2 Spin dynamics

3.2.1 Ultracold atoms

At a given temperature T, the spatial extent of the wave function of an atom with mass m can be characterized by its thermal de Broglie wavelength

$$\lambda_{\mathrm{dB}} = \sqrt{\frac{2\pi\hbar^2}{mk_BT}}, \tag{3.7}$$

where k_B is the Boltzmann constant. When λ_{dB} is larger than the two-body interaction length, the binary collisions between indistinguishable particles lead to coherent exchange interactions. In our system, the relevant collision length scale is the s-wave scattering length a, which sets the effective range of interaction for two atoms. The thermal de Broglie wavelength grows with decreasing temperature, and at ultracold temperatures, it can become much larger than the scattering length. In this work, $T = 650\,\mathrm{nK}$ is the typical operating temperature, which gives $\lambda_{\mathrm{dB}} \simeq 233\,\mathrm{nm}$. For ^{87}Rb, the scattering length is about 100 times

the Bohr radius, so $a \simeq 5.3\,\mathrm{nm}$; therefore, $\lambda_{\mathrm{dB}} \gg a$. This large ratio between the thermal de Broglie wavelength and scattering length means that during collisions, the wave functions of the two atoms have a large overlap, which necessitates wave function symmetrization with respect to atom exchange due to the indistinguishability of the colliding particles. A consequence of this symmetrization is a rotation of individual spins about their mean spin, which appears as a spin-torque term in the governing spin kinetic equation that is discussed next.

3.2.2   Spin Boltzmann equation

In the rest of this Chapter, the theory of spin diffusion of a two-level system trapped in a harmonic potential is described. The discussions follow the work in Refs. [19, 20]. In the notation here, the symbol $\perp$ refers to the radial direction, and z represents the axial direction of the trapped ensemble.

The mean-field interaction strength for two scattering particles of mass m is $g_{ij} = 4\pi\hbar^2 a_{ij}/m$ $(i, j = 1, 2)$, where a_{ij} is the s-wave scattering length between the two states. For ^{87}Rb, $a_{11} = 100.9a_0$, $a_{12} = 98.2a_0$, $a_{22} = 95.6a_0$, where a_0 is the Bohr radius [21]; therefore, it is reasonable to make the approximations $a_{11} \simeq a_{12} \simeq a_{22} \equiv a$, and $g_{11} \simeq g_{12} \simeq g_{22} \equiv g$. Accounting for the small differences in the scattering lengths leads to a slow decay in the transverse spin in the order of 10 seconds or more [22].

To describe the dynamics of this ensemble of pseudo-spin-1/2 particles, a semiclassical approach can be taken. In this approach, the motion of atoms is described in terms of a phase-space distribution function, where the phase-space variables are position ($\mathbf{r}$) and momentum ($\mathbf{p}$) of the atoms. The density distributions of atoms and spins are indicated by $f(\mathbf{r}, \mathbf{p}, t)$ and $\vec{\sigma}(\mathbf{r}, \mathbf{p}, t)$, respectively. The total number density is obtained from adding the number density in each state, which is given by

$$n(\mathbf{r}, t) = n_1(\mathbf{r}, t) + n_2(\mathbf{r}, t) = \int d\mathbf{p} f(\mathbf{r}, \mathbf{p}, t)/(2\pi\hbar)^3 .$$

The spin density is given by

$$\vec{S}(\mathbf{r}, t) = \int d\mathbf{p}\, \vec{\sigma}(\mathbf{r}, \mathbf{p}, t)/(2\pi\hbar)^3 .$$

The longitudinal spin component represents the relative number density: $S_w = n_2 - n_1$. Internal coherence is the magnitude ($S_\perp$) of the transverse spin $\vec{S}_\perp = S_\perp e^{i\phi}$, and ϕ is the relative phase between the components (S_u, S_v) of the transverse spin.

The magnetic trapping potential is

$$U_{\mathrm{ext}}(\mathbf{r}) = \frac{1}{2}m\omega_z^2 \left[\alpha^2 \left(x^2 + y^2\right) + z^2\right],$$

where α is the trap aspect ratio. The effective center-of-mass potential is

$$U_n(\mathbf{r}, t) = U_{\mathrm{ext}}(\mathbf{r}) + g_{11}n_1(\mathbf{r}, t) + g_{22}n_2(\mathbf{r}, t) + g_{12}\left[n_1(\mathbf{r}, t) + n_2(\mathbf{r}, t)\right]/2.$$

The effective coupling field is given by

$$\vec{\Omega}_n \left(\mathbf{r}, t \right) = \vec{\Omega}'_n \left(\mathbf{r}, t \right) + \frac{g_{12}}{\hbar} \vec{S} \left(\mathbf{r}, t \right), \tag{3.8}$$

where

$$\vec{\Omega}'_n \left(\mathbf{r}, t \right) = \left\{ \Omega_u \left(\mathbf{r} \right), \Omega_v \left(\mathbf{r} \right), \Omega_w \left(\mathbf{r} \right) + \Delta_{\mathrm{MF}} \left(\mathbf{r}, t \right) \right\},$$

with $\left\{ \Omega_u, \Omega_v, \Omega_w \right\}$ being the components of the coupling field vector $\vec{\Omega} \left(\mathbf{r} \right)$ (see below), and Δ_{MF} is the mean-field frequency shift.

The coupled Boltzmann equations for $f \left(\mathbf{r}, \mathbf{p}, t \right)$ and $\vec{\sigma} \left(\mathbf{r}, \mathbf{p}, t \right)$ are given by

$$\frac{\partial f}{\partial t} + \frac{\mathbf{p}}{m} \cdot \nabla f - \nabla U_n \cdot \nabla_p f - \frac{\hbar}{2} \sum_{i=u,v,w} \nabla \Omega_{ni} \cdot \nabla_p \sigma_i = \left. \frac{\partial f}{\partial t} \right|_{\mathrm{coll}}, \tag{3.9}$$

$$\frac{\partial \vec{\sigma}}{\partial t} + \frac{\mathbf{p}}{m} \cdot \nabla \vec{\sigma} - \nabla U_n \cdot \nabla_p \vec{\sigma} - \frac{\hbar}{2} \nabla \vec{\Omega}_n \cdot \nabla_p f - \vec{\Omega}_n \times \vec{\sigma} = \left. \frac{\partial \vec{\sigma}}{\partial t} \right|_{\mathrm{coll}}. \tag{3.10}$$

The right-hand sides of Eqn 3.9 and 3.10 are the elastic collision integrals, which are given in Ref. [19].

It is possible to decouple Eqn. 3.9 and 3.10 by considering energy scales. In both of these equations, the third and fourth terms scale like $gn/k_B T$. At the operating conditions in this work, the typical values are $T = 650 \, \mathrm{nK}$ and $n_0 = 2 \times 10^{19} \, \mathrm{m}^{-3}$ for temperature and peak density, making $k_B T = 13.5 \, \mathrm{kHz} \times \mathrm{h}$ and $gn_0 = 155 \, \mathrm{Hz} \times \mathrm{h}$; therefore, $gn/k_B T \ll 1$. Dropping the third and fourth terms in both Boltzmann equations leads to their decoupling, and the Boltzmann equation of the spin density distribution becomes

$$\frac{\partial \vec{\sigma}}{\partial t} + \frac{\mathbf{p}}{m} \cdot \nabla \vec{\sigma} - \nabla U_{\mathrm{ext}} \cdot \nabla_p \vec{\sigma} - \vec{\Omega}_n \times \vec{\sigma} = \left. \frac{\partial \vec{\sigma}}{\partial t} \right|_{\mathrm{coll}}. \tag{3.11}$$

In our system, $\alpha \gg 1$ (see Section 2.3), which makes the geometry of the system quasi-one-dimensional. It is therefore preferable to convert Eqn. 3.11 into a one-dimensional equation. Using the ansatz $\vec{\sigma} \left(\mathbf{r}, \mathbf{p}, t \right) = \vec{\sigma} \left(z, p, t \right) h_0 \left(\mathbf{r}_\perp, \mathbf{p}_\perp \right)$, where the static radial profile is $h_0 = \exp \left[- \left(p_\perp^2 / 2m + m \omega_\perp^2 r_\perp^2 / 2 \right) / k_B T \right]$, and integrating over the phase-space variables, Eqn. 3.11 further simplifies to the 1D spin Boltzmann equation

$$\frac{\partial \vec{\sigma}}{\partial t} + \frac{p}{m} \frac{\partial \vec{\sigma}}{\partial z} - \frac{\partial U_{\mathrm{ext}}}{\partial z} \frac{\partial \vec{\sigma}}{\partial p} - \vec{\Omega}_n \times \vec{\sigma} = \left. \frac{\partial \vec{\sigma}}{\partial t} \right|_{\mathrm{1D}}. \tag{3.12}$$

The RHS of Eqn. 3.12 represents damping of excitations due to elastic collisions. In our system, the observable is the spatial distribution of spin

$$\vec{S} \left(z, t \right) = \frac{1}{2 \pi \hbar} \int dp \, \vec{\sigma} \left(z, p, t \right). \tag{3.13}$$

The spin-torque term $\vec{\Omega}_n \times \vec{\sigma}$ in Eqn. 3.12 acts as an effective magnetic field, and makes the dynamics non-linear. In the absence of an external coupling field, $\Omega_u \left(z \right) = \Omega_v \left(z \right) = 0$, and

$$\Omega_w \left(z \right) = \Delta \left(z \right) = U_{\mathrm{diff}} \left(z \right) / \hbar, \tag{3.14}$$

is the frequency splitting between the two states across the ensemble. U_{diff} is the differential potential, which is defined as the energy difference between the two states across the cloud. These conditions therefore make

$$\vec{\Omega}_n \times \vec{\sigma} = \left(U_{\text{diff}}\hat{w} \times \vec{\sigma} + g\vec{S} \times \vec{\sigma} \right) / \hbar. \tag{3.15}$$

The cross-product $\vec{S} \times \vec{\sigma}$ in Eqn. 3.15 leads to the so-called identical spin rotation effect, which is further discussed below.

When the differential potential is uniform, we can make another reference frame transformation to make $U_{\text{diff}} = 0$. From this change, we get $\vec{\Omega}_n = g\vec{S}/\hbar$, which further simplifies Eqn. 3.12 to

$$\frac{\partial \vec{\sigma}}{\partial t} + \frac{p}{m}\frac{\partial \vec{\sigma}}{\partial z} - \frac{\partial U_{\text{ext}}}{\partial z}\frac{\partial \vec{\sigma}}{\partial p} - \frac{g}{\hbar}\vec{S} \times \vec{\sigma} = \frac{\partial \vec{\sigma}}{\partial t}\bigg]_{\text{1D}}. \tag{3.16}$$

3.2.3   Identical spin rotation effect (ISRE)

The term $\vec{S} \times \vec{\sigma}$ in Eqn. 3.15 leads to rotation of the spins of two colliding particles around their combined spin. The physical effect giving rise to this term is quantum particle indistinguishability [5]. Figure 3.4 schematically shows that for two colliding ultracold atoms, the thermal de Broglie wavelength is larger than the scattering length. Thus, in a cold collision it cannot be determined which particle scatters forward and which backward, leading to the requirement of symmetrization of the two-body wave function. This symmetrization leads to spin rotation of each colliding atom around their mean spin. This phenomenon is referred to as the identical spin rotation effect.

The ISRE is essentially an exchange effect during a collision, which in general changes the internal state of the two colliding atoms. An example of this process is depicted in Fig. 3.5 in which two purely transverse spins with a relative phase difference moving in opposite directions collide and, due to the ISRE, they end up with opposite longitudinal components after the collision. Neither longitudinal nor transverse component of individual spins is conserved by the ISRE. However, in a binary interaction governed by the ISRE, the total spin and hence the total energy of the system remains the same because the spins precess together around the net spin, conserving the total spin [23].

Orthogonal spins are not modified by the ISRE as the combined spin of the colliding particles would be zero. Orthogonality here refers to states in the Hilbert space. With regards to the ISRE, the ensemble is at equilibrium if the atoms are in a uniform binary mixture of states $|1\rangle$ and $|2\rangle$.

On a macroscopic scale, the ISRE can modify transport properties of gases with internal states [24]. It is not easy to predict the dynamics of the entire cloud based on the rotation effect in a few collisions. In any case, the ISRE can convert binary collisions to collective spin behavior. The strength of the ISRE can be quantified by the parameter

$$\mu = gn\tau_{\text{cl}}/\hbar, \tag{3.17}$$

with the radially averaged mean-collision time given by [19]
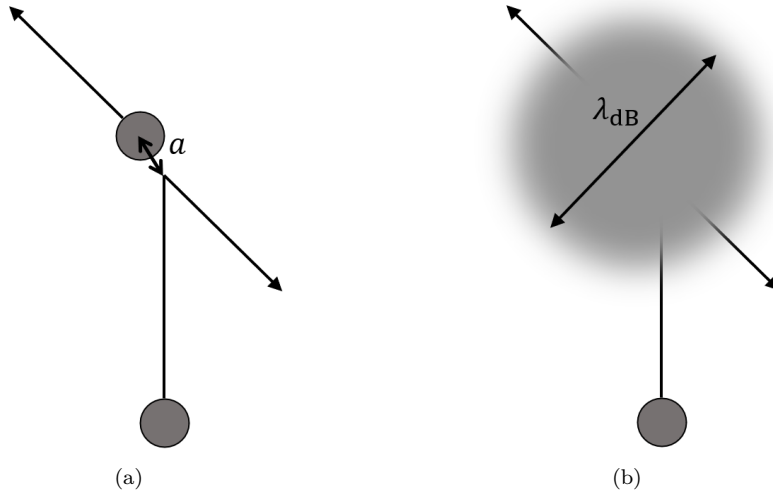
Figure 3.4: Schematic illustration of collision of two (a) distinguishable and (b) indistinguishable atoms. Each small circle represents an atom. Since $\lambda_{dB} \propto 1/\sqrt{T}$, the thermal de Broglie wavelength λ_{dB} is smaller than the scattering length a at higher temperatures T, and the colliding atoms are distinguishable as in (a). At ultracold temperatures like (b), we have $\lambda_{dB} \gg a$, and the atoms become indistinguishable in a collision, making it necessary for the the wave function to be symmetrized with respect to a particle exchange. The identical spin rotation effect is a consequence of this symmetrization.

$$\tau_{\text{cl}}(z) \simeq \left[16a^2 n(z) \sqrt{\pi k_{\text{B}} T/m}\right]^{-1}. \tag{3.18}$$

In physical terms, the parameter μ is the ratio of the exchange frequency to the elastic scattering rate. Since $\mu \propto 1/\sqrt{T}$, the ISRE strengthens as temperature decreases, and becomes the dominant effect compared to classical elastic scattering.

The next Chapter uses the concepts presented in this and the previous Chapters to discuss the steps for initializing spin-state profiles and measuring evolution of spin domains.

(a)

(b)

(c)
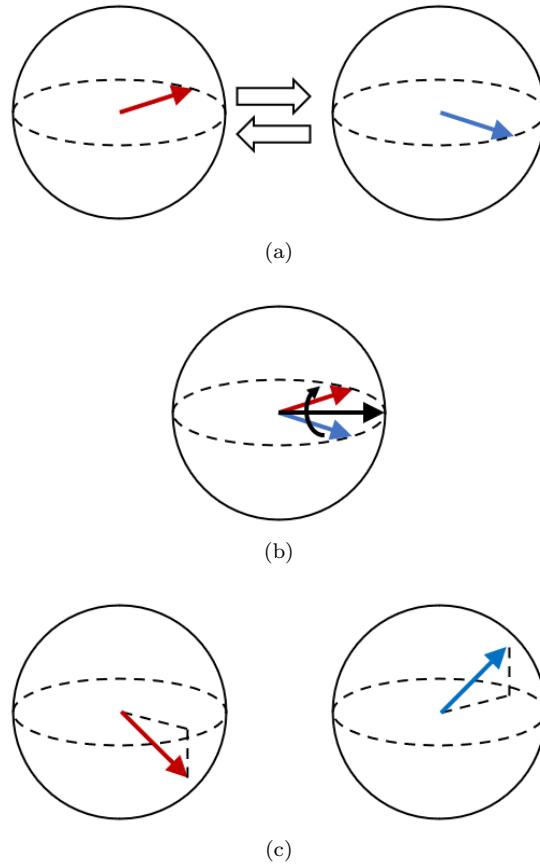
Figure 3.5: Schematic example of the ISRE. Each Bloch sphere represents an atom with a particular spin shown as an arrow. (a) Before the collision, the two spins are purely transverse with a relative phase difference. (b) During the collision, the two spins precess around their mean (the black arrow). (c) After the collision, the two spins have obtained opposite longitudinal components. The degree of rotation of the spins in a collision depends on the ISRE strength, which increases as the temperature decreases.

Chapter 4

Spin profile preparation and evolution

In Chapter 2, the steps before and after an experiment were explained. In particular, it included the two cooling techniques, and the procedures for imaging the ultracold trapped atoms. Chapter 3 discussed the relevant background theory for our system, including concepts of π- and $\frac{\pi}{2}$-pulses. This Chapter builds on the previous discussions to explain how the experiment is actually initialized and controlled. After presenting the two-level system in more detail, creation of uniform differential potentials across the cloud is described. The invaluable Ramsey method of spectroscopy used for measuring the differential potential is discussed, too. The patterning of light from a laser to "paint" spin textures on the cloud is explained. Finally, initialization of spin profiles and measurement of the evolution of the system is presented.

4.1   The experimental two-level system

The atomic species we use is rubidium-87. The experimental two-level system is made of two magnetically trapped Zeeman sublevels of its hyperfine ground states, namely $|1\rangle = |F = 1, m_F = -1\rangle$ and $|2\rangle = |F = 2, m_F = 1\rangle$, where F and m_F denote the total angular momentum and magnetic quantum numbers, respectively. The magnetic moments of these two state are nearly the same, which makes them equally trapped by the magnetic field.

Since these two states are different by two units of angular momentum, they cannot be coupled by a single photon transition. As shown in Fig. 4.1, the coupling is achieved by a two-photon process in which a $\sim 6.8\,\mathrm{GHz}$ microwave photon and a $\sim 3\,\mathrm{MHz}$ rf photon are used. Both photons are detuned from the intermediate state $|F = 2, m_F = 0\rangle$ by about $700\,\mathrm{kHz}$ so that excitations to this level are avoided. The Zeeman shifts across the cloud are not uniform due to nonuniformity of the trapping potential. However, in small magnetic fields both $|1\rangle$ and $|2\rangle$ states experience equal first-order Zeeman shifts; therefore, the spatial inhomogeneities in Zeeman shifts are negligible and the same two photons can couple the two Zeeman states across the cloud.
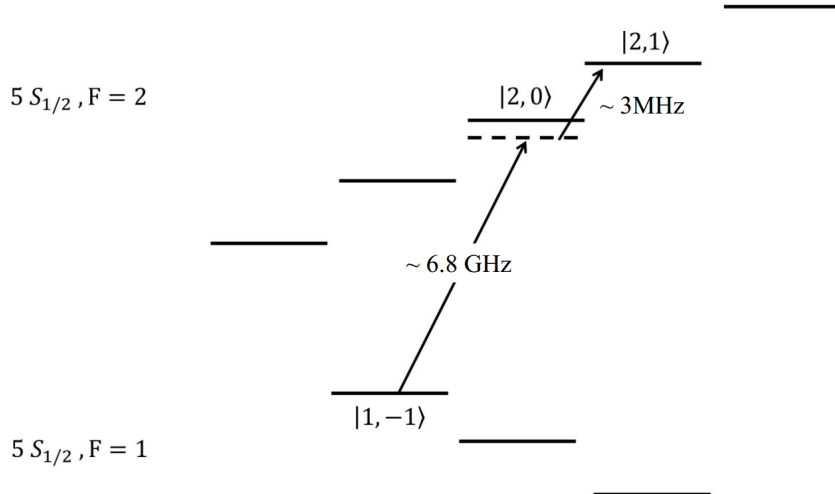
Figure 4.1: Zeeman sublevels of the two ground hyperfine levels of the $5S_{1/2}$ manifold of ^{87}Rb. Trapped states $|F = 1, m_F = -1\rangle$ and $|2, 1\rangle$ constitute the two-level system in this work. The two states are coupled by a microwave photon and an rf photon, which are detuned from the intermediate state $|2, 0\rangle$ to avoid real transitions to that state. The energy separations are not drawn to scale.

4.2 Cancellation spot

The differential potential can be written as $U_{\text{diff}} = hf_{12}$, where f_{12} is the transition frequency. The precession rate of the transverse spin around the longitudinal axis of the Bloch sphere is a function of the differential potential. If there is no inhomogeneity in U_{diff} across the cloud, the associated Larmor precession frequency can be eliminated by moving to an appropriate rotating reference frame. However, in general U_{diff} varies with the axial position z, and its spatial inhomogeneities can lead to smaller coherence times in the experiment. It is thus desirable to make U_{diff} as uniform as possible.

There are three sources that contribute to the U_{diff} axial profile. One is the mean-field shift, which is a result of collisional interactions between the atoms. Another is the Zeeman shift produced by the trapping magnetic field. The third source is the ac Stark shift, which can be induced by an off-resonant laser. In the work of this thesis, the laser light is only used to prepare the initial spin profile of the cloud (see Section 4.4) and the beam is immediately turned off after the initialization. In these cases, U_{diff} would only be set by the mean-field and Zeeman shifts.

In general, the shifts from the mean-field and Zeeman effect do not cancel each other. Through what is called a mutual compensation scheme [21], it is possible to adjust the effects of the two energy-shifting schemes such that they would cancel each other. The rest of this Section explains how the differential potential is made spatially uniform in our system, and how it is measured using the Ramsey method of spectroscopy.

4.2.1 Making U_{diff} uniform

Collisions between atoms can lead to a shift in their energy levels. This mean-field component of the differential potential is given by [13]

$$\Delta_{\text{MF}}(z) = \frac{4\pi\hbar^2}{m}\left\{2a_{22}n_2(z) - 2a_{11}n_1(z) + 2a_{12}\left[n_1(z) - n_2(z)\right]\right\}. \qquad (4.1)$$

As the atomic sample has a Gaussian density profile, the mean-field collisional shift, which scales with the atomic density, also has a Gaussian profile.

Since the atoms are trapped in a magnetic field in the science cell, the degeneracy in the magnetic quantum number m_F is removed. For intermediate magnetic fields B, the Breit-Rabi formula for $J = 1/2$ (which is the case for the $5S_{1/2}$ ground state considered here) gives the shift in each m_F energy level [13]

$$E\left(F = I \pm \frac{1}{2}, m_F\right) = \frac{-\Delta E_{\text{hf}}}{2(2I+1)} - g_I m_F \mu_B B \pm \frac{\Delta E_{\text{hf}}}{2}\sqrt{1 + \frac{4m_F}{2I+1}x + x^2}, \qquad (4.2)$$

where

$$x = \frac{(g_I + g_J)\mu_B B}{\Delta E_{\text{hf}}}. \qquad (4.3)$$

Here, g_I and g_J are the nuclear and Lande g-factors, respectively. ΔE_{hf} is the hyperfine splitting between the two states ($F = 1$ and 2) in zero B-field. For ^{87}Rb, the nuclear spin $I = 3/2$.

At a so-called magic spot of $B_0 \sim 3.23\,\text{G}$, Eqn. 4.2 gives a minimum for the differential potential. In the vicinity of the magic spot, the differential Zeeman shift is first-order independent of B, so the transition frequency can be written as $f_{12}(z) = f_{\text{min}} + b\left[B(z) - B_0\right]^2$ where b is a constant and f_{min} is the transition frequency at the local minimum. The magnetic field near the magic spot can be approximated as $B(z) = B_{\text{bias}} + \frac{1}{2}B''z^2$. Hence, $f_{12}(z)$ can be written as

$$f_{12}(z) = f_{\text{min}} + b(B_{\text{bias}} - B_0)^2 + b\left[\left(\frac{B''}{2}\right)^2 z^4 + (B_{\text{bias}} - B_0)B''z^2\right]. \qquad (4.4)$$

The quadratic term $(B_{\text{bias}} - B_0)^2$ in Eqn. 4.4 does not depend on z, so it can be absorbed into f_{min}. About $100\,\text{mG}$ away from B_0, the term $\left(\frac{B''}{2}\right)^2 z^4$ can also be ignored, further simplifying $f_{12}(z)$ to

$$f_{12}(z) = f_{\text{min}} + b(B_{\text{bias}} - B_0)B''z^2, \qquad (4.5)$$

showing that the differential Zeeman shift has a quadratic dependence on position near the magic spot. The control parameter here is the bias magnetic field B_{bias}, and by changing its value, the differential Zeeman shift can be adjusted.

Since the Zeeman shift has a quadratic profile and the mean-field shift has a Gaussian profile, it is possible to approximately flatten the differential potential by adjusting the trapping magnetic field or the density of the atoms in such a way that these two would cancel each other. Figure 4.2 displays this mutual compensation schematically. With this

method, a perfect cancellation is not possible as a parabola and a Gaussian do not exactly cancel each other. In the work of this thesis, the density of the atoms is chosen first; therefore, the parameter to be adjusted to obtain a uniform differential potential is the bias magnetic field. If the density changes, the mean-field shift would also change, and the counteracting Zeeman shift would occur at a different cancellation spot; thus the magnetic field would have to be adjusted accordingly.
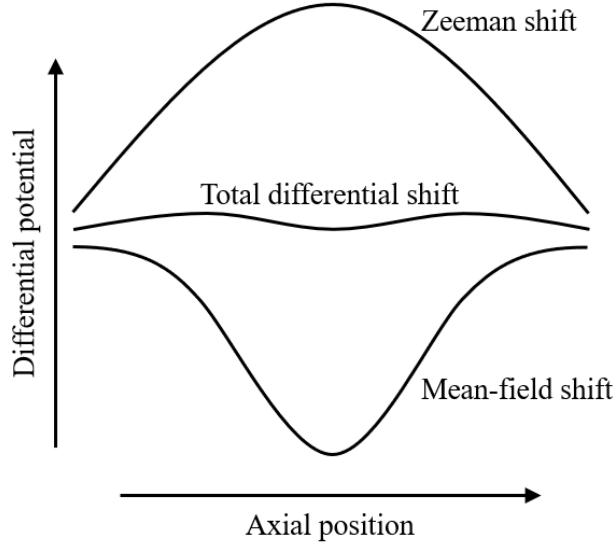

Figure 4.2: Schematic representation of the mutual compensation scheme. The Gaussian mean-field shift and the roughly quadratic Zeeman shift almost cancel each other, which makes the total differential potential across the ensemble approximately flat. The parameter that we adjust is the magnetic field and hence the differential Zeeman shift.

4.2.2 Measuring U_{diff} with Ramsey spectroscopy

In this work, the differential potential is measured via the Ramsey method of spectroscopy. Figure 4.3 shows a schematic of the procedures in this method, in which there are two Rabi pulses with duration τ and a free evolution time of interval T in between. The pulses are resonant two-photon pulses. To maximize the amplitude of the Ramsey fringes, both pulses are $\frac{\pi}{2}$-pulses. A $\frac{\pi}{2}$-pulse takes an atom in spin state $|1\rangle$ to the transverse plane with state

$$|S\rangle = \frac{1}{\sqrt{2}}\left(|1\rangle + e^{i\phi}|2\rangle\right). \tag{4.6}$$

The amplitude of Ramsey fringes is a measure of the magnitude of the transverse component of spin. A $\frac{\pi}{2}$-pulse maximizes the transverse component, which improves the signal-to-noise ratio.

During the evolution time, the frequency of the local oscillator generating the pulses is ω. Denoting the resonant frequency of the atoms by ω_0, the detuning is defined as the difference between these two frequencies: $\delta = \omega_0 - \omega$. When $\delta \neq 0$, the transverse spin accumulates phase with respect to the oscillator during the evolution time. The second
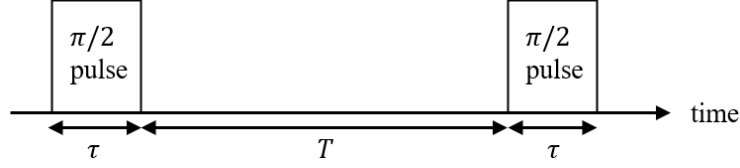
Figure 4.3: Procedures in the Ramsey method of spectroscopy for measuring the differential potential. The durations are not drawn to scale since $\tau \ll T$. To maximize the amplitude of Ramsey fringes, both Rabi pulses are $\frac{\pi}{2}$-pulses. Fringes are obtained by sampling at different evolution time T.

Rabi pulse converts the accumulated phase into a probability distribution for the atom being in the ground or excited state. For $\delta \ll \Omega_R$ and $\tau \ll T$, the probability of finding an atom in state $|2\rangle$ after time T is given by

$$P_2\left(\delta, T\right) = \frac{1}{2}\left[1 + \cos\left(\delta T\right)\right].$$

(4.7)

To obtain Ramsey fringes, data is acquired at different T values. A sinusoid is fit to find the frequency. Figure 4.4 shows an example of a typical Ramsey measurement.
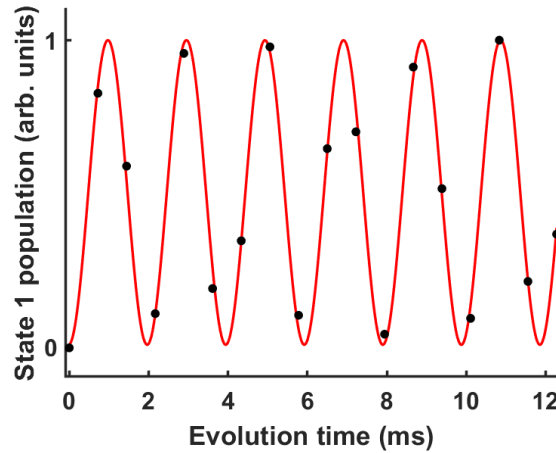
Figure 4.4: Example of a Ramsey measurement. A sinusoid is fit to extract parameters.

The evolution of the relative phase $\phi\left(z, t\right)$ is proportional to the relative energy difference between the two states, i.e. the differential potential. Across the cloud, $\phi\left(z, t\right)$ is given by

$$\phi\left(z, t\right) = \left(\frac{U_{\mathrm{diff}}\left(z\right)}{\hbar}\right) t.$$

(4.8)

Spatial variations of the differential potential can be effectively found by measuring the frequency of Ramsey oscillations across the cloud. Figure 4.5 shows a flat differential potential profile that has been obtained by adjusting the Zeeman shift to cancel the mean-field shift. This cancellation is for an equal ratio of populations of the two states. Nonetheless, since the s-wave scattering lengths are almost equal for the two states ($a_{11} \simeq a_{12} \simeq a_{22}$), U_{diff} remains fairly flat for other population ratios as well.

Figure 4.5: Example of flat U_diff, achieved by adjusting the Zeeman shift to cancel the mean-field collisional shift across the could. The common hyperfine splitting between the two states has been subtracted. The red line is a fit to the central region, which has a slope of 0 Hz/mm. Error bars are fit uncertainties to Ramsey oscillations as in Fig. 4.4. Error bars away from the central region gro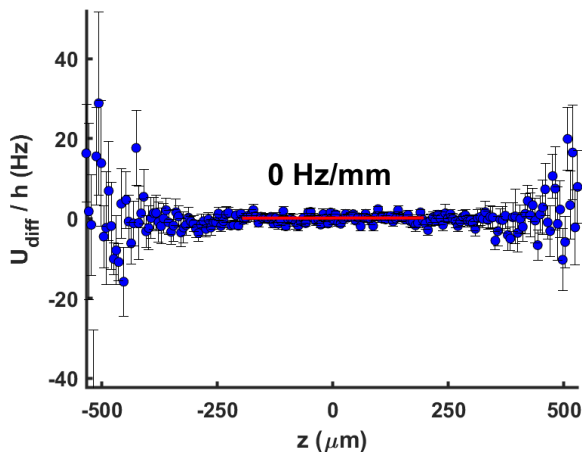w because the SNR drops towards the tails of the Gaussian distribution of atoms. The fact that U_diff is less uniform toward the sides of the cloud does not substantially affect the dynamics because the atom density is relatively very small in those regions.

4.3 Making patterned light

In this work, off-resonant patterned light is used for initializing spin profiles. To make patterned light, we use a laser beam and a digital micromirror device (DMD). To initialize spin profiles, patterned light with appropriate laser beam intensity together with two-photon microwave pulses are used. Details of the procedures for spin profile initialization are discussed in Section 4.4. This Section focuses on how the light is actually patterned.

A DMD is a matrix of mirrors that can be individually controlled to two possible rotation angles, which are referred to as "on" and "off" positions. When an image is uploaded to the DMD, each pixel corresponds to one mirror. The DMD image is uploaded to the memory of the DMD before the experiment begins. The pattern of the image is chosen based on its application.

Depending on the status of the DMD mirrors, the reflected light from the DMD takes one of two paths: if the mirror is in the "off" position, the reflected light goes in a direction that does not reach the atoms; if the mirror is in the "on" position, the reflected light goes through a path that is eventually focused on the atoms by the DMD optics.

Figure 4.6 schematically shows the optical setup of the DMD. Laser light from a single-mode fiber is passed through a collimating lens. The DMD reflects this collimated beam. Positions of the DMD mirrors gives the reflected beam a specific pattern. The patterned light passes through an imaging lens and illuminates the atom cloud. The two lenses are achromatic doublets to reduce spherical aberrations. This setup is for direct imaging and the magnification is $\sim 1/12$.

Since the atom cloud is quasi-one-dimensional, the DMD patterns are made such that
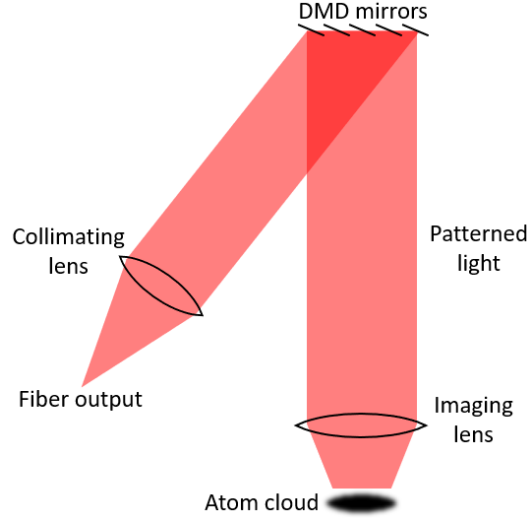
Figure 4.6: DMD optical setup for direct imaging of the DMD pattern onto the atoms. The DMD is illuminated by a collimated beam. Depending on the positions of the DMD patterns, the reflect light obtains a specific pattern, which is then shined on the atoms.

all the mirrors in one column are either on or off; in other words, although the DMD is a 2D matrix of mirrors, we effectively use it as a 1D array of mirrors. In this thesis, each column of the DMD mirrors will be referred to as a "DMD bin."

For certain reasons, one of which is explained in Chapter 5, it is sometimes needed to make the Stark beam intensity have particular spatial variations. To make intensity profiles, one needs a grayscale image. In places where pixels would be closer to white (black), the intensity would be larger (smaller). The requirement, though, is that to make a grayscale image, the mirrors of the DMD should be able to rotate to more than two possible positions.

One solution to produce an arbitrary grayscale pattern with the DMD is to binarize a grayscale image. The idea is to make an image in which each pixel value is in the range of 0 to $2^N - 1$, where N is the number of pixel bits. Then, using an error diffusion algorithm, the grayscale image is converted to a binary image so that each pixel would be 1 bit. The number of required bits depends on the application. If variations in light intensity is large, N should be larger to allow for smoother changes in the DMD image. For the work in this thesis, $N = 8$ bits proved to be good enough. With 8 bits, the value of each pixel can be in the range of 0 to 255, where 0 would be black, 255 would be white, and pixel values in between would be shades of gray.

For the purpose of image binarization, there are various error diffusion kernels. In image processing, a kernel is typically a small matrix that is used for various processes such as finding the edges in an image. For this thesis work, the Sierra kernel was used because the image distortions after binarization would be minimum. Further details about the DMD can be found in Ref. [16].

4.4 Spin profile initialization and evolution

4.4.1 Spin profile initialization

To initialize a spin profile, we take advantage of the ac Stark effect caused by off-resonant laser light combined with a resonant cloud-wide π-pulse. When an atom is illuminated by the laser light, it develops an induced electric dipole moment as a result of interaction with the oscillating electric field of the light. The energy levels of the atom shift as a result of the interaction between this induced moment and the electric field. Near the D_1 and D_2 lines of alkali atoms, the dipolar interaction is given by the dipole potential [25]

$$U_{\text{dip}}(z) = \frac{\pi c^2 \Gamma}{2\omega_0^3} \left(\frac{2 + P g_F m_F}{\Delta_{2,F}} + \frac{1 - P g_F m_F}{\Delta_{1,F}} \right) I(z), \qquad (4.9)$$

where $I(z)$ is the spatial profile of the laser intensity, Γ is the natural linewidth of the excited state, $P = \{0, \pm 1\}$ for linearly and circularly polarized light, and g_F is the Lande g-factor. ω_0 is the transition frequency, which is the center of the D-line doublet $\left({}^2S_{1/2} \to {}^2P_{1/2}, {}^2P_{3/2} \right)$. $\Delta_{1,F}$ and $\Delta_{2,F}$ denote the energy difference between the specific ground state ${}^2S_{1/2}, F$ and the center of the hyperfine splitting of the excited states ${}^2P_{1/2}$ and ${}^2P_{3/2}$. The terms in parentheses in Eqn. 4.9 show that both the D_1 and D_2 lines contribute to the total dipole potential. However, for a detuning Δ close to the D_2 transition, $\Delta_{2,F} \ll \Delta_{1,F}$, the dipole potential simplifies to

$$U_{\text{dip}}(z) = \frac{\pi c^2 \Gamma}{2\omega_0^3} \left(\frac{2 + P g_F m_F}{\Delta_{2,F}} \right) I(z).$$

To minimize the spontaneous scattering rate, Δ should be chosen to be midway between the cooling and repumper transition frequencies such that $\Delta_{2,F}^{(1)} = -\Delta_{2,F}^{(2)}$, where the superscripts refer to the spin states $|1\rangle$ and $|2\rangle$ [16]. This choice makes the detuning $\Delta \sim 3.4\,\text{GHz}$ below the cooling transition (see Fig. 2.4). The Stark laser is locked using the phase-locked loop method (see Ref. [14] for further details).

When making patterned light, there will be dark and bright regions. In regions where the pattern is dark, i.e. no light, the effective Rabi vector $\vec{\Omega}'_\text{R}$ points along the u-axis on the Bloch sphere; therefore, a resonant π-pulse takes the atoms from state $|1\rangle$ to $|2\rangle$, as depicted in Fig. 4.7(a). If there is light, the pulse will have a detuning from the transition $|1\rangle \to |2\rangle$, and the vector $\vec{\Omega}'_\text{R}$ will be tilted away from the u-axis. Since the π-pulse is cloud-wide, in the illuminated regions, the detuning should be such that the pulse rotates the spin state vector $|S\rangle = |1\rangle$ around $\vec{\Omega}'_\text{R}$ and brings it back to state $|1\rangle$ at the end of the pulse duration so that atoms remain in state $|1\rangle$. Numerical simulations of the optical Bloch equations show that the optimal detuning of the effective Rabi vector is

$$\delta^* = \sqrt{3}\Omega_\text{R}, \qquad (4.10)$$

which is obtained by adjusting the Stark laser beam intensity [16]. This detuning makes the magnitude of the effective Rabi vector $\left| \vec{\Omega}'_\text{R} \right| = 2\Omega_\text{R}$ (see Eqn. 3.3), which changes a previously resonant π-pulse to be equivalent to a 2π-pulse on the detuned parts of the cloud (the parts that are illuminated by the laser). For this optimal effective Rabi vector, a resonant π-pulse would rotate a ground state Bloch vector $|S\rangle = |1\rangle$ around $\vec{\Omega}'_\text{R}$ once and

bring it back to the $|1\rangle$ state without going through state $|2\rangle$. The process is schematically shown in Fig. 4.7(b).

On the edges of the patterned light, the intensity gradually goes from bright to dark. In these small regions of the cloud, the pulse takes the state vector from $|1\rangle$ into a superposition of $|1\rangle$ and $|2\rangle$ with a smoothly changing transverse spin magnitude and phase. In these regions the spin vector takes a helical path, and makes a helical spin domain wall.
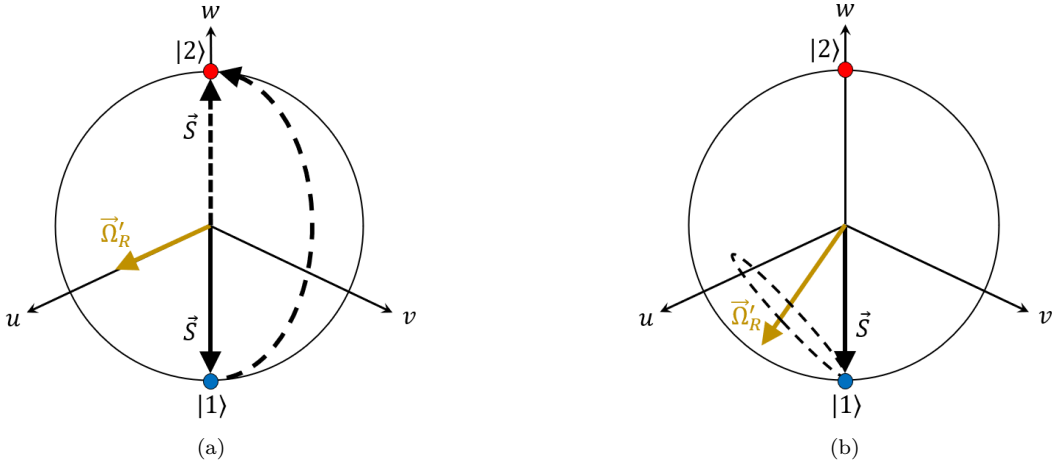

Figure 4.7: Schematic depiction of how a cloud-wide π-pulse changes state of the atoms from $|1\rangle$ (a) to $|2\rangle$ at dark regions of the light pattern, and (b) back to $|1\rangle$ at bright regions of the pattern with optimal detuning. The light that reaches the cloud is patterned by the DMD image. The change of the intensity from bright to dark is gradual and the pulse makes the spins take a gradual helical path, creating a helical spin domain wall between adjacent bright and dark regions of the light pattern.

In the beginning of spin profile initialization, all spins are in the state $|1\rangle$, and the DMD pattern is chosen based on what spin profile we want to create. For example, to make the three-domain spin structure $|2\rangle - |1\rangle - |2\rangle$, the patterned light must have a bright region in the middle and must be dark on the two sides, and after applying a cloud-wide π-pulse, the spin domains are constructed. Section 7.1 discusses how we characterize an initial three-domain spin profile, which is the main spin structure in this work. To make other spin profiles, we only need to change the DMD pattern accordingly.

4.4.2 Obtaining spin evolution data

To investigate evolution of the longitudinal spin, we start the system with the same initial conditions in each experimental cycle and let it evolve under the same conditions. The evolution is sampled by imaging the atoms at different times. For each evolution time, there are two experimental cycles, one for each of the two states. To measure atoms in state $|2\rangle$, an additional π-pulse is applied before the imaging procedure to swap the state of the atoms so that the ARP process transfers those atoms to the cycling transition for imaging (see Section 2.4).

Due to dipolar relaxation during $|2\rangle - |2\rangle$ collisions, atoms in this state can transfer to

states that are not trapped, and therefore some of them exit the trap. To remove the effects of this loss, we normalize the number of atoms in each state N_i $(i = 1, 2)$ at time t to their initial total number

$$N_i^{\mathrm{norm}}(z,t) \equiv N_i(z,t) \times \frac{\sum_z N_i(z, t = 0)}{\sum_z N_i(z, t)} \quad (i = 1, 2).$$ (4.11)

We do the same normalization for N_1 atoms too, although their population is almost constant during the evolution periods that are considered in this work. The normalization removes the loss effect absent in the dynamical equations and is an imaging enhancement technique to highlight features in the experiment. The longitudinal spin at time t is then found as

$$S_{||}(z,t) = N_2^{\mathrm{norm}}(z,t) - N_1^{\mathrm{norm}}(z,t).$$ (4.12)

To simplify notation, N_i will be used instead of N_i^{norm} in the rest of this thesis; however, it should be remembered that in all of the analysis in future Chapters, the normalized number of atoms is used.

Figure 4.8 shows a typical example of longitudinal spin evolution for a three-domain spin profile with uniform differential potential for short times. Blue (Red) is associated with atoms whose longitudinal spin is towards the south (north) pole of the Bloch sphere. White represents spin domain walls in which there is an equal number of atoms in the two states. Further results and discussions are presented in Chapter 7.
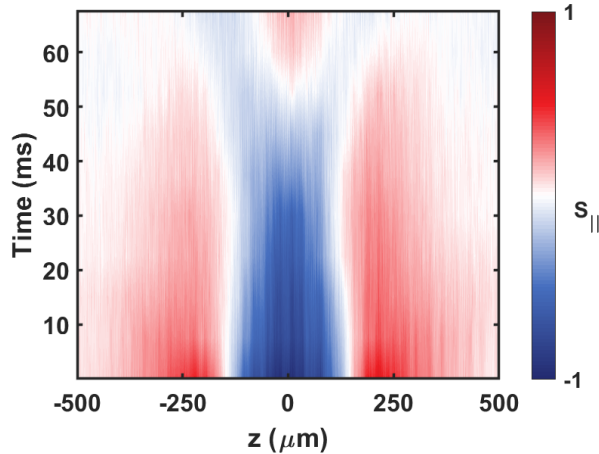

Figure 4.8: Data showing evolution of longitudinal spin $\left(S_{||}\right)$ of a three-domain spin structure in a uniform differential potential. In each experimental cycle, the system is initialized with the same conditions and allowed to evolve for various times. Atoms whose longitudinal spin component is towards the south (north) pole of the Bloch sphere are shown with blue (red) color. White color is associated with spin domain walls, where there is an equal number of spins in the two states.

During the course of this work, finding the optimal detuning δ^* for initializing spin profiles became a challenging problem. Details of the problem and the solution that we developed are presented in the next Chapter.

Chapter 5

Correcting the intensity profile of the Stark laser

Chapter 4 explained how we use the off-resonant light of a laser (referred to as the Stark laser) to detune a π-pulse from the $|1\rangle \rightarrow |2\rangle$ transition for chosen regions of the cloud when initializing a spin profile with patterned light. It was pointed out that numerical simulations show that the optimal value of this optically-induced two-photon detuning is $\delta^* = \sqrt{3}\Omega_R$.

We use an acousto-optic modulator (AOM) device to control the intensity of the Stark laser beam. The power of the rf signal going into the AOM modulates the intensity. The rf power itself is adjusted by a control voltage, which will be referred to as the AOM control voltage (V_{AOM}). The input rf frequency of the AOM is fixed. Since V_{AOM} sets the optical detuning, and there is an optimal detuning, there is therefore an optimal V_{AOM} (V_{AOM}^*).

To find V_{AOM}^*, one could scan the Stark laser intensity by changing V_{AOM} and applying a π-pulse at every new voltage. The intensity of the off-resonant laser light changes the total number of atoms that appears in the image after applying the π-pulse. The total population of state $|1\rangle$ atoms (N_1) can be plotted against V_{AOM}. The first local maximum in the population corresponds to δ^*, because when $\delta = \delta^*$, the maximum number of atoms returns to state $|1\rangle$ after rotating around $\vec{\Omega}_R'$ once (see Fig. 4.7(b)). The corresponding voltage is V_{AOM}^*. Figure 5.1 shows an example of finding this optimal voltage. In practice, however, some challenges were faced in accomplishing this task. This Chapter discusses these problems and details the method used to solve them.

5.1 The problem with the Stark laser intensity

The output of the optical fiber has a Gaussian profile. This beam expands quickly and is passed through a collimating lens before reaching the DMD; therefore, it is expected that all the atoms experience an almost equal optical detuning. However, that is not the case, as the intensity of the Stark beam experienced by the atoms has spatial variations. Figure 5.1 shows the atom population only at the center of the cloud. When the intensity is not spatially uniform, other parts of the cloud would reach the optimal detuning at different V_{AOM} values.
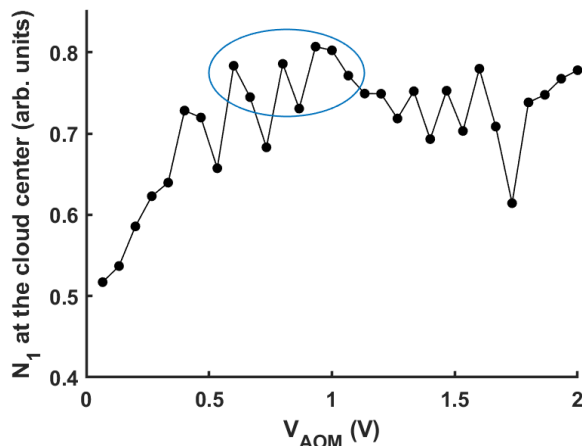
Figure 5.1: Population of atoms in state $|1\rangle$ (N_1) at the center of the cloud as a function of V_{AOM} that sets the intensity of the Stark laser. V_{AOM}^* correspond to the first maximum of the plot, which is located somewhere in the circled region. To obtain the plot, V_{AOM} is scanned, and at each voltage, a π-pulse is applied. The π-pulse would be resonant in the absence of the laser light. In each case, all the atoms are initially in state $|1\rangle$.

The variations in intensity could be due to different factors. One reason could be refractions at the bottom surface of the science cell. Even small misalignment of the optics between the DMD and the science cell could be another reason. A further reason could be interference of the beam with itself, after reflecting from the top of the science cell. There could also be reflections from outside the science cell. In any case, these and other possible factors could introduce spatial variations in the detunings experienced by different parts of the ensemble.

Figure 5.2 shows an example of measured detuning when the DMD image is uniform. A uniform image means all the pixels have the same value, e.g. all pixels are white or have the same shade of gray. To measure detuning across the cloud, we use the Ramsey method that was explained in Section 4.2.2 for measuring U_{diff}, with the difference being that in Fig. 4.3, the Stark laser is on during the evolution time. Since the DMD pattern is uniform, illuminating the atoms with the Stark laser will show if the laser intensity experienced by the atoms is non-uniform.

In principle, one could improve the Stark laser optics to decrease the spatial variations in the intensity experienced by the atoms in the science cell. However, this is not an easy task. Each time one of the knobs on the optics is tweaked, the best way to check the effect of the changes made is to measure the detuning. Since the method of measurement is a Ramsey scan, that would take about 40 minutes after each tweak. Tens of these tweaks could be needed to finally obtain uniform intensity. To overcome this difficulty, we developed another method that is explained in the rest of this Chapter.
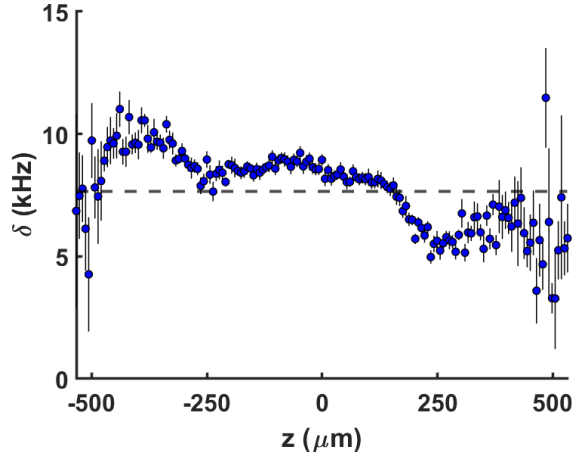
Figure 5.2: Detuning δ across the cloud introduced by the off-resonant Stark laser. To obtain the data, a uniform image is uploaded to the DMD and the Stark laser is turned on during the interrogation time of the Ramsey measurement. Each data point is the frequency of Ramsey oscillations at the corresponding axial position with error bars extracted from fit uncertainties. The dashed line is the optimal detuning $\delta^* = \sqrt{3}\Omega_R$ for initializing a spin pattern. In our system, $\Omega_R \simeq 4.4\,\mathrm{kHz}$. The variations in the detuning across the cloud shows that the beam intensity illuminating the atoms is not uniform.

5.2 Solution idea

The problem of non-uniform beam intensity experienced by the atoms can be solved by using a counteracting non-uniform DMD pattern. There are two ways to change the beam intensity experienced by the atoms. One way is to change V_{AOM}; another method is to change pixel values (PVs) of the DMD pattern.

Since each pixel value of a DMD pattern can be an N-bit number, the PVs can cover the range of values from 0 to $2^N - 1$. We have set $N = 8$ so the range of PVs is from 0 to 255. By keeping V_{AOM} constant and changing the PVs, we can adjust the detuning that atoms across the cloud experience. In this method, instead of scanning V_{AOM}, the PVs are scanned while V_{AOM} is kept constant. Figure 5.3(a) shows how the detuning changes as the PVs go from minimum to maximum. Note that the DMD pattern is still uniform; what is changing is the value of the pixels of the DMD pattern in each scan. Figure 5.3(b) shows how the detuning changes at a few specific axial bins as a function of pixel values, illustrating the fact that the detunings at different positions follow a similar trend, but they reach the optimal detuning at different pixel values.

The idea is to find the PV corresponding to δ^* for each bin, and make a DMD pattern based on those optimal PVs. Since these PVs will not be the same, the resulting DMD pattern will be non-uniform. Figure 5.3(b) shows estimations of the optimal PVs at the indicated positions. Although it is possible to do a detailed scan of the resulting detunings at many PVs and estimate what the optimal PV for each bin should be, it is better to do the process in two iterations with a reasonably small number of scans. The reason for that and details of the process are described in the following Sections.

To make a "correcting pattern," that is, a non-uniform DMD pattern that makes the

detunings uniform and equal to δ^* across the cloud, we must first map the positions of the DMD bins onto the imaging camera bins. This process is explained first and then the procedures for the two iterations of generating correcting patterns are described.
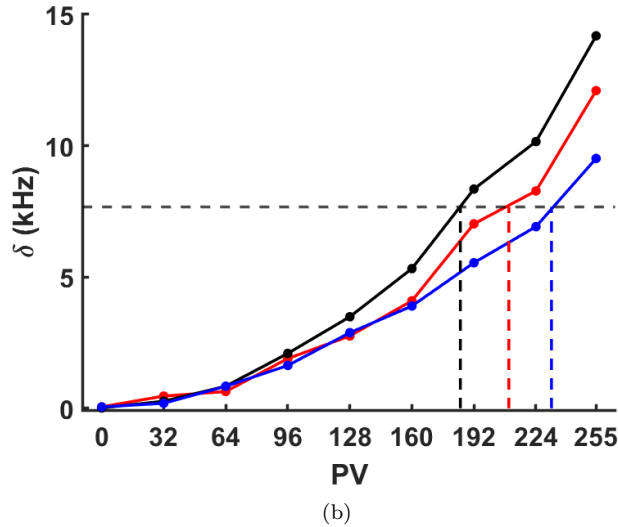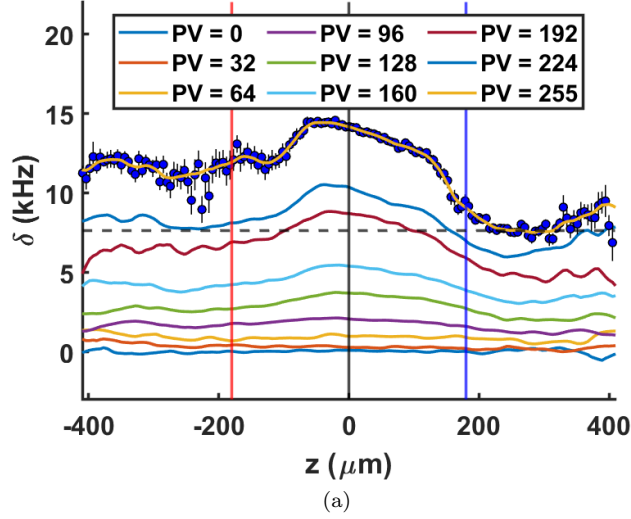

(a)

(b)

Figure 5.3: Detuning (δ) as a function of PV of uniform DMD images. In both plots, the horizontal dashed lines indicate δ^*. (a) Ramsey measurements of δ across the cloud for various DMD images. The variable is the PV of each image, which is shown in the legend. As the PV increases, the intensity of the laser reaching the atoms increases, and therefore the detuning gets larger. As a typical case, the data for PV = 255 is shown on the plot and a smoothed line is drawn through the points to guide the eye. Smooth lines for other PVs have been obtained in the same manner. (b) Detuning as a function of PV at three specific axial positions, corresponding to the same color vertical lines in (a). As (b) shows, the detuning has similar trends across the cloud, but different axial bins reach the optimal detuning at different PVs. The dashed vertical lines in (b) show the approximate PV at the corresponding axial position that makes the detuning at that position roughly equal to the optimal detuning.

5.3 Mapping imaging camera and DMD bins

Since the trapped ensemble is quasi-one-dimensional, it makes sense to speak of bins rather than pixels; nonetheless, the two terms will be used interchangeably in this context. A mapping between the bins of the DMD and the camera are needed because a shift by one bin on the DMD is not one bin shift on the camera, due to the difference in the size of their pixels. Moreover, the center of the DMD does not necessarily match the center of the camera, though tweaking the optics could bring them closer by directing the beam towards the center of the cloud, and hence the center of the camera.

The procedure of mapping the camera and DMD bins is as follows. A "small" pattern is uploaded onto the DMD, where small is relative to the size of the cloud. V_{AOM} is set to some large value to make the laser intensity high. This large intensity across the cloud makes the detuning large at every bin; therefore, the direction of the effective Rabi vector at every position gets close to state $|1\rangle$ on the Bloch sphere (see Fig. 5.4). The fact that the resulting detunings across the ensemble is not uniform is not an issue here. That only means the effective Rabi vectors at different axial positions are not the same, but since the detuning is very large, the effective Rabi vector at each bin is still close to state $|1\rangle$. The position of the DMD pattern is then shifted from the DMD center in multiple steps, and each time a π-pulse is applied. After each pulse, an image is taken. For each image, a Gaussian function is fitted and the center is extracted. Plotting Gaussian centers against DMD pattern shifts tells us how DMD and camera bins map onto each other. A linear function is fit to this data to extract the slope and intercept, as shown in Fig. 5.5. These two parameters of the mapping equation are then used to generate a correcting pattern based on approximated optimal pixel values for each bin of the imaging camera. To get a more accurate mapping equation, the shifts of the DMD pattern should cover a large range of the DMD bins.
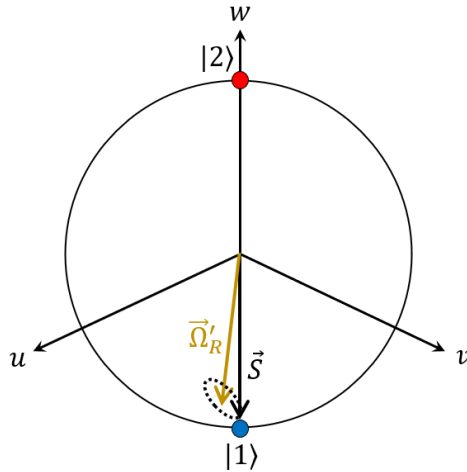

Figure 5.4: Large detuning makes the effective Rabi vector point very close to the south pole of the Bloch sphere. In this case, when a π-pulse is applied, atoms precess and remain in a state that is very close to their original state of $|1\rangle$. The dashed circle indicates the precession path that the spin state vector $\vec{S}$ takes while the pulse is being applied.
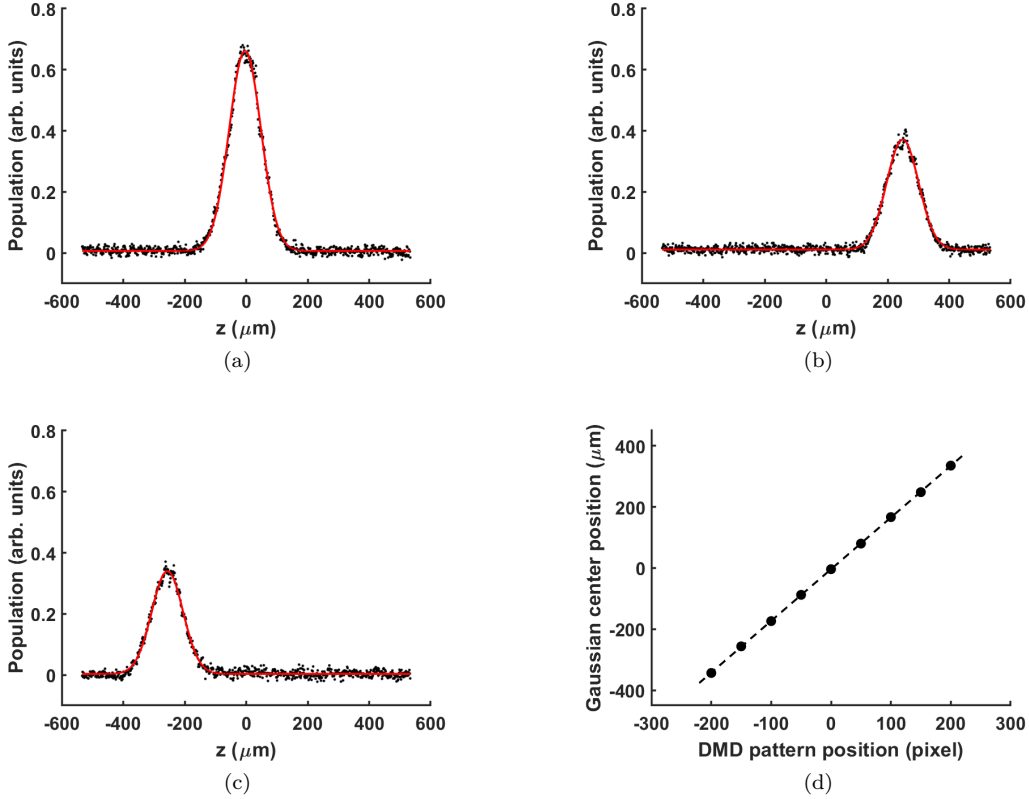
Figure 5.5: To map the pixels of the DMD and the imaging camera, a small DMD pattern is shifted across the DMD with a large detuning, and a π-pulse is applied after every shift. (a), (b), and (c) show examples of where the shifted DMD patterns appear on the camera. Solid red lines are Gaussian fits. (d) shows the center of the fitted Gaussian as a function of the shift in the DMD pattern. The dashed line in (d) is a linear fit. The slope and intercept of this line relate positions of the DMD bins to the camera bins. In this example, the slope is $1.7\,\mu\mathrm{m}/(\mathrm{DMD\,pixel})$ and the intercept is $-3.8\,\mu\mathrm{m}$. The magnification of the camera is $1.349\,\mu\mathrm{m}/(\mathrm{CCD\,pixel})$.

5.4   First iteration for making a correcting pattern

A condition for the "PV scanning" method to work is to have a large enough intensity such that, at maximum pixel value, detunings of all the bins can reach the optimal detuning δ^*. The DMD pattern to check this requirement is a cloud-wide white image, i.e. all the pixel values are set to the maximum value of 255. An example of meeting this requirement is shown in Fig. 5.6. The fact that the atoms at different positions have different detunings due to non-uniformity of the beam intensity is not an issue here. What we want to be sure of is that at some pixel value, whether maximum value or below that, it is possible to get to the optimal detuning. If V_{AOM} is not large enough, and thus the optical intensity is lower than needed, there will be some bins for which it would not be possible to reach the optimal detuning at any pixel value. If that problem happens, all we need to do is increase V_{AOM} until detunings get large enough.

It should be noted that setting a large V_{AOM} to make the intensity high would not be a
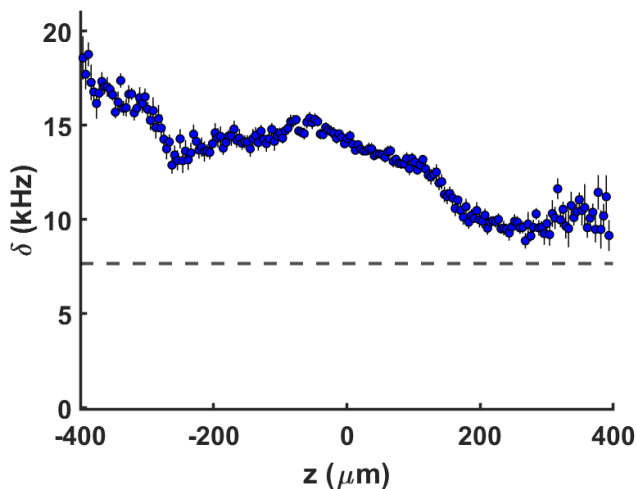
Figure 5.6: Detuning across the cloud in a case where beam intensity of the Stark laser is large enough everywhere so that detuning at all positions is above the optimal detuning, indicated by the dashed line.

good idea, although it would make it possible for the detunings at all the axial bins to reach the optimal detuning at some pixel value. Making V_{AOM} large would decrease the intensity resolution achievable by changing the DMD pixel values. If the voltage is smaller, changing pixel value by one unit would cause a smaller change in the intensity, and thus the detuning. A good V_{AOM} value is one that is large enough so that all the bins can reach the optimal detuning, but not so large that all detunings are far above δ^*.

As Fig. 5.3(b) shows, the detuning for each axial bin is a monotonic function of the pixel value. Instead of measuring detuning for many pixel values and then fitting a function such as a second or third order polynomial, we can approximate the behavior of the detuning by doing Ramsey measurements for only three pixel values and linearly interpolate between those points.

For this method to work, there is still another requirement. The smallest pixel value among these three points should be small enough so that the detuning of all the bins are below the optimal detuning. This condition, plus the previous condition of surpassing δ^*, ensures that by interpolating between the three points, at some pixel value, the detuning will equal δ^*. There is no particular requisite of the pixel value of the middle point but it is preferable to set it to the midpoint between the pixel values of the first and third points to decrease the inaccuracy of the extracted optimal pixel value found from a linear interpolation of the three points. Figure 5.7(a) shows an example of measuring detunings across the cloud with three uniform DMD patterns, the PV for one of which is small enough that detunings of all the bins remain below δ^*, and for one it is large enough that the detunings are above δ^*.

Based on the estimated optimal PVs, an intensity correcting pattern can be generated by a MATLAB code. The purpose of this correcting pattern is to make the detuning of all the bins equal to the optimal detuning. The input data to the code is the set of three pixel values and their resulting bin detunings as discussed above. For each bin, the code interpolates

the detunings to find the pixel value for which the interpolated detuning has the smallest distance to the optimal detuning δ^*. Figure 5.7(b) shows an example of first iteration results for estimated optimal PVs across the cloud, which are based on the measurements shown in Fig. 5.7(a).

The estimated pixel values are then used to generate a correcting pattern. Figure 5.7(c) is the Ramsey measurement of detunings that checks the quality of the correcting pattern, which should be contrasted with the detunings in Fig. 5.7(a) that were obtained with uniform DMD patterns. The improvement in making the detunings more uniform and bringing them closer to δ^* is already noticeable.

Depending on which three points are originally chosen for interpolation, the quality of the correcting pattern can change. If the points are far apart - for instance, if the pixel values are 0, 128, and 255 - the quality of the correcting pattern will be lower. In any case, this step serves as a first iteration. A second iteration with a slightly different method can be done to improve the quality of the correcting pattern.

5.5 Second iteration for making a correcting pattern

The approximate optimal pixel values found from the first round can be used as the starting point for a second round. This time, there will again be three measurements to do a new and more accurate estimation of the optimal pixel values. The difference is that in each measurement, the pattern is not made of a single pixel value for all the bins as was done in Fig. 5.7(a). In this round, there are three non-uniform patterns. One is based on the results of the first round, which is the "middle" pattern. The pixel values of this middle pattern are raised and lowered to make "higher" and "lower" PV patterns. The magnitude of PV shift should be smaller than the first round as this round is essentially a fine-tuning step. Ramsey measurements of the detuning are done to obtain the detuning changes at each bin for the higher and lower patterns. No measurement is needed for the middle pattern as it has already been done at the end of the first round of measurements to check the quality of the correcting pattern of the first iteration.

The remaining procedures of this iteration are then the same as the first iteration. Once the Ramsey measurements of the lower and higher patterns are completed, the data is interpolated again. Since the distance between the PVs is smaller this time, the approximation is more accurate. Finally a new correcting pattern is generated based on the new approximation of the optimal pixel value at each bin.

Figure 5.8 shows an example of the steps taken in the second iteration. Figure 5.8(c) illustrates the final result in this round showing the improvements in bringing the detuning across the cloud much closer to the optimal value.

The advantage of finding the correcting pattern in two iterations, a coarse method followed by fine tuning, is that over time there can be drifts in the system that would lower the quality of the correcting pattern. However, when the changes are small, we would not need the first iteration each time. We could just start from the last correcting pattern that was made and use that as the middle pattern, so we would need the second iteration with three points only. This is a quicker method than having one iteration in which we would
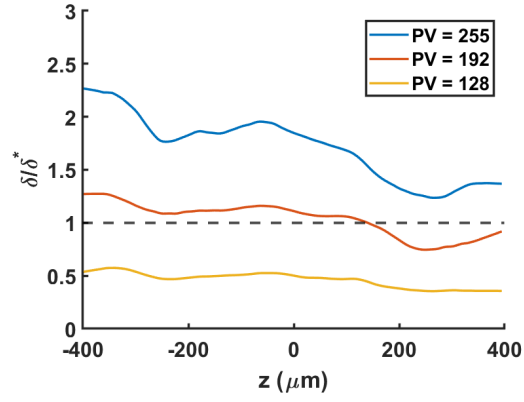
(a)
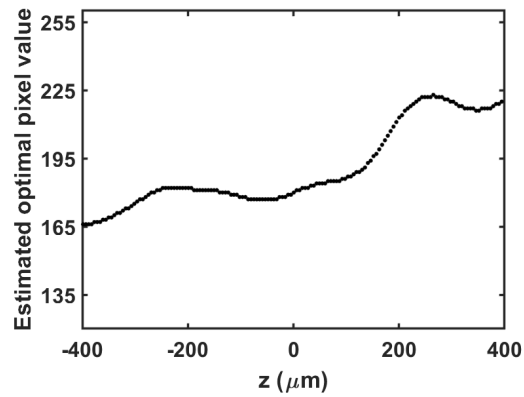
(b)
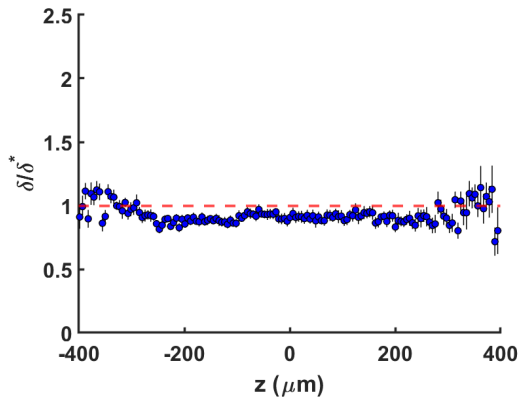
(c)

Figure 5.7: Results of the first iteration for correcting the non-uniformity of the Stark laser intensity reaching the atoms. (a) Three detuning measurements with uniform DMD patterns with pixel values equal to 128, 192, and 255. (b) Estimated optimal pixel values for making the detunings across the cloud uniform and closer to δ^*. These PVs are found by interpolating the measurements shown in (a) for each bin, and estimating at what PV, δ would be closer to δ^*. (c) Result of detuning measurement using the DMD pattern generated based on the pixel values in (b).

scan many pixel values each time.

After a good quality correcting pattern is obtained, it can be multiplied by other patterns for making spin profile initializations used in this thesis. The correcting pattern is independent of any spin profile. The same pattern could be used to make, e.g., a two-domain or a three-domain spin profile.

5.6 A quicker way to check the quality of the correcting pattern

With a Ramsey measurement, the quality of a correcting pattern can be checked. However, a Ramsey measurement is a relatively long process. Since the information of the measurement is extracted based on a sinusoidal fit, it would take around 40 minutes to sample enough points for the fitting uncertainties to be small. However, our apparatus is stable enough that a frequent check of the quality of the correcting pattern using the Ramsey method is not needed. A quicker way to check the quality of the pattern is to simply check the density profile obtained when the correcting pattern is used together with a π-pulse, and to compare that to the density profile with no laser light present and no π-pulse applied. If the correcting pattern has a high quality, a cloud-wide π-pulse rotates the initial state vector $|S\rangle = |1\rangle$ around the effective Rabi vector and brings it back to its original position. Taking an image after that should produce a Gaussian density profile that is very similar to the density profile of a cloud without any state vector manipulation. On the other hand, if the quality of the correcting pattern has deteriorated over time, an image with correcting pattern and π-pulse combination will show a density profile that has either a distorted Gaussian profile or a Gaussian profile with a smaller amplitude compared to the original profile. That is because we only image atoms in state $|1\rangle$, so if there is something wrong with the correcting pattern, a π-pulse will not bring all atoms back to their original state and the resulting image will look different. For the sake of averaging, a few points should be taken, which makes the entire process take about 10 minutes.

This Chapter covered the problems about non-uniform optical detunings across the cloud caused by variations in the Stark laser intensity reaching the atoms, and the method that we developed to solve this issue. The next Chapter presents the method that we developed to extract information about the evolution of the spin system that would otherwise be hard to obtain using standard fitting methods.
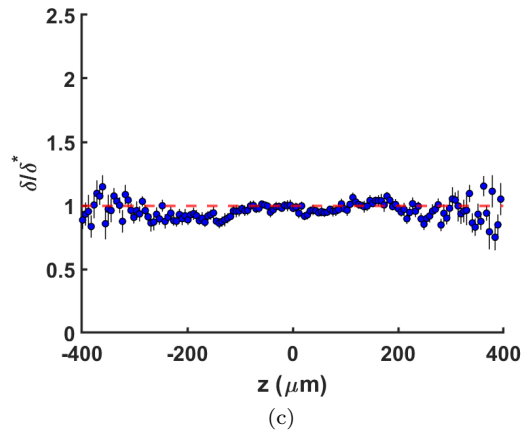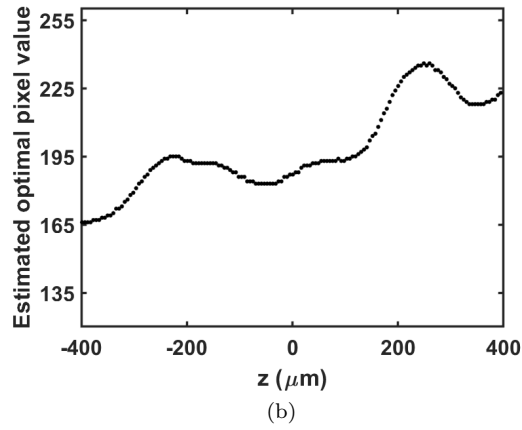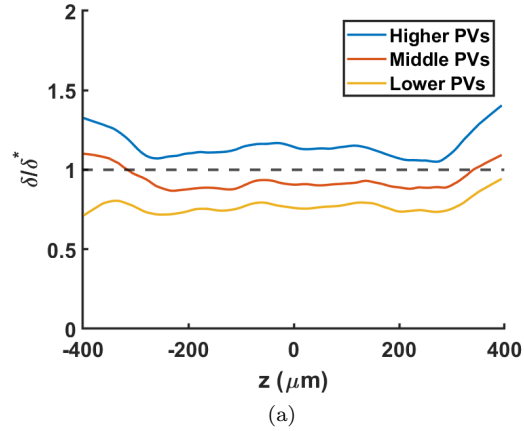
(a)

(b)

(c)

Figure 5.8: Results of the second iteration in correcting the non-uniformity of the detuning. (a) Three detuning measurements with non-uniform DMD patterns with pixel values obtained by raising and lowering the pixel values in the "middle" pattern. The middle pixel values are obtained in the first iteration. In this example, the middle PVs are changed by ± 20 units for the higher and lower PVs. (b) Estimated optimal pixel values for making the detunings across the cloud δ^*, found by interpolating the measurements shown in (a). (c) Result of detuning measurement where the DMD pattern has been generated based on the pixel values in (b). For convenience, plot scales have been kept the same as those in Fig 5.7.

Chapter 6

An algorithm for extracting spin domain wall information

To extract parameters about the evolution of the longitudinal spin component, the usual way is to fit a function and look at the evolution of the fit parameters. For a spin profile initialized with three spin domains, the phenomenological fitting function that we use is

$$S_{||}(z,t) = A \tanh\left(\frac{z - z_L}{\lambda_L}\right) \tanh\left(\frac{z - z_R}{\lambda_R}\right) \exp\left(\frac{-(z - z_G)^2}{2\sigma_G^2}\right), \qquad (6.1)$$

where z_G and σ_G are the Gaussian center and width obtained from a fit to the density profile. The fit parameters are A, z_L, z_R, λ_L and λ_R, and they are all functions of time. This Chapter discusses problems that arise when using a fitting method over the course of the dynamics of the system. Next, it presents the method that we employ to avoid fitting a function like Eqn. 6.1.

6.1 The problem with the fitting method

In early stages of the evolution of the spin system, Eqn. 6.1 is a suitable fitting function for the profile of the longitudinal spin. However, relatively quickly, the profile evolves into a form where the functional form of Eqn. 6.1 is no longer applicable as a good fitting function. Figure 6.1 shows an example where this model is suitable near the beginning point of the dynamics (Fig. 6.1(b)) but becomes unsuitable at a later time (Fig. 6.1(c)).

In principle, this problem could still be fixed using the fitting method. In Fig. 6.1, for instance, at times later than around 60 ms, the profile transitions from three to five spin domains. A function similar to Eqn. 6.1 but with four hyperbolic tangents could be used to fit the data. However, in general this is not a good idea. In different data sets, transition in the number of domains occurs at different times so we would have to check every set individually and then determine where to change the fitting function. Another issue is that the number of domains changes back from five to three at some later time, as it happens around 120 ms in Fig. 6.1(a), and this second transition also happens at different times in
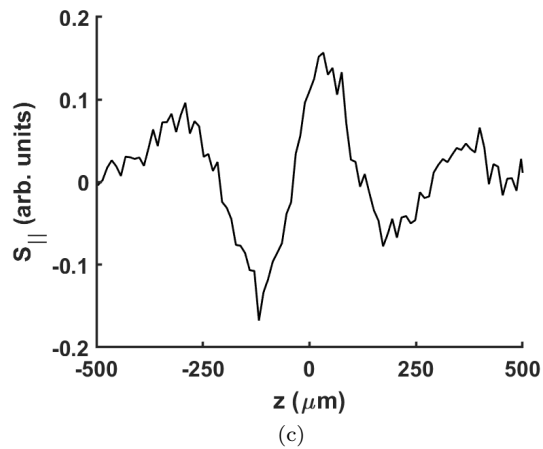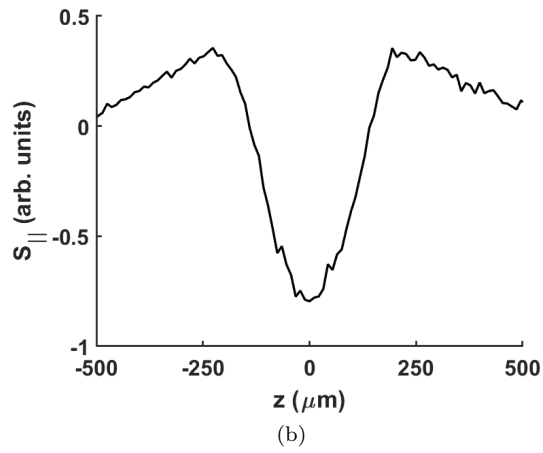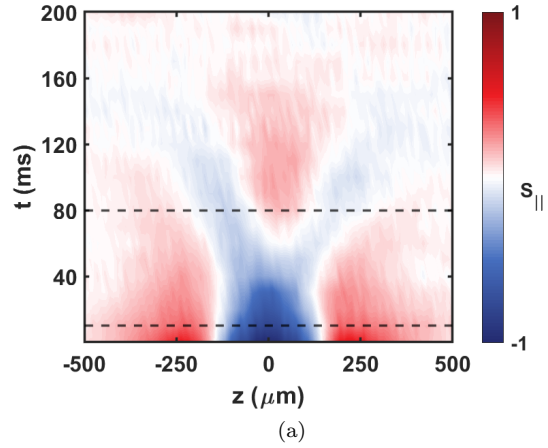
Figure 6.1: An example showing problems with fitting method for extracting information about longitudinal spin dynamics. (a) Spatio-temporal evolution of longitudinal spin where the spin profile at the times indicated by the dashed lines are shown in the next two panels. (b) and (c) are longitudinal spin at times $t = 10\,\mathrm{ms}$ and $t = 80\,\mathrm{ms}$, respectively. As can be seen, Eqn. 6.1 cannot be a suitable fit in (c).

different data sets. Moreover, there could be cases where the profile of the spin could obtain a complicated functional form that could be quite different from a function made of some elementary functions such as Eqn. 6.1.

6.2   Solution idea

In the evolution of the longitudinal spin, the widths and centers of the spin domain walls are what we typically look for. Analysis that comes later is based on the values of these quantities. The center of a domain wall is where there is an equal superposition of the two spin states, which makes $S_{||}(z,t) = 0$ - essentially a zero-crossing in a plot like Fig. 6.1(b) or Fig. 6.1(c). In Eqn. 6.1, the λ's are the widths of the left and right walls.

To locate a wall center, we could just find the zero-crossings of the longitudinal spin profile at each sampling time, but the drawback would be the lack of any information about the size of the wall. To maintain some information about the wall size, we can define a small threshold around the zero line. The part of the spin profile that lies within this threshold region would define the "wall region." Figure 6.2 shows an example of using a threshold for $S_{||}(z,t)$ to define wall regions with certain wall centers and region sizes.
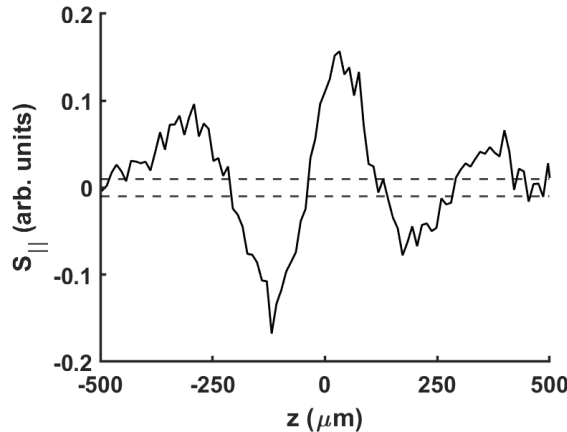

Figure 6.2: Example of using a threshold to extract information from $S_{||}$. The horizontal dashed lines at ± 0.01 set the threshold and the parts of the signal that fall within these two lines are defined as "wall regions."

Since the threshold value is arbitrary, the size of the wall region is not a good approximation for the width of a wall. Furthermore, for the same threshold and wall width (constant λ in Eqn. 6.1), the wall region grows as the wall center moves toward the cloud edge. This increase in wall region size is due to the decrease in the signal size on the sides of the cloud. Nonetheless, the wall region can still be used as an approximation of the uncertainty in the wall center position, although in most cases it would be an overestimation. In general, the wall region size can be used as an estimation of the wall width if the Gaussian distribution is incorporated in the analysis. However, this idea is not followed in this work, and the size of the wall region is only used as an estimation in the uncertainty of the wall position.

The rest of this Chapter discusses the more important features of this "threshold" method

and how domain wall information is extracted using this method. A comparison between the results of the threshold and fitting methods, in which Eqn. 6.1 would be applicable, is shown at the end.

6.3   Details of the threshold algorithm

Before information about domain walls can be extracted with the threshold method, some pre-processing steps are needed. This Section first explains these steps. Then, extraction of domain-wall information is explained. Finally, wall center and wall region width are calculated.

6.3.1   Smoothing longitudinal spin profile

In the process of extracting information about domain walls, the first step is to smooth the spin data, which is done by a moving-average method. The smoothing span should be some value that the smoothed data still keeps the overall profile of the original data so that its salient features are not shifted by much. Figure 6.3(a) shows an example of the original data (cyan line) overlapped by smoothed data (black line) with threshold shown as two horizontal lines. The circled region in Fig. 6.3(a) is shown in Fig. 6.3(b) to better illustrate why smoothing is helpful. The fact that the signal jumps in and out of the threshold region is due to the noise in the images, and smoothing removes this issue, making the data smoothly pass through the threshold region.
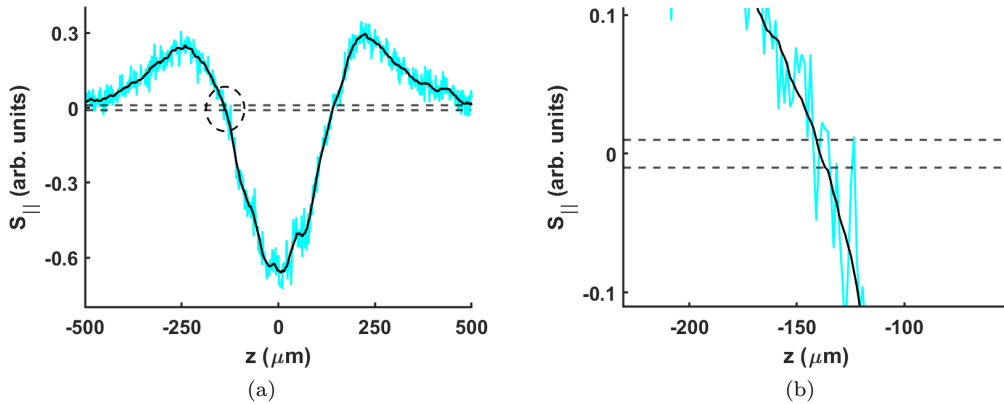

Figure 6.3: Example of smoothing the longitudinal spin data using a moving-average method. (a) Overlap of original data (cyan) by smoothed data (black). Horizontal dashed lines set the threshold region for processing steps that come next. The circled region in (a) is plotted in (b), showing that smoothing removes the noise in imaging, which makes the data jump in and out of the threshold region. The smoothing span has been set to 20 points.

6.3.2 Binarization of the longitudinal spin data matrix

Longitudinal spin evolution data is stored in a matrix where one dimension is the axial bin, or equivalently axial position (z), the other axis is the sampling time (t), and the elements of the matrix are $S_{||}(z,t)$. At each sampling time, $S_{||}(z,t)$ is first smoothed across the position axis of the matrix. Then, the data matrix can be binarized based on a threshold. Figure 6.4 shows an example of this binarization step in which every element within the threshold is changed to logical 1 (marked by vertical stripes on the figure) and the rest are set to logical 0. Both the smoothing span and the threshold are chosen constants. Binarization is done only because it facilitates the future coding steps in the analysis, primarily because of the built-in functions of MATLAB for handling binary matrices.
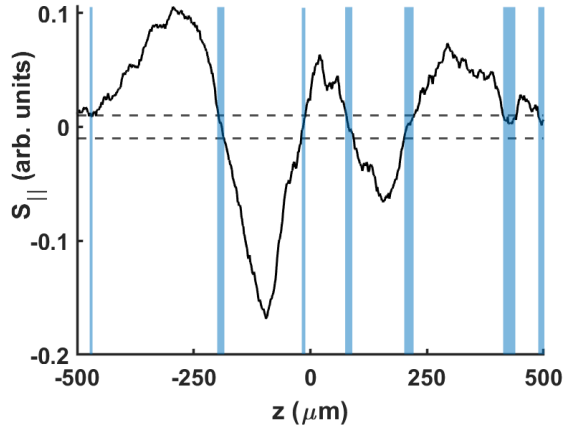

Figure 6.4: Illustration of how binarization of $S_{||}$ at a specific time is performed. Blue stripes are drawn for elements that fall within the threshold (shown as horizontal dashed lines). These parts will be set to logical 1. The other parts will be set to logical 0.

Binarization of the entire spin data matrix is done in the same way as in Fig. 6.4, which is at one specific time. The same threshold is used for the entire matrix. Figure 6.5 shows an example of such binarization where black stripes represent logical 1 and white regions show logical 0. The dynamics of domain walls is already clear; nonetheless, before extracting quantities based on the binarized matrix at this step, it is helpful to first interpolate the data along the time axis and then binarize the interpolated matrix. Main points about interpolation are discussed in the next Section.

6.3.3 Interpolating the data along the time axis

After the data matrix is smoothed, instead of directly binarizing the data matrix, we linearly interpolate its elements along the time axis. No interpolation is done along the position axis of the matrix. One reason for temporal interpolation of the data is to facilitate the coding for the analysis. Some MATLAB functions easily manipulate elements of a binary matrix when those elements form a connected region. Due to the continuity of the dynamics of the system, the domain wall position moves continuously too. That means interpolating the data along the time axis can make the coding easier for the purpose of extracting information about its features. Figure 6.6 illustrates an example of how interpolation can connect regions
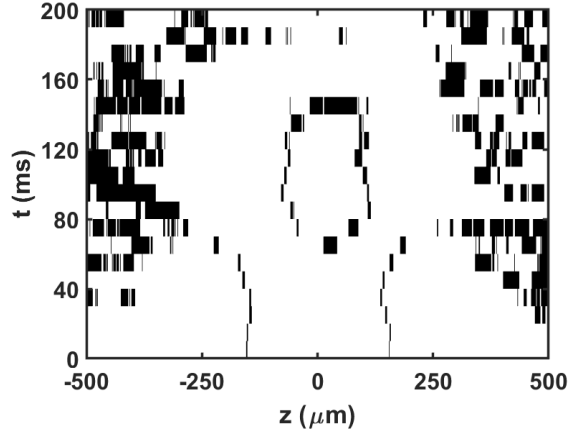
Figure 6.5: Example of binarization of an entire longitudinal spin data matrix. Black stripes represent logical 1 and white regions show logical 0.

of features. It should be emphasized that the original features of the data matrix are not changed as it is only an interpolation.
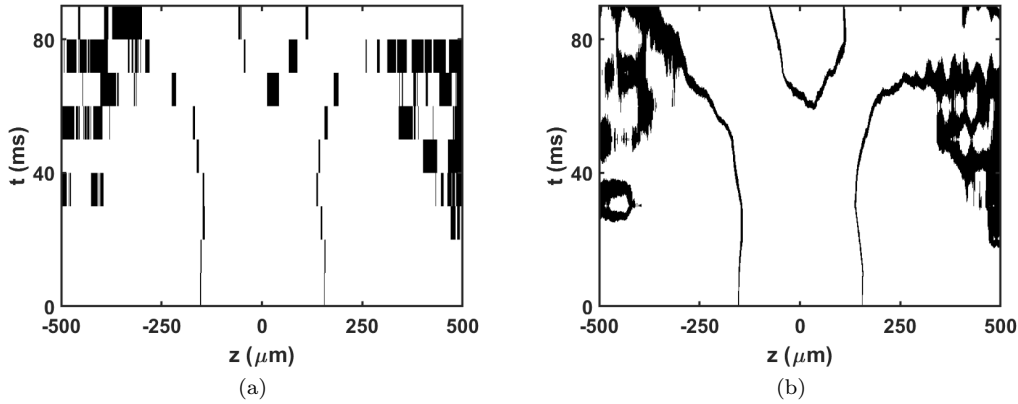

(a)

(b)

Figure 6.6: Example of temporal interpolation of the longitudinal spin followed by binarization of the data matrix. Each domain wall becomes a connected region.

One should note that temporal interpolation reveals new features masked by the resolution of the original spin data matrix. This can happen when $S_{||}$ at a certain axial position changes its sign between two consecutive sampling times. Figure 6.7 shows an example of how this could occur. In Fig. 6.7(a), features of the original data are shown and the dashed rectangle surrounds a region in which no feature has been detected. In Fig. 6.7(b), the corresponding interpolated data is shown and features have emerged in the same rectangular region. Figure 6.7(c) explains how interpolation can reveal features between measured data points. The plots of $S_{||}$ in Fig. 6.7(c) are at two consecutive sampling times, the solid line is at $t = 110$ ms and the dotted line is at $t = 120$ ms. As can be seen, neither of the lines fall within the threshold near the center of the cloud. Interpolation makes $S_{||}$ pass through the threshold region, and that makes it to be detected in the rectangle in Fig. 6.7(b).

50
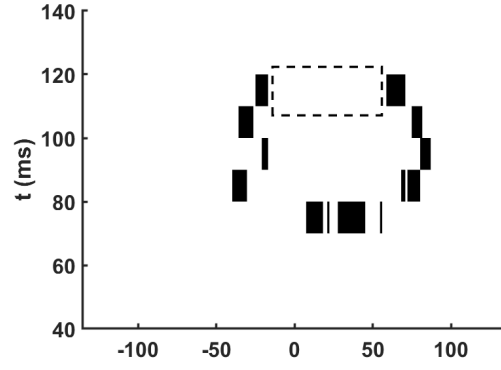
(a)
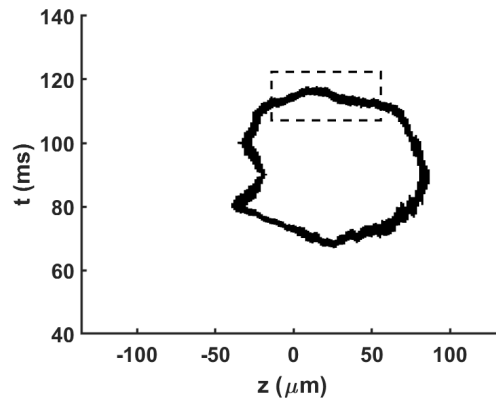
(b)
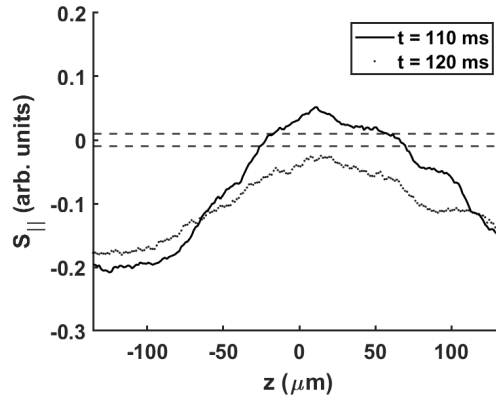
(c)

Figure 6.7: Illustrating how temporal interpolation of spin data matrix can reveal more features in $S_{||}$. (a) Detected domain wall in the original data with no features within the region surrounded by the dashed rectangle. (b) Detected features of the interpolated data, now showing features in the same rectangular region. (c) $S_{||}(z,t)$ at the two consecutive sampling times of $110\,\mathrm{ms}$ and $120\,\mathrm{ms}$, showing that interpolation would make the function pass through the threshold region (horizontal dashed lines) near the center of the cloud, which causes emergence of new features.

6.3.4   Extracting domain walls

Because the threshold method is based on whether $S_{||}$ falls within the threshold region, it will always capture regions that are not domain walls. That happens because of the overall Gaussian profile of the density. The signal to noise ratio (SNR) drops as we move from the center towards the edge of the cloud and so more portions fall within the threshold region. This is a downside of this method but given our understanding of the system and how it is initialized, it is generally easy to determine which detected features are only due to low SNR and should therefore be ignored. The removing process simply sets 1's to 0's in those low-SNR regions.

   Most of the data of this work are about a spin system that is initialized with three domains, and so there are two domain walls in the beginning. Due to dynamics of the system, the positions of these two walls shift and move towards edges of the cloud where the SNR is low. It becomes difficult to tell what is happening at those points, so we ignore the data in those regions. There is no exact axial position that denotes low SNR regions. We cut the detected features where the SNR is still reasonably high.

   Figure 6.8 shows an example of the process of removing unwanted parts. In Fig. 6.8(a), the dashed lines set the boundary for removing features. All the matrix elements in the left and right regions indicated by the dashed lines are set to 0. Figure 6.8(b) shows the same data after these unwanted features have been removed.

   After removing parts based on chosen boundaries, there can still be some small regions that are also wrongly detected as domain wall regions. These small parts are automatically removed by defining an area threshold. If the area of the connected region is smaller than this area threshold, it will be removed. Figure 6.8(c) shows an example where small unwanted regions (the small black spots) in Fig. 6.8(b) have been removed. This step works because the domain walls are continuous features and so they generally make connected regions with a relatively large area, and therefore they will not be removed.

   After all the noise features have been removed, the features of the binarized spatio-temporal matrix of the longitudinal spin component are separated for further analysis. Figure 6.9 shows an example of separated pieces. If the system is initialized with three domains, the separated regions typically consist of a left wall, a right wall, and a central region whose boundary is determined by the dynamically created new domain walls. Depending on the initial conditions, this central region could form a roughly elliptical area, or it may not be created at all.

### 6.3.5   Calculating center and region size of the domain walls

The size of the wall region is found by calculating the difference between positions of the leftmost and rightmost connected points that fall within the threshold region; then, the bin separation (dz) is added. The addition is done because the wall region size is used as an estimation of the uncertainty in the position of the wall center. For some cases, particularly in the beginning of the evolution, there is just one point that falls within the threshold region so the difference in positions of the leftmost and rightmost points is zero, resulting in a zero uncertainty in wall center. Addition of dz solves this problem.
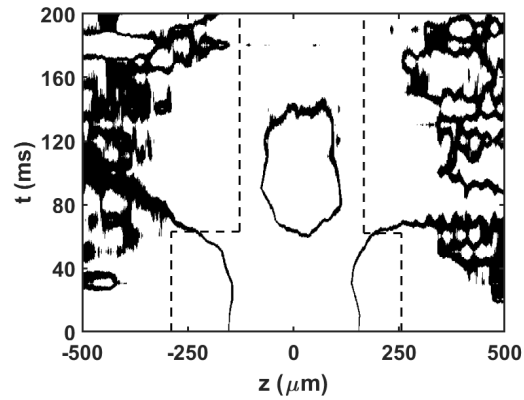
(a)
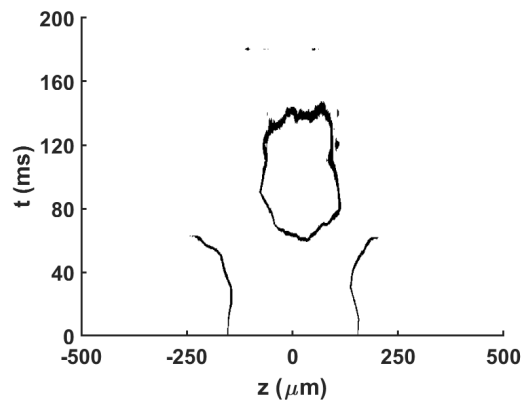
(b)
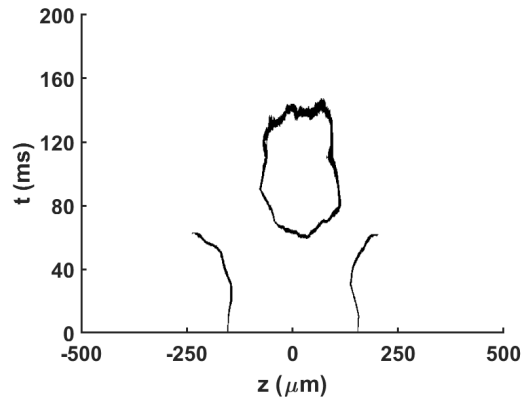
(c)

Figure 6.8: Example of removing unwanted regions. (a) shows all the detected features. The dashed lines indicate the chosen boundaries for keeping features. The detected features in the low-SNR regions of left and right parts will be removed. (b) Result of removing regions based on the set boundaries. (c) The small unwanted regions in (b) that were not removed in the previous step are removed using an area threshold. Areas of domain wall regions are relatively large due to the temporal interpolation, and therefore they are kept.
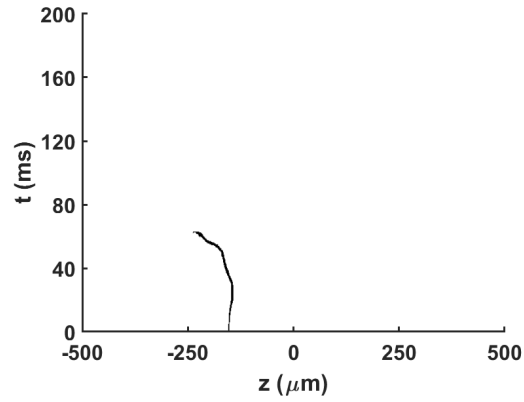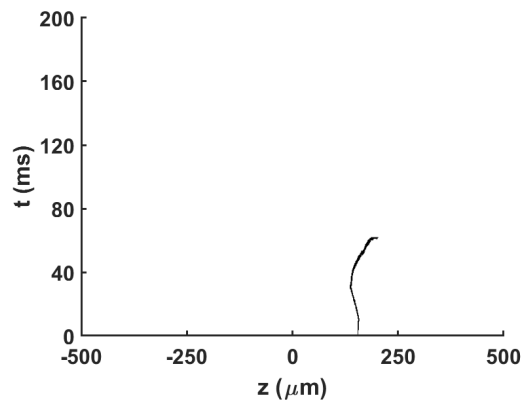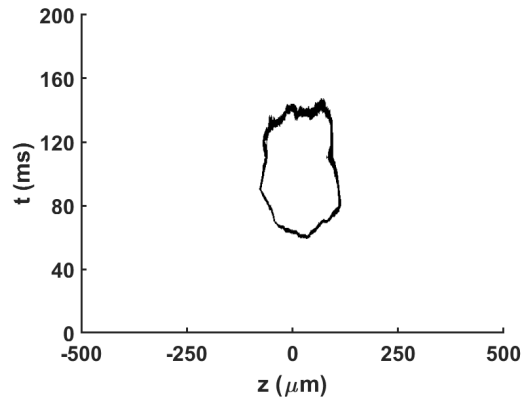
Figure 6.9: Example of separating detected regions. (a) and (b) show motion of the initially created left and right domain walls, respectively. (c) Dynamics of the central region with domain walls created dynamically.

The center of the domain wall is found by averaging positions of the leftmost and right-most connected points in the threshold region. The resulting value can be a few microns different from the zero point, which is the true center of the wall. However, this is still a good approximation for the position of the center of a domain wall given that the motion

of the wall happens on scales of tens of microns.

Figure 6.10 shows examples of extracted domain wall dynamics for the left and right sides. In these plots, the error bars represent the size of the wall region, which is in general an overestimation of the uncertainty in the center position. For points closer to the beginning, error bars are too small to be seen here.
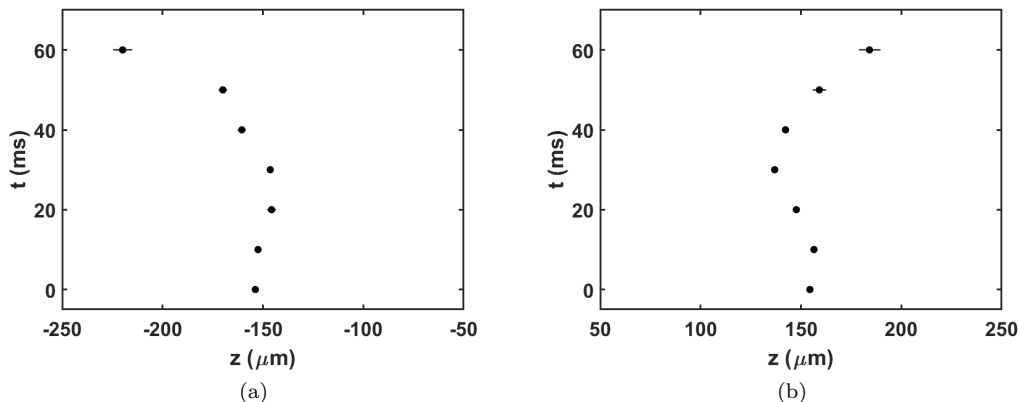

Figure 6.10: Example of extracted domain wall center position and width. Widths are indicated as error bars, which are very small for points closer to the initial time. (a) Left domain wall. (b) Right domain wall.

6.4   Comparison of the threshold and fitting methods

Figure 6.11 shows an example of the domain wall positions found using the threshold method developed in this Chapter in comparison to their positions found using the fitting method based on Eqn. 6.1. The comparison is done up to a point where the fitting still works well. As was discussed in the beginning of this Chapter, the fitting works only for a relatively short time interval before its functional form loses its quality as a good fitting function. Since the threshold method is not based on fitting, it can still be used beyond that point. As Fig. 6.11 shows, the wall positions found from the threshold method agree well with their values found from the fitting method; their difference is just a few microns.

To extract information about domain wall dynamics, we also tested image processing methods. In Fig. 6.1(a), for instance, domain walls have white color, which can be detected by region detection methods in image processing. However, the threshold method proved to be a better method here, mainly due to the level of control that we have over the spin data matrix. In image processing methods, the data would be an image matrix, and we would need to work based on pixel values, which in general made the processing less straightforward.
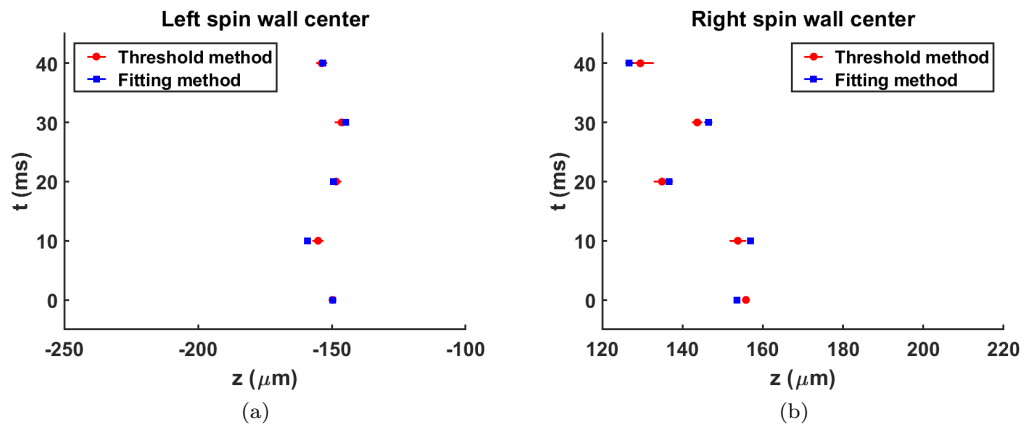
Figure 6.11: Comparison of domain wall positions found via the threshold method (circular points) and the fitting method (square points) that is based on Eqn. 6.1. Error bars of circular points indicate the width of the wall region, which is used as an approximation for the uncertainty in the position of the wall. Error bars of square points are fit uncertainties. Comparison is done up to a point where the fitting function could still work. The two methods agree to a few microns. (a) Left wall center. (b) Right wall center.

Chapter 7

Experimental data and discussion

Chapter 5 explained a method to make the optical detuning of the atoms uniform when they are illuminated by an off-resonant laser so that spin-domain initialization could be done optimally. Chapter 6 discussed an algorithm that enables us to extract spin-domain wall centers as the system evolves. This Chapter presents the experimental data and their analysis.

The main focus of this Chapter will be on the analysis of the longitudinal spin data obtained for systems that have been initialized with three spin domains. In all of the data sets, the differential potential has been adjusted to be uniform via the compensating scheme explained in Section 4.2, in which the Zeeman shift is adjusted to cancel the effect of the mean-field shift. All the data is taken at peak density $n_0 = 2 \times 10^{13}\,\mathrm{cm}^{-3}$ and temperature $T = 650\,\mathrm{nK}$.

Figure 7.1 shows an example of a spatio-temporal plot of the longitudinal spin dynamics. Based on the type of motion that the domain walls exhibit, a phenomenological model is suggested to fit the trajectory of the walls. Further analysis based on the fitted parameters is presented later. It is shown how regimes of domain wall motion can be observed depending on initial spin distribution. Examples of domain wall motion in two-domain systems are also presented, which help us understand what initial conditions can lead to displacement of a wall. Finally, it is shown that a three-domain system is capable of creating new domain walls dynamically.

7.1 Characterizing initial longitudinal spin profiles

The DMD pattern to make a three-domain spin profile is a dark-bright-dark or bright-dark-bright pattern. After applying a cloud-wide π-pulse, dark regions become state $|2\rangle$ while atoms in bright regions remain in state $|1\rangle$. The three-domain data in this Chapter has the configuration of $|2\rangle - |1\rangle - |2\rangle$, for which the DMD image has the pattern dark-bright-dark when initializing spin domains. In the following discussions, width of the central bright region (d) refers to the size of this bright region of the DMD pattern.
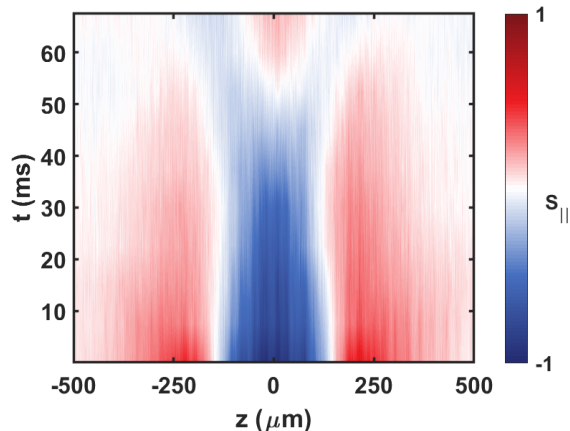
Figure 7.1: Spatio-temporal plot of longitudinal spin for a system initialized with three spin domains. The blue color is associated with state $|1\rangle$ (the south pole of the Bloch sphere) and red indicates state $|2\rangle$ (the north pole of the Bloch sphere). White curves are trajectories of domain walls.

The initial profile of the longitudinal spin $(S_{||})$ with three domains can be characterized by the phenomenological model

$$S_{||} = A \tanh\left(\frac{z - z_L}{\lambda_L}\right) \tanh\left(\frac{z - z_R}{\lambda_R}\right) \exp\left(\frac{-(z - z_G)^2}{2\sigma_G^2}\right). \quad (7.1)$$

The atom density has a Gaussian distribution with mean $z_G = 0$, and at temperature 650 nK, the Gaussian width is $\sigma_G = 187\,\mu$m. z_L and z_R are the left and right domain wall centers. λ_L and λ_R are the wall widths. The quantity that changes in the initial setup of the experiment is the middle domain size (D), defined as the difference between the right and left wall centers,

$$D \equiv z_R\,(t = 0) - z_L\,(t = 0). \quad (7.2)$$

In term of wall positions, initialization is symmetric with $|z_R| = |z_L|$. The left and right wall widths are kept constant at $\lambda_L \approx 80\,\mu$m and $\lambda_R \approx 74\,\mu$m, noting that the left wall is a few microns larger than the right one. There are at least two possible contributing factors for this difference. One is that the optical detuning is not exactly at $\delta^* = \sqrt{3}\Omega_R$ and has some fluctuations along the axial direction. Another reason is that in the setup, the microwave waveguide that is used in the two-photon pulse for creating the spin domains is on one side of the cloud, which leads to a non-uniform Rabi frequency across the cloud. This asymmetry in the initialization leads to an asymmetry in the dynamics, but the overall behavior of the left and right walls are the same, which will be illustrated later.

Figure 7.2(a) shows an example of the initial configuration of a three-domain setup, and the profile is characterized in Fig. 7.2(b) by fitting Eqn. 7.1 to $N_2\,(z, t = 0) - N_1\,(z, t = 0)$.

Equation 7.1 fits the initial spin profile well for smaller middle domain widths. As D increases, such as in Fig. 7.3(a) and Fig. 7.3(c) compared to Fig. 7.2(b), the fitting quality of the model drops. However, if we exclude points from the central region in the fitting, like Fig. 7.3(b) and Fig. 7.3(d), the fit wall width values approach those with a relatively
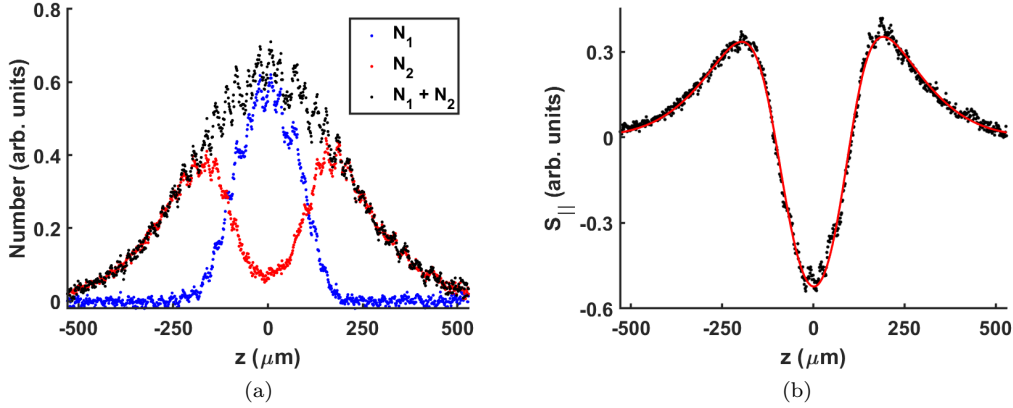
Figure 7.2: Characterization of the initial longitudinal spin profile with three domains. (a) Distribution of the two states and the overall Gaussian distribution of the atom density $(N_2 + N_1)$. In general, N_2 does not get to zero in the central region (or equivalently, N_1 does not get to its maximum possible value) in the initialization. The primary reason is probably the fact that we do not optimize the initialization in the radial direction. That additional optimization would require more optical setup. (b) Determining properties of the initial longitudinal spin by fitting Eqn. 7.1 to $N_2 - N_1$. The red line is the fit, and $D = 208 \, \mu\text{m}$.

small middle domain size in which no point is excluded in the fitting. It is expected for all the wall widths to be the same because the only change in the DMD image used to pattern the light is an increase in the width of the central bright region of the pattern. Since the edges of the bright region are kept the same, the wall sizes should also have the same values for different D. The fitting method is only used for the initial point in the dynamics. For $S_{||}(z, t > 0)$, analysis will be based on the threshold method (discussed in Chapter 6). In that method, there is no need to exclude any points to find the wall centers.

7.2 Creation of transverse spin

When we apply a π-pulse together with patterned light, transverse spin is necessarily created at the edges of the bright regions of the DMD pattern. That is because the change in light intensity is gradual. Where the intensity is at its optimally adjusted value, which is the maximum intensity of the light pattern, the spin vector remains in state $|1\rangle$ because the π-pulse becomes a 2π-pulse. Where the light intensity is zero, the spin vector makes a complete rotation to state $|2\rangle$ after the π-pulse. In these two cases, there will be no creation of transverse spin. In cases between them, transverse spin is generated with its magnitude growing from 0, reaching a maximum, and then diminishing again. The phase of the transverse spin obtains a gradient in the initialization process as the spin vector takes a helical path through spin domain walls. Figure 7.4 schematically shows the rotation of the transverse spin in a domain wall as viewed from the longitudinal axis of the Bloch sphere (w-axis in Fig. 3.2). During evolution of the dynamics, the transverse spin precesses around the w-axis at a rate proportional to the energy difference between the two states. Since we
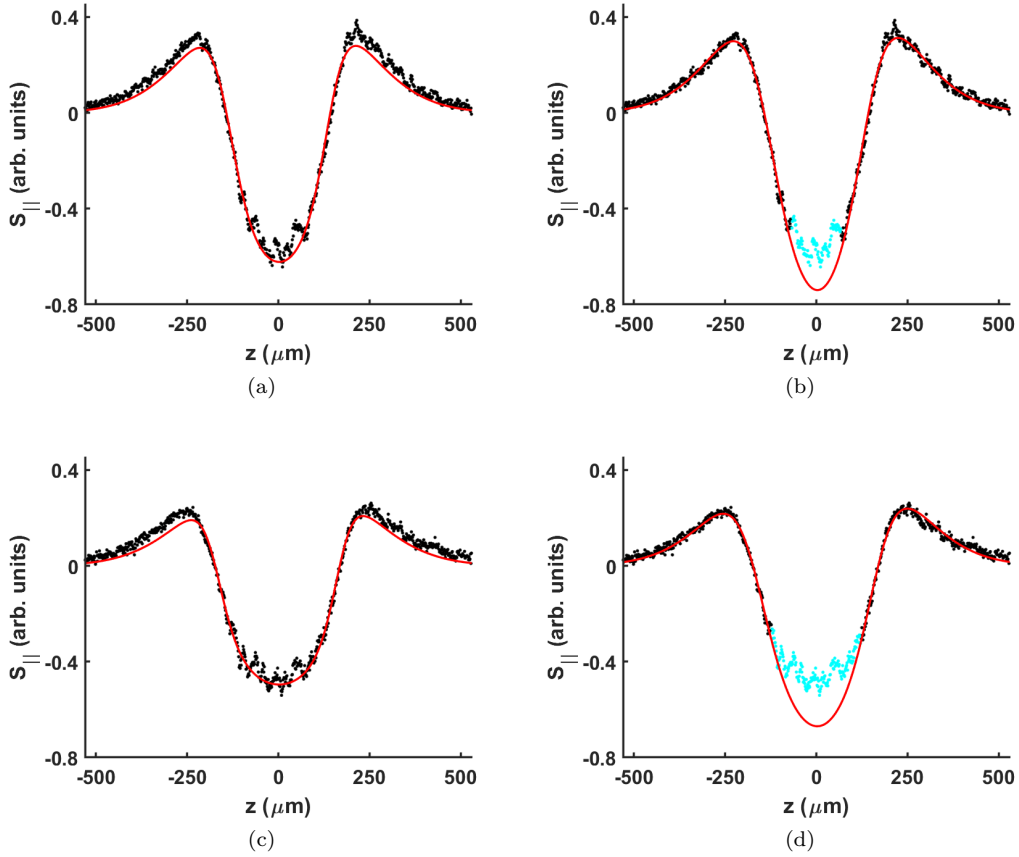
Figure 7.3: As the middle domain size increases, quality of the fitting model (Eqn. 7.1) drops as shown in (a) for $D = 285\,\mu$m and (c) for $D = 343\,\mu$m. To solve this issue, points from the center can be removed so that the fit goes through the domain wall. In (b), 100 data points have been excluded in the fit, and in (d), 180 points. Overall, there are 792 data points along the axial direction. As the fits get better by removing middle points from the fit, the sizes of the left and right walls approach those of Fig. 7.2 where the fit quality is good without removing any points. Values of D are found from fits with excluded points.
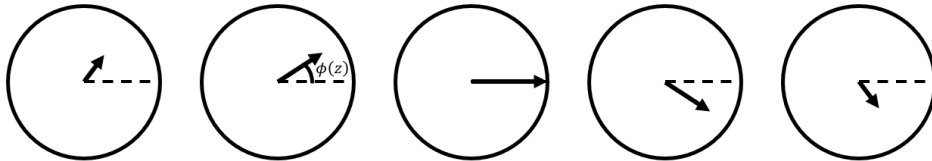

Figure 7.4: Schematic representation of the magnitude and orientation of the initial transverse spin component across a domain wall viewed from the longitudinal axis of the Bloch sphere. The direction of rotation of the transverse spin is opposite in the two walls. The state vector takes a helical path as it goes from state $|1\rangle$ to $|2\rangle$.

make the differential potential uniform, all the spin vectors rotate at the same rate.

7.3 Evolution of the system

Using the threshold method explained in Chapter 6, positions of domain wall centers as a function of time are extracted. In the following discussions, various quantities obtained from wall centers are analyzed. A bigger picture of the dynamics of the walls is given next. Then, some two-domain systems are given for comparison to illustrate the point that motion of a domain wall is not limited to three-domain systems. These examples also clarify the initial conditions for wall displacement over the evolution of the system. At the end, an example of dynamical creation of domain walls in a three-domain system is presented.

7.3.1 Dynamics of the left and right domain walls

Figure 7.5 shows examples of motions of domain walls for different middle domain sizes for initializations similar to those in Fig. 7.2 and Fig. 7.3. What is common in their behavior is an initial movement towards the center of the trap and then reversing their direction and heading outward towards the edges of the cloud. This type of motion for a range of middle domain widths resembles that of an unstable oscillation, so a phenomenological model of the form

$$\Delta z = A e^{\gamma t} \sin(\omega t), \tag{7.3}$$

is used as the fitting function, where $\{A, \gamma, \omega\}$ are the fitting parameters. Here, oscillation growth rate (γ) and oscillation frequency (ω) are both positive, but amplitude (A) is allowed to be negative to account for the π-shift in the initial phase of the oscillations. Δz stands for $\Delta z_{L/R} = z_{L/R}(t) - z_{L/R}(t = 0)$ for the left and right walls. Eqn. 7.3 fits well to the data. Figure 7.6 shows examples of fitting this equation to the data of domain wall positions for a few cases.
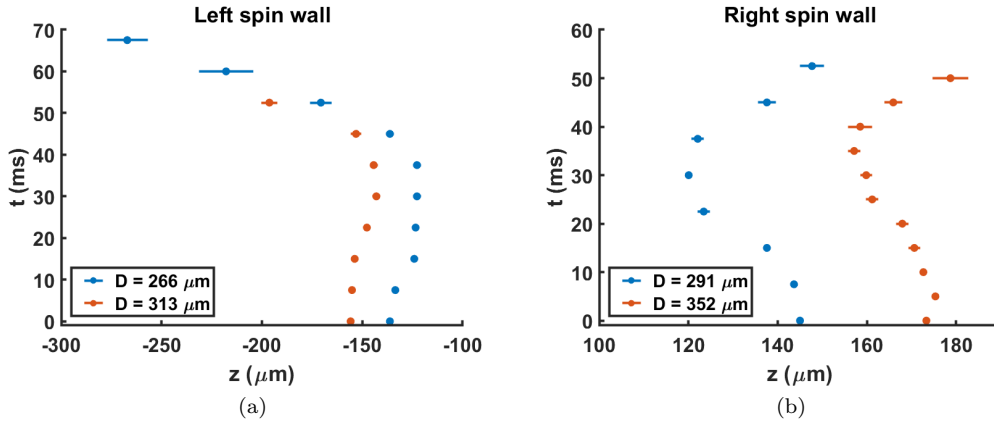

Figure 7.5: Extracted positions of (a) left and (b) right spin domain wall centers for different values of initial middle domain size (D). For initializations similar to Fig. 7.2 and Fig. 7.3, the walls have the typical motion of first moving inward toward the trap center and then reversing their direction, heading outward. Their motions resemble that of an unstable oscillation.

A summary of fitting parameters of Eqn. 7.3 for a wide range of initial middle domain
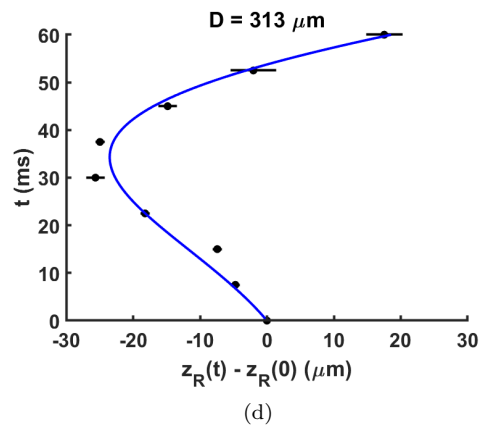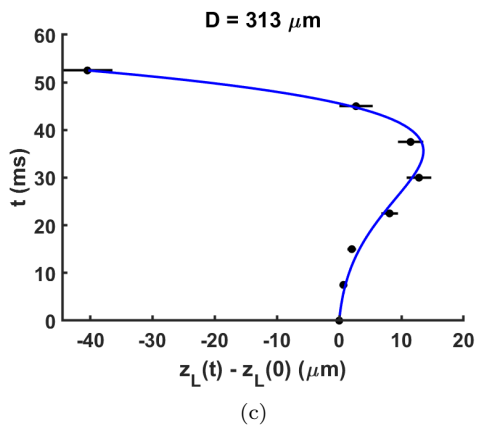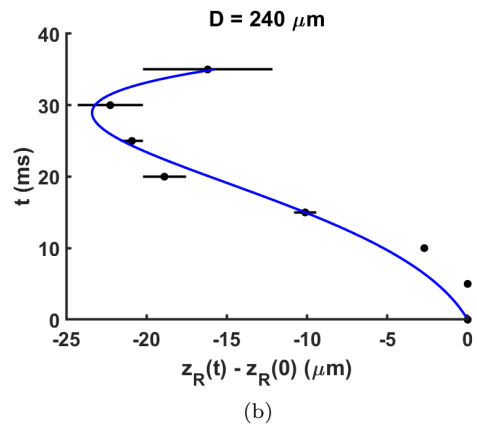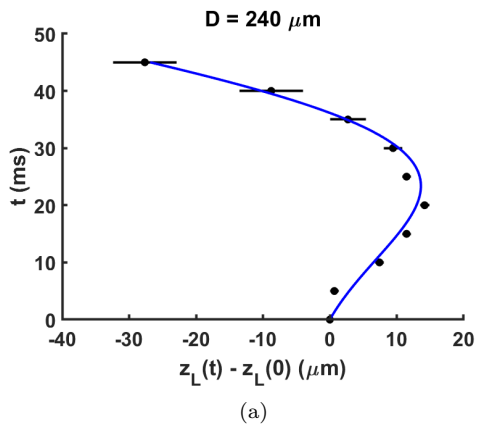
Figure 7.6: Examples of fitting Eqn. 7.3 to the wall positions for cases of $D = 240\,\mu$m in (a) and (b), and $D = 313\,\mu$m in (c) and (d).
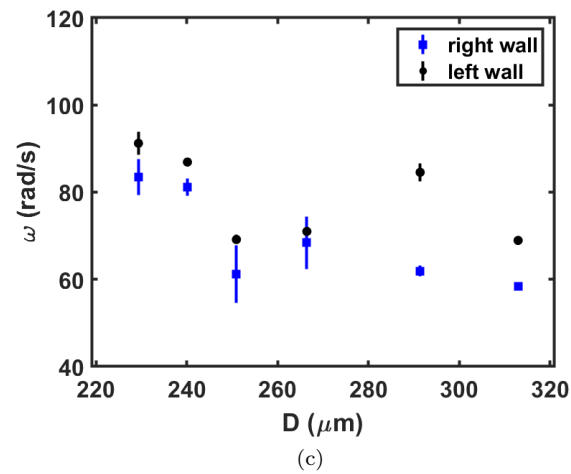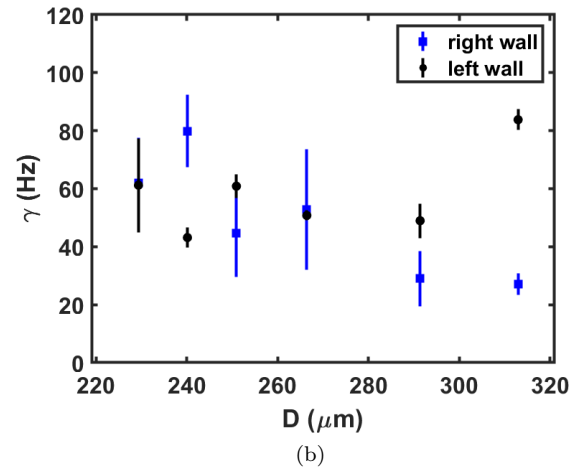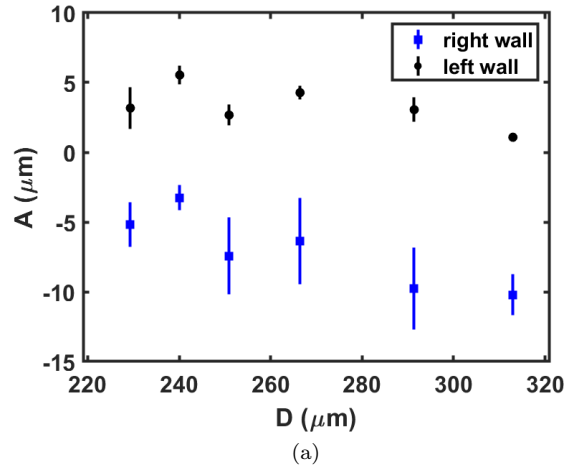
Figure 7.7: Results of fitting Eqn. 7.3 to left and right domain wall trajectories for a wide range of initial middle domain width D. None of the fit parameters shows a strong dependence on D. The vertical bars are fit uncertainties.

widths is shown in Fig. 7.7. What is interesting is that the fitting parameters, namely the amplitude, oscillation growth rate, and oscillation frequency, all show only a weak dependence on the size of the middle domain in this range, i.e. for a large range of the ratio of N_2 to N_1 in the initialization, overall behavior of each wall remains fairly the same. The width of the Gaussian profile of density is about $190\,\mu$m, while the range of the middle domain width is from $230\,\mu$m to $313\,\mu$m in Fig. 7.7. The ratio of the total populations in the two states is defined by

$$\eta \equiv \frac{\sum\limits_{z} N_2\left(z, t = 0\right)}{\sum\limits_{z} N_1\left(z, t = 0\right)}, \tag{7.4}$$

where summation is taken over all axial bins. In this data set, η changes from 1.38 to 0.86 and passes through unity, but no remarkable change in the behavior of the system is observed in this short-time part of the evolution.
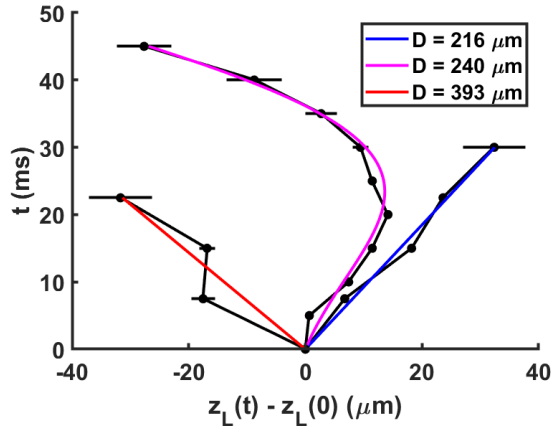

Figure 7.8: Left domain wall motion for small, medium, and large middle domain widths. Depending on the size of the initial domain, the wall can show a linear or an unstable oscillatory motion. The red and blue lines are linear fits and the magenta line is a fit using Eqn. 7.3. The right wall exhibits similar behavior.

The range of D values in Fig. 7.7 is a modest range of values. For D values that are out of this range, signifying a small or large middle domain, behavior of the walls is drastically different. Overall, the data shows three regimes of motion of a domain wall, as shown in Fig. 7.8. For D values in the middle range, the motion is the typical unstable oscillation. When D is relatively small or large, the motion becomes linear with slopes of opposite signs for the two cases. For small and large initial population ratios, the motion is dominated by the state that has the larger number of atoms. When state $|1\rangle$ is in the middle and has much smaller population, the region of state $|2\rangle$ atoms expands by pushing the wall towards the center of the cloud. When N_1 is much larger in the beginning, state $|1\rangle$ atoms prevail and their domain expands by pushing the spin walls towards the edges of the cloud.

Plots in Fig. 7.9 illustrate how transition from oscillatory to linear motion for the left wall occurs as η becomes smaller with D getting larger. There is no recognizable type of motion between these two cases and Eqn. 7.3 would not be a good fitting model.
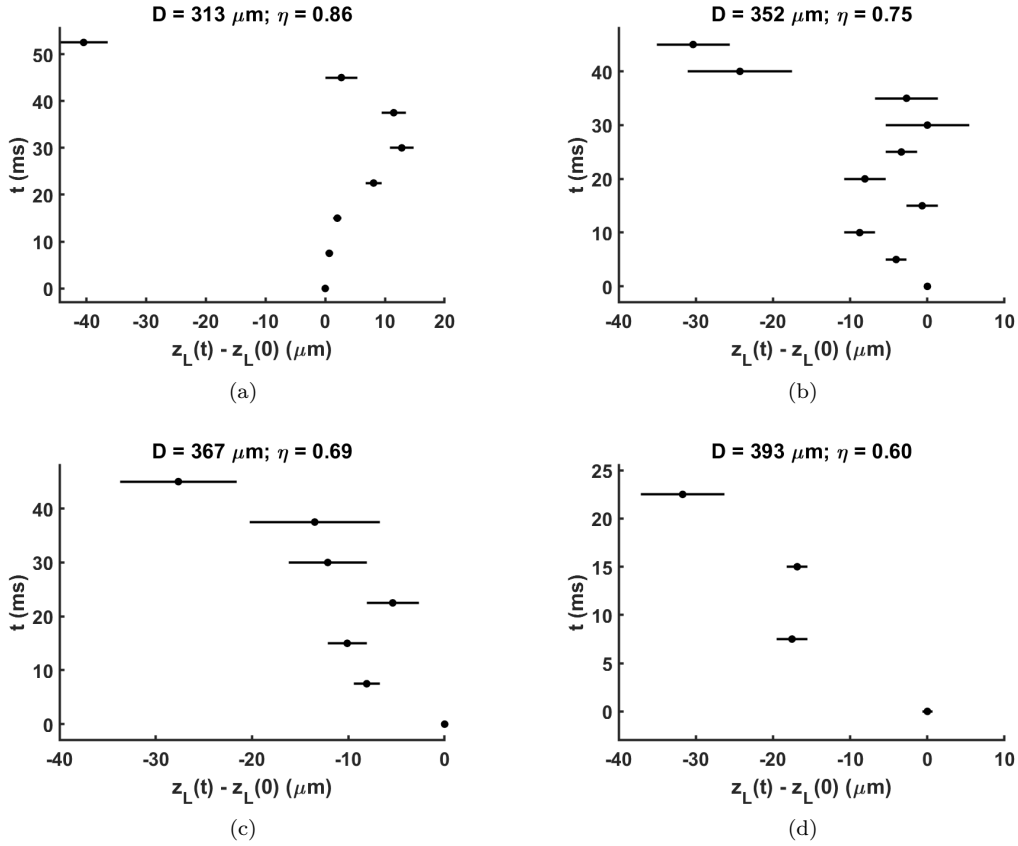
Figure 7.9: Transition of the type of motion of the domain wall. As D (or equivalently η) increases, the motion changes from an unstable oscillation to more like a linear evolution.

7.3.2 Turning points

Based on the fitted trajectories, the turning points of domain walls are found. The red square in Fig. 7.10(a) is an example of where the wall reverses its direction of motion. Δz_{turn} is defined to be the distance a wall moves from its original position until it reaches its maximum inward deviation. Figure 7.10(b) gives the values of these displacements. Similarly, Fig. 7.10(c) shows values of t_{turn}, which is the time it takes a wall to reach the turning point. Since the fit parameters for each wall are almost equal within the middle range of D values, it should be expected that the distance the left (right) wall shifts to the right (left) before it turns its direction of motion is almost independent of the initial z_L (z_R). For the same reason, it is expected for t_{turn} not to vary much within this range of D values. These expectations are confirmed by Fig. 7.10(b) and Fig. 7.10(c). The average time for the left wall to reach the turning point is $\sim 29\,\mathrm{ms}$ and it is $\sim 32\,\mathrm{ms}$ for the right wall.
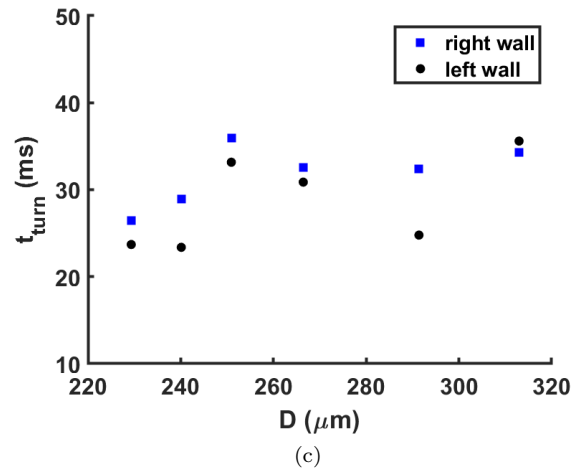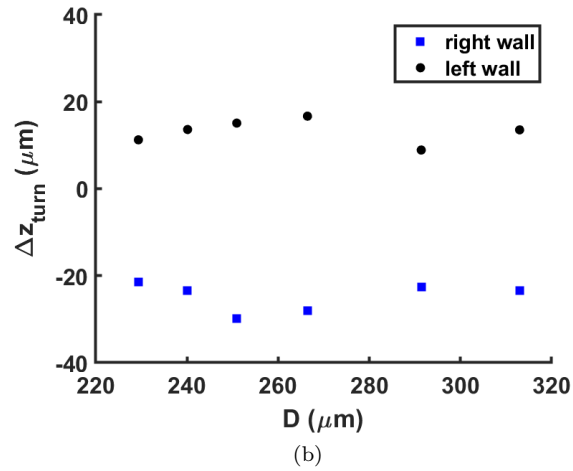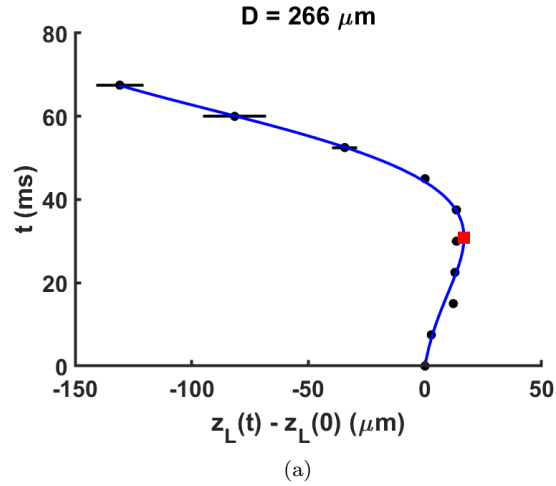
Figure 7.10: Δz_{turn} and t_{turn} vs. D. The range of D values is the same as in Fig. 7.7. (a) Example showing location of the turning point of the left wall indicated by the red square. (b) and (c) are Δz_{turn} and t_{turn} vs. D, respectively. All the points in (b) and (c) are found from fits to the wall trajectories. Square points are for the right wall, and circles for the left wall. The results show that turning point displacements and times are only weakly dependent on D for the given range.

66

7.3.3 Velocities

Instantaneous velocity of the walls at time

$$t^* \equiv \frac{t_{i+1} + t_i}{2}$$

can be approximated by

$$v\left(t^*\right) = \frac{z\left(t_{i+1}\right) - z\left(t_i\right)}{t_{i+1} - t_i}, \tag{7.5}$$

where i runs over the number of sampled times. Figure 7.11 shows the results of the calculations as the ratio of instantaneous velocity to the thermal velocity (v_{th}). At $T = 650\,$nK, $v_{\text{th}} = 7.9\,\mu$m/ms. The plots confirm that the travel speed of spin information is limited by the thermal velocity.
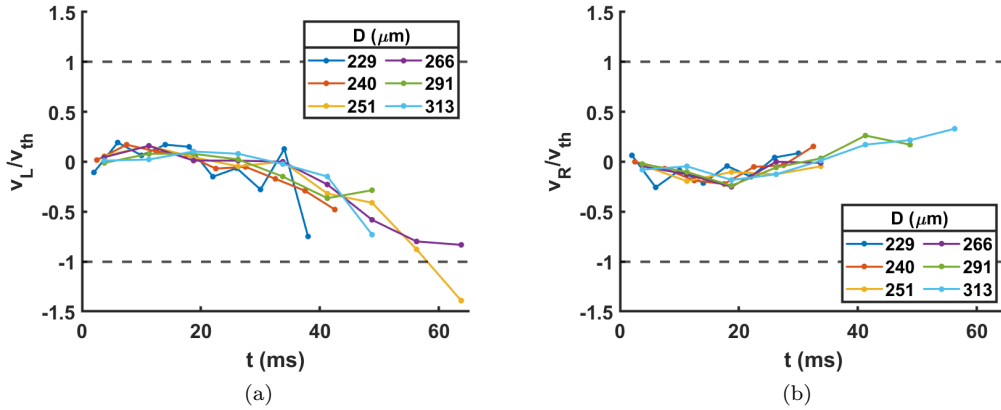

Figure 7.11: Instantaneous velocities of domain walls scaled by thermal velocity for a range of D. The range of D values is the same as in Fig. 7.7. It is expected that all the points stay within the boundary ± 1 as the speed of spin information cannot surpass v_{th}.

On the edges of the cloud, the SNR drops, and it is not possible to draw conclusions about the behavior of the walls in those regions. However, the trends of velocities suggest two possibilities. One is that the velocity keeps increasing while the wall moves towards the cloud edge until it reaches the end and essentially dies. Another possibility is that the acceleration changes direction towards the cloud center, the velocity changes its direction once more, and the wall continues by coming back towards the central region. The current SNR in our system does not allow us to see which one is the case.

7.3.4 Initial impurity

In the initializations of the data shown so far, state $|1\rangle$ atoms are always in the middle of the cloud while the two sides consist of atoms in state $|2\rangle$. However, due to imperfections in our current domain preparation method, there are always some $|2\rangle$ atoms in the central region, making the middle domain "impure." Impurity here only refers to the magnitude of the longitudinal spin being less than its maximum due to the presence of a transverse spin

component. Over the course of this work, we learned that the impurity significantly affects the dynamics of the domain walls, and its effects are further explored below.
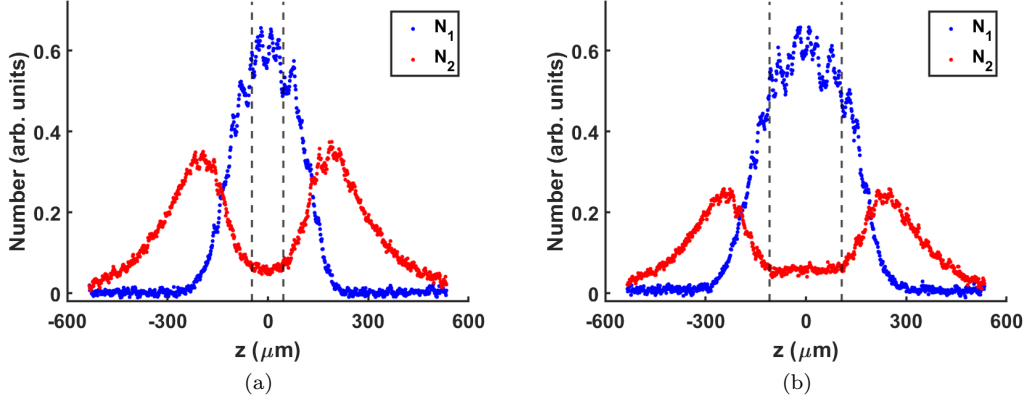

(a)   (b)

Figure 7.12: Examples of impurity in the middle domain. Vertical dashed lines set the boundaries in calculating β in Eqn. 7.6.

To quantify the initial impurity, we can define boundaries where N_2 becomes approximately constant in the middle domain in the initial longitudinal profile. Examples are shown in Fig. 7.12 where the boundaries are defined by the vertical dashed lines. The impurity (β) is then defined by

$$\beta \equiv \frac{\sum\limits_{z \in \mathrm{boundary}} N_2\left(z, t=0\right)}{\sum\limits_{z \in \mathrm{boundary}} N_1\left(z, t=0\right)}, \tag{7.6}$$

where summation is taken over the axial bins within the boundary. We can add more impurity by setting the detuning away from its ideal value of $\sqrt{3}\Omega_R$ while keeping the cloud-wide π-pulse resonant for the dark regions of the DMD patterns.

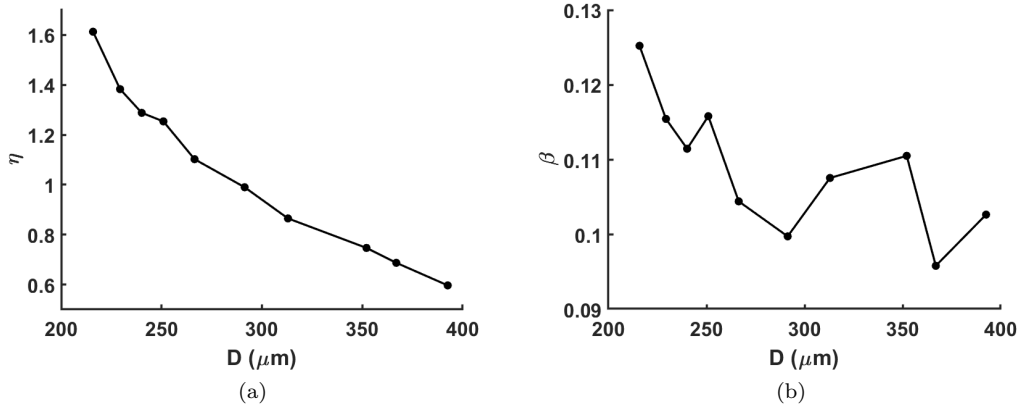(a)   (b)

Figure 7.13: Change in (a) total atom ratio (η) and (b) impurity in the central region (β) as the initial middle domain width increases.

The changes in η and β for a range of the middle domain width that includes those in

Fig. 7.7 are shown in Fig. 7.13. Behavior of η is as expected: as D increases over a relatively large range, η drops significantly. β interestingly only drops by a small amount because N_2 stays almost constant as D increases. The value of β is only slightly sensitive to where the approximate boundary lines are drawn, and in any case, its value does not change by any significant amount.

The small change in β is consistent with the results of fits for the wall motion shown in Fig. 7.10. The amount a domain wall moves toward the center of the cloud is a function of the impurity. Figure 7.14 shows how differences in initial impurity lead to different trajectories of the walls. In Fig. 7.14(b), more impurity is added in the middle compared to the initialization in Fig. 7.14(a), which increases the β value from 0.10 to 0.21. Left and right wall centers are kept the same in both cases so that the middle domain width remains identical. With this setup, the system is allowed to evolve. Figure 7.14(c) and Fig. 7.14(d) show the extracted left and right wall positions, respectively. This example clearly illustrates that more impurity in the center drags the walls further towards the center of the trap before they head to the cloud edges. A similar change in the wall trajectory for larger impurity in a two-domain system will be shown later.
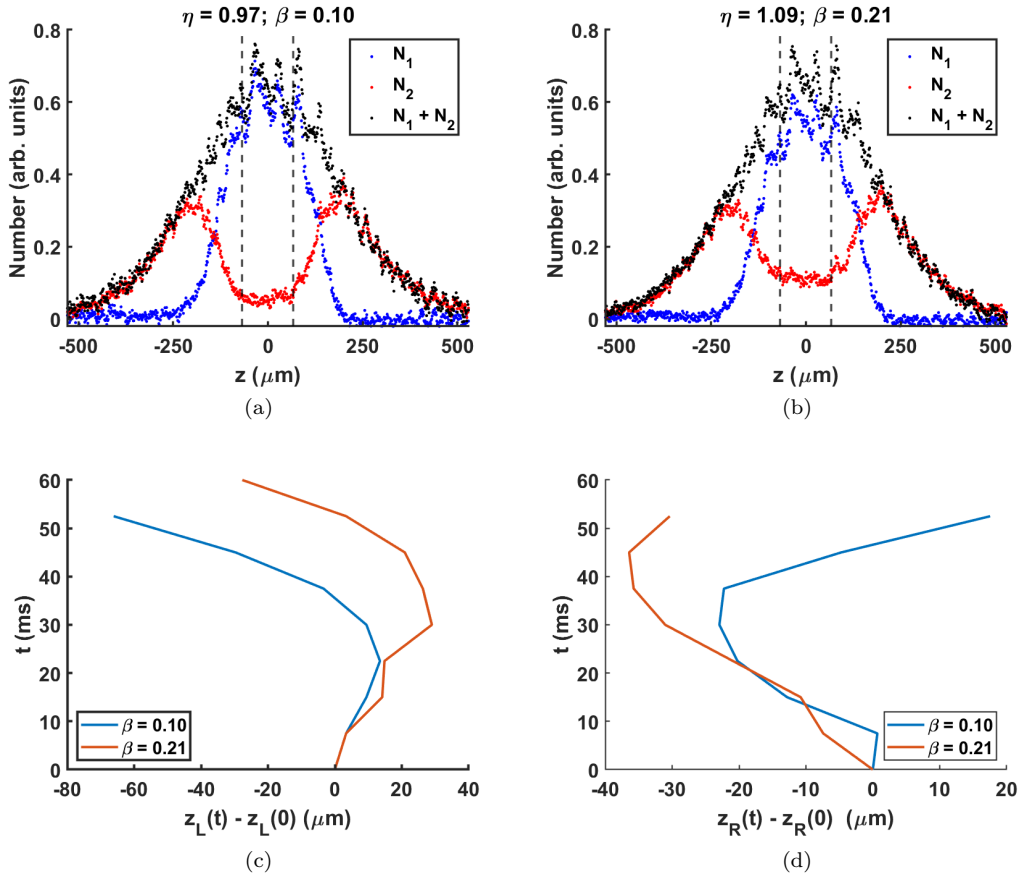

Figure 7.14: Effect of initial impurity on wall trajectories. D is kept constant in (a) and (b), but (b) has a larger impurity. (c) and (d) show the difference in left and right wall trajectories, respectively. More impurity in the middle domain leads to larger displacement of the walls towards the center before they reverse their direction of motion.

7.3.5 Wall motion in a two-domain system

Spin domain wall motion is not limited to systems initialized with three domains. For instance, it can also happen in a system with two domains, provided that the domains are initialized asymmetrically, i.e. the initial position of the domain wall is not at the trap center. Setting the wall off-center in the beginning breaks the symmetry in the population ratio and the trap potential. Figure 7.15 shows two cases of a two-domain system where one has a symmetric initialization and the other is asymmetric. Figure 7.15(b) shows a spatio-temporal plot of the symmetric example, where the wall remains at the axis of symmetry, indicated by the dashed line at $z = 0$. The initialization in Fig. 7.15(d) is asymmetric with the wall initially at $z = -65\,\mu$m, and as the system evolves, the wall displaces. In general, in a two-domain system the wall moves towards the state that has a lower population of atoms.
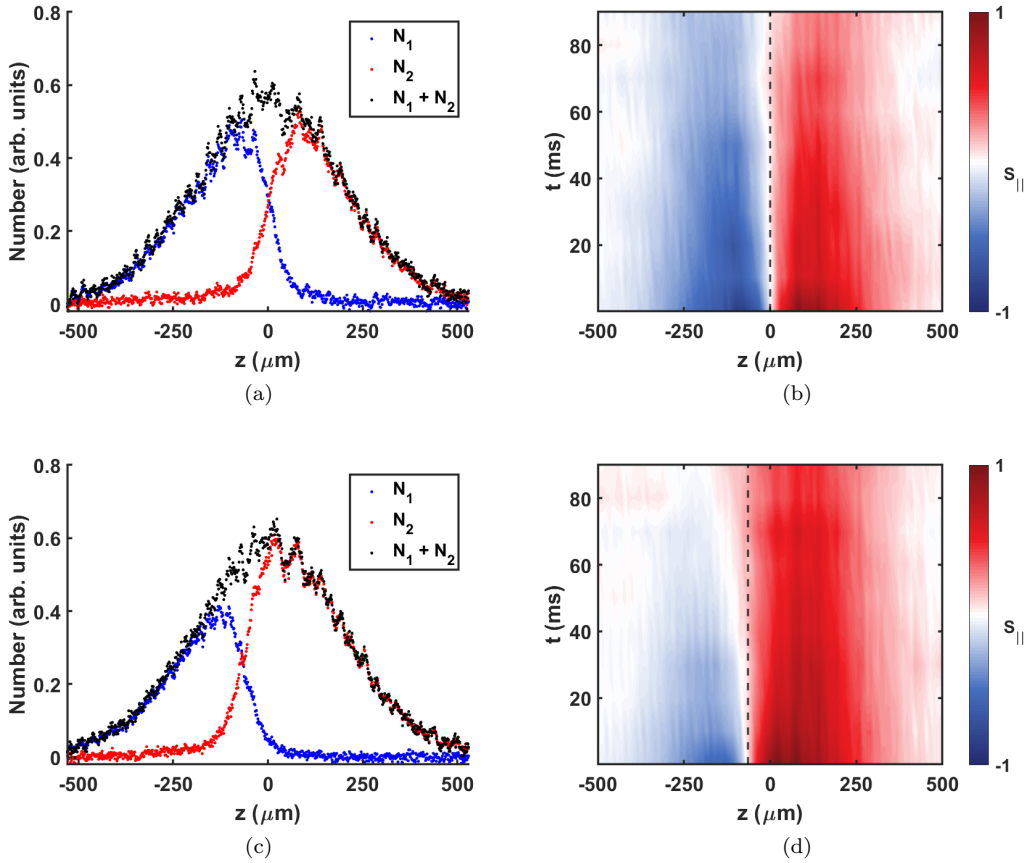

Figure 7.15: Illustrating how domain wall motion can also happen in an asymmetric two-domain system. (a) Initial symmetric initialization and (b) its spatio-temporal plot showing that the wall remains at its original position as the system evolves. (c) Initial asymmetric initialization and (d) its evolution exhibiting gradual displacement of the wall toward the smaller domain.

Similar to a system with three domains, impurity can affect the dynamics of a two-domain cloud. Figure 7.16 shows two cases of asymmetric two-domain systems. The initial

position of the wall center is the same in both cases. The difference is that the impurity in Fig. 7.16(b) is larger than in Fig. 7.16(a). The result is that the wall moves further toward the center in Fig. 7.16(d) versus Fig. 7.16(c). It is evident that the effect of impurity on the dynamics is not merely limited to the trajectory of the wall. In the example here, we can see that it also preserves the state of the domains for a significantly longer time, though the width of each domain changes; in other words, impurity can also have a stabilizing effect due to increased ISRE collisions.
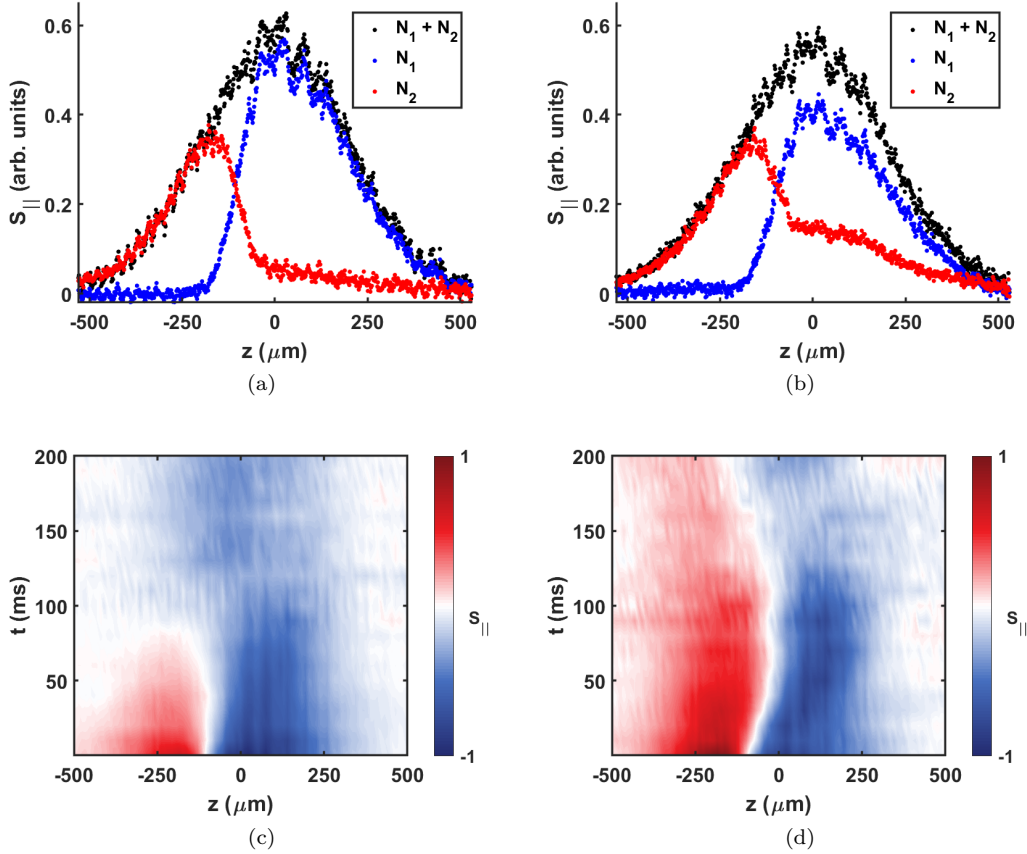

Figure 7.16: Illustrating how impurity can change dynamics of a two-domain system. (a) and (b) are initial profiles with small and large impurities, respectively. The wall center is at the same position in both cases. (c) shows evolution of (a), and (d) corresponds to (b). Similar to a three-domain system (Fig. 7.14), more impurity in a domain can drag the wall further toward that side.

7.3.6 Emergence of new walls in a three-domain system

Another interesting phenomenon that the data shows is dynamic creation of new domain walls, which occurs at longer evolution times. The original walls can move toward the edges of the cloud while new walls emerge near the center of the cloud, an example of which is shown in Fig. 7.17. During this transition, three domains can become five domains due to emergence of the new walls.
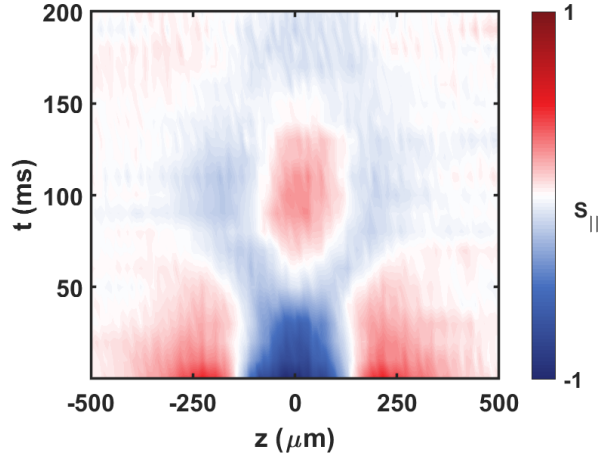
Figure 7.17: Example of dynamic creation of new domain walls in a three-domain system. The initial walls move outward and a new domain (the red region at the center) appears. The new domain is bounded by new walls that have emerged dynamically. During the transition that happens around 50 ms to 80 ms, the new walls increase the number of domains from three to five. Due to the low SNR at the sides of the cloud, we cannot conclusively state whether the system continues with five domains.

The middle domain that is constructed by the new walls can have a different width from the original middle domain. Figure 7.18 shows the inverse relationship between the initial width of the middle domain and the width of the new middle domain. Initializing the middle domain with a larger width results in a smaller middle domain formed by the new walls.

Dynamic creation of new domain walls and properties of the new middle domain are interesting topics. One of our goals is to further investigate these topics in the future.
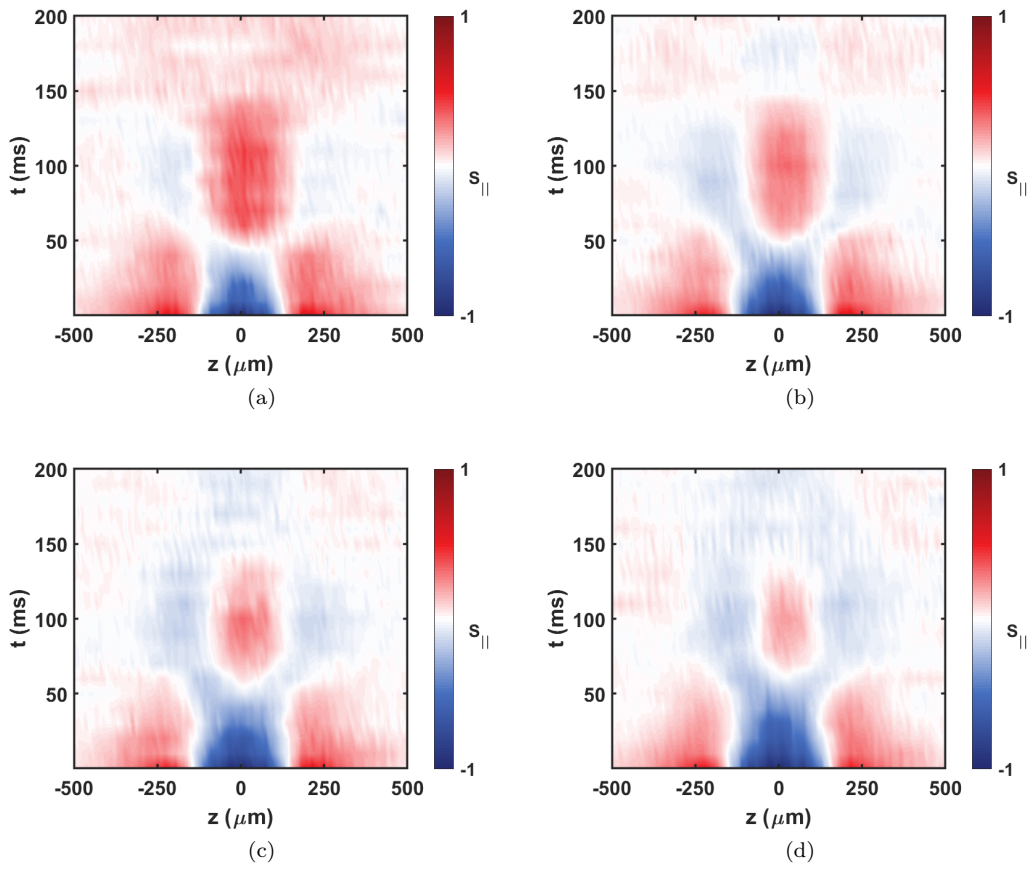
Figure 7.18: Examples illustrating how a wider initial middle domain leads to a narrower new middle domain that is created dynamically. (a) $D = 268\,\mu$m, (b) $D = 275\,\mu$m, (c) $D = 293\,\mu$m, and (d) $D = 310\,\mu$m.

Chapter 8

Conclusions and ideas for future work

As was shown in the previous Chapter, the position of a domain wall can be a dynamic feature of a spin system. It was shown that domain walls do not necessarily stay static when the system evolves, both in two- and three-domain systems.

The data in this work suggest that the primary prerequisite for the walls to move is asymmetry in the transverse spin distribution with respect to the wall center. Given that in our system the atom density has a Gaussian profile, constructing a domain wall away from the center of the trap breaks the local symmetry in the transverse spin distribution. Figure 7.15 shows how moving the wall from the trap center in a two-domain system leads to motion of the wall. In the three-domain systems studied in this work, there is necessarily an asymmetry in the local transverse spin distribution around the centers of both walls, even when the total population ratio of the two states is unity. In all of the examples that have been shown for the three-domain systems, the walls displace as the system evolves. It should be emphasized that this suggested prerequisite for the motion of a domain wall is a subject for future studies.

The experimental results show that impurity is not the only factor that determines the behavior of a domain wall. In Fig. 7.8, the impurity does not change much, yet the walls belong to different regimes of motion (namely, linear and unstable oscillation). Another determining factor is the total population ratio of the two states. For the cases where the wall moves linearly, the middle domain size is very small or very large, which results in a more imbalanced population ratio. In the cases where domain walls exhibit similar oscillatory motions (Fig. 7.7), the impurity is almost constant and the population ratio is closer to unity.

More transverse spin in a domain is seen as higher impurity in our system. In the previous Chapter, it was shown how initial impurity can be used as a control parameter to affect the trajectory that a domain wall takes. In an asymmetric two-domain system, if a state has a smaller total population, the wall will move toward the side of that state. However, if enough impurity is added to the other domain, the wall will first move toward that domain before reversing its direction (Fig. 7.16). Figure 7.14 shows a similar effect in

three-domain systems, where adding impurity makes the walls move further inward before changing their directions.

In the rest of this Chapter, we present a few interesting topics that are feasible to explore in our experimental system. One topic is the dynamic emergence of new domain walls that was mentioned in the last Chapter. Figure 7.18 shows that the width of the dynamically created middle domain can be different from that of the original middle domain, depending on the initial width of the middle domain. It would be quite interesting to explore the phenomenon of dynamic creation of new domain walls and geometrical properties of the new middle domain.

Another topic to explore is the effect of the widths of the domain walls on the dynamics of a three-domain system. In this work, the walls were kept at the same size in the initialization while investigating how the size of the middle domain modifies the oscillatory motion of domain walls. Figure 8.1 shows an example of the opposite case where the middle domain size is kept constant and the walls are made larger in the initialization. The conditions of larger walls in Fig. 8.1(b) as compared to Fig. 8.1(a) illustrates a stabilizing effect, though the width of the domains change. Moreover, in this case the walls exhibit a stable oscillatory motion as opposed to the unstable oscillatory motion seen in this work.
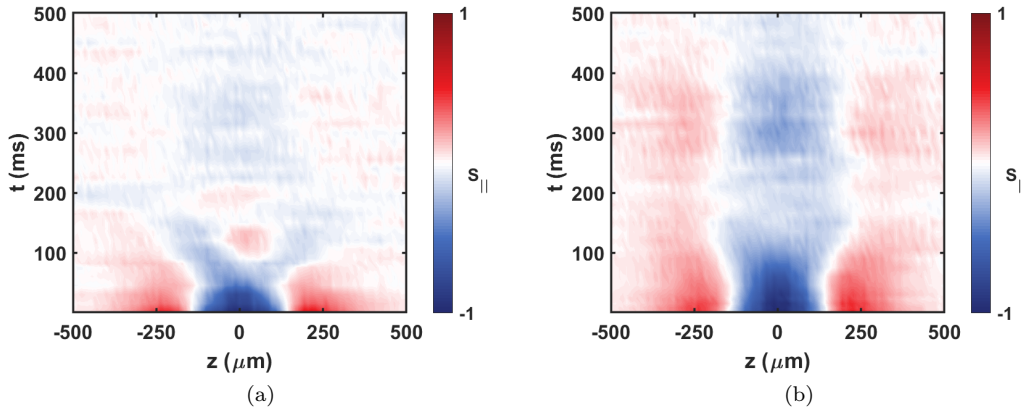

<div style="text-align:center">(a)   (b)</div>

Figure 8.1: Illustrating how domain wall widths can drastically change the dynamics. The walls are initialized with a width of about (a) $75\,\mu$m and (b) $114\,\mu$m. The width of the middle domain and the impurity are kept constant in the initialization of (a) and (b).

Previous work by the McGuirk group has shown that domains in a two-domain system can be stabilized by applying a linear differential potential with a certain slope (see Ref. [12]). The same stabilization technique can be applied to three-domain systems with a double-linear potential that has a V-shape or an inverted V-shape potential. Figure 8.2 shows an example in which the applied double-linear potential has stabilized the domains for at least $200\,$ms. Both in Fig. 8.2 and in Ref. [12], the stabilizing potential is applied from the beginning, i.e. before the walls start moving. A question that remains to be answered is what potential would stabilize a moving wall? It is already clear that this problem is more challenging because the slope of the required stabilizing potential depends on the width of the wall, which is itself a dynamic quantity. As the system evolves, the width of the wall

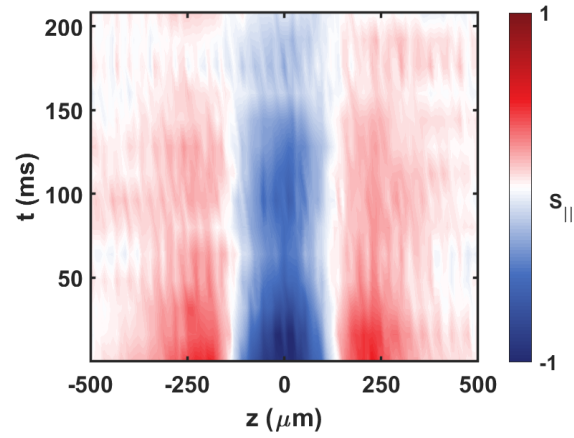changes so it matters when the stabilizing potential is applied.

Figure 8.2: Example of experimentally stabilizing a three-domain system with a double-linear differential potential.

The data in this work has shown different trajectories for domain-wall motion. One general question that remains is this: if we want a domain wall to have a certain trajectory, what should the initial conditions and the governing differential potential be? This question is easier to explore in a two-domain system, and part of our ongoing work is in that direction.

Bibliography

[1] M. Takamoto, F.L. Hong, R. Higashi, and H. Katori, "An optical lattice clock," *Nature* **435**, 321 (2005).

[2] J. M. McGuirk, G. T. Foster, J. B. Fixler, M. J. Snadden and M. A. Kasevich, "Sensitive absolute-gravity gradiometry using atom interferometry," *Physical Review A* **65**, 033608 (2002).

[3] W. B. Cairncross, D. N. Gresh, M. Grau, K. C. Cossel, T. S. Roussy, Y. Ni, Y. Zhou, J. Ye, amd E. A. Cornell, "Precision measurement of the electron's electric dipole moment using trapped molecular ions," *Physical Review Letters* **119**, 153001 (2017).

[4] A. E. Meyerovich, "Quantum and nonlocal coherent effects in Boltzmann gases," *Physical Review B* **39**, 9318 (1989).

[5] C. Lhuillier and F. Laloë, "Transport properties in a spin polarized gas, I," *Journal de Physique* **43**, 197 (1982).

[6] J. M. McGuirk, H. J. Lewandowski, D. M. Harber, T. Nikuni, J. E. Williams and E. A. Cornell, "Spatial resolution of spin waves in an ultracold gas," *Physical Review Letters* **89**, 090402 (2002).

[7] J. M. McGuirk and L. F. Zajiczek, "Localized collapse and revival of coherence in an ultracold Bose gas," *Physical Review A* **83**, 013625 (2011).

[8] C. Deutsch, F. Ramirez-Martinez, C. Lacroûte, F. Reinhard, T. Schneider, J. N. Fuchs, F. Piéchon, F. Laloë, J. Reichel, and P. Rosenbusch, "Spin self-rephasing and very long coherence times in a trapped atomic ensemble," *Physical Review Letters* **105**, 020401 (2010).

[9] G. Nunes, C. Jin, D. L. Hawthorne, A. M. Putnam, and D. M. Lee, "Spin-polarized $^3-^4$He solutions: Longitudinal spin diffusion and nonlinear spin dynamics," *Physical Review B* **46**, 9082 (1992).

[10] J. M. McGuirk and L. F. Zajiczek, "Optical excitation of nonlinear spin waves," *New Journal of Physics* **12**, 103020 (2010).

[11] D. Niroomand, S. D. Graham and J. M. McGuirk, "Longitudinal spin diffusion in a nondegenerate trapped ^{87}Rb gas," *Physical Review Letters* **115**, 075302 (2015).

[12] S. D. Graham, D. Niroomand, R. J. Ragan and J. M. McGuirk, "Stable spin domains in a nondegenerate ultracold gas," *Physical Review A* **97**, 051603 (2018).

[13] H. J. Lewandowski, *Coherences and correlations in an ultracold Bose gas*, Ph.D. thesis, University of Colorado (2002).

[14] D. Niroomand, *Observation of the Castaing Instability in a Trapped Ultracold Bose Gas*, M.Sc. thesis, Simon Fraser University (2013).

[15] D. Niroomand, *Spin transport in an ultra-cold trapped non-condensed ^{87}Rb gas*, Ph.D. thesis, Simon Fraser University (2018).

[16] S. Graham, *Modifying spin diffusion in a nondegenerate ultracold gas*, Ph.D. thesis, Simon Fraser University (2019).

[17] H. J. Metcalf and P. van der Straten, "Laser cooling and trapping of atoms," Springer Verlag (1999).

[18] W. Ketterle, D. S. Durfee and D. M. Stamper-Kurn, "Making, probing and understanding Bose-Einstein condensates," in *Proceedings of the International School on Physics "Enrico Fermi" 1998, Bose-Einstein Condensation in Atomic Gases*, edited by M. Inguscio, S. Stringari, and C. E. Wieman (IOS Press, 1999), pp. 67–176.

[19] T. Nikuni, J. E. Williams and C. W. Clark, "Linear spin waves in a trapped Bose gas," *Physical Review A* **66**, 043411 (2002).

[20] J. E. Williams, T. Nikuni and C. W. Clark, "Longitudinal spin waves in a dilute Bose gas," *Physical Review Letters* **88**, 230405 (2002).

[21] H. J. Lewandowski, D. M. Harber, D. L. Whitaker and E. A. Cornell, "Observation of anomalous spin-state segregation in a trapped ultracold vapor," *Physical Review Letters* **88**, 070403 (2002).

[22] T. Nikuni and J. E. Williams, "Kinetic theory of a spin-1/2 Bose-condensed gas," *Journal of Low Temperature Physics* **133**, 323 (2003).

[23] B. J. Verhaar, D. J. Wineland, C. E. Wieman and S. J. Smith, "Cold collision phenomena," *AIP Conference Proceedings* **323**, 351 (1994).

[24] J. N. Fuchs, D. M. Gangardt and F. Laloë, "Internal state conversion in ultracold gases," *Physical Review Letters* **88**, 230404 (2002).

[25] R. Grimm, M. Weidemüller and Y. B. Ovchinnikov, "Optical dipole traps for neutral atoms," in *Advances in atomic, molecular, and optical physics* (Elsevier, 2000), Volume 42, pp. 95–170.